On Electronic Transport through Single Molecules in Nanostructures

Zur Erlangung des akademischen Grades eines
DOKTORS DER NATURWISSENSCHAFTEN
von der Fakultät für Physik des
Karlsruher Instituts für Technologie (KIT)

genehmigte

DISSERTATION

von

Dipl.-Phys. Birgit Angelika Kießig
aus Stuttgart

Tag der mündlichen Prüfung: 30. November 2012

Referent: Prof. Dr. Hilbert von Löhneysen
Korreferent: Prof. Dr. Alexey Ustinov

Zum elektronischen Transport durch einzelne Moleküle in Nanostrukturen

Kurzfassung

Diese Arbeit fasst die Ergebnisse von Transportexperimenten an unterschiedlichen Nanostrukturen zusammen. Dabei werden im Wesentlichen zwei Themen behandelt. Zum Einen wird ein Ansatz zur Kontaktierung und Untersuchung von Molekülen auf der Grundlage von Elektromigration beschrieben. Ein Feedback-kontrollierter Mechanismus wurde zur Bildung von nur wenige Nanometer breiten Lücken in Strukturen aus dünnen metallischen Schichten verwendet. Seine Handhabung sowie die Entwicklung des Probenwiderstandes während des Prozesses werden im Detail beschrieben. Weiterhin wird die Temperaturerhöhung in dünnen stromführenden Leitern durch Joulesche Wärme mit einem zweidimensionalen Modell numerisch berechnet. Inbesondere der Einfluss der thermischen Leitfähigkeit des Substrates und der Probengeometrie auf das lokale Aufheizen einer Metallstruktur während gezielter Elektromigration wird analysiert. Zuletzt werden erste Leitfähigkeitsmessungen an Oligophenyl-Ethynylen-Molekülen, die zwischen den erzeugten Elektrodenpaaren deponiert wurden, gezeigt und diskutiert.
Zum Anderen werden im vorliegenden Text Tieftemperaturmessungen an einem System von Kohlenstoffnanoröhrchen (carbon nanotubes, kurz: CNTs) präsentiert, welches Charakteristiken von untereinander kapazitiv gekoppelten Quantenpunkten erkennen ließ. Die Präparation der Proben und ihre Untersuchung im ^{3}He-^{4}He-Mischkryostaten werden erklärt. Des Weiteren werden numerische Simulationen erläutert, die eine Reproduktion des experimentell beobachteten Transportverhaltens und die Zuordnung einzelner Merkmale der Messungen zu physikalischen Kontakt- und Kopplungseigenschaften der Nanoröhren erlauben.

On Electronic Transport through Single Molecules in Nanostructures

Abstract

This thesis summarizes transport experiments performed on different nanostructures. Two main topics are treated. On the one hand, an approach for contacting and measuring molecules based on electromigration is presented. A feedback-controlled mechanism has been employed to generate gaps only a few nanometers wide in structures prepared from thin metallic films. The procedure is explained and a detailed description of the development of the sample resistance vs. bias voltage measured during the gap formation process is given. Furthermore, the temperature rise in thin current carrying conductors by Joule heating is numerically determined with a two-dimensional model. In particular, the influence of the thermal conductance of the substrate on the heating of a sample during deliberate electromigration is analyzed. Finally, first conductance measurements on oligo(phenylene ethynylene) molecules placed in the generated nanogaps are described and interpreted.
On the other hand, the results of low temperature transport measurements on a system of carbon nanotubes (CNTs) which revealed characteristics of capacitively coupled quantum dots are shown. The preparation of samples and their investigation in a ^{3}He/^{4}He dilution refrigerator are explained. In addition, numerical simulations are introduced, which allow the reproduction of features of the experimentally observed conductance behavior and their attribution to physical properties of the interacting CNTs.

Contents

1 Motivation

Field effect transistors are of central importance for every modern electronic circuit. The current flow from the source to the drain contact of these three-terminal devices can be influenced by a third electrode, the gate. By now, the continuous miniaturization of those building blocks is reaching the length scales of molecules. At such small dimensions coherence is an important issue. It would lead to interference effects in the interplay of two or even more of said components which are not considered in the classical transport theory of charge carriers and could crucially alter the transport behavior of an entire electronic circuit. One might want to avoid or be able to exploit such interference effects, but either way one has to know about their nature.
It was the aim of this PhD project to investigate coherence in molecular transport with the help of the *Aharonov-Bohm effect*, which was first predicted in 1959 as a manifestation of the effect of the vector potential of a magnetic field on the quantum mechanical phase of charged particles [1]. In metals, it leads to periodic fluctuations in the magnetoresistance of multiply connected structures if electron transport through them is phase-coherent. This is the case as long as only elastic scattering occurs, i. e. the charge carriers do not exchange neither energy nor spin with the lattice in an inelastic manner. Thus the device has to be smaller than the inelastic electron mean free path l_{in} [2, 3].
Consequently, our realization of experiments with macromolecules started with the structuring of metallic rings smaller than l_{in}. Gold is a suitable metal for this purpose. At low temperatures, the inelastic electron mean free path $l_{\mathrm{in}}(\mathrm{Au})$ is of the order of one micron, essentially limited only by the distance of magnetic impurities. Apart from that, gold also has further experimental advantages. To list only a few, it does not corrode in air, is available in high purity, can easily be evaporated and can form covalent bonds to molecules with a thiol end group [4, 5]. The details of the sample preparation procedure are given in Secs. 3.1.1 and 3.1.2.
Macromolecules with an experimentally reasonable conductance are usually of the size of a few nanometers only. Up until now, electrodes with such a small spacing cannot be fabricated by standard lithography techniques. Section 2.1 gives a short overview over the field of single-molecule transport measurements and the various contacting methods tried so far. In particular, the concept of electromigration and its application in this context are introduced in Sec. 2.2. For the integration of macromolecules into metallic structures suitable for Aharonov-Bohm measurements in the framework of this thesis, we generated a nanogap in each of the two ring arms by feedback-controlled electromigration [6, 7] thus creating two electrode pairs. The procedure is explained in Sec. 3.1.3 and its results are analyzed in Sec. 4.1.
Preferably, a single specimen of a known molecule should be bridging each of the two electrode pairs. Working in an environment as clean as possible is thus a prerequisite for reliable measurements and results. In that respect, in-situ electromigration and immediate molecule deposition by sublimation in a cryostat would have been the optimal method. However, synthesis of a suitable molecule proved very challenging and in the end we had to resort to deposition

from solution. Process and results can be found in Secs. 3.1.4 and 4.2, respectively.
After several attempts and scarce results we realized that we are not able to provide the statistics necessary to extract meaningful results from our measurements on macromolecules in a reasonable time. Therefore we decided to focus on even larger molecular structures, namely *Carbon Nanotubes* (*CNTs*). In Sec. 2.3 their molecular and electronic properties are introduced [8–10], followed by a theoretical treatment of transport through spatially confined structures weakly coupled to their surroundings in Sec. 2.4. Typically, a suppression of conductance in the low bias regime is observed. This phenomenon is called *Coulomb blockade*. It can be lifted by applying an appropriate voltage to a third, capacitively coupled electrode [11]. We therefore implemented two separately addressable gates in the sample layout to independently shift the energy spectra of our two conduction channels.
Working with CNTs had several advantages for us. First of all, they can be up to several centimeters long [12], so their contacting does not require electromigration. Second, we could build on the experience of the group of Prof. Ralph Krupke at the INT with the deposition of CNTs by ac-dielectrophoresis [13, 14]. The complete sample preparation and this technique in particular are described in Sec. 3.2.
At low temperatures the inelastic mean free path of electrons in metals is enlarged as mentioned above. Therefore we intended to test for Aharonov-Bohm oscillations in a ^{3}He/^{4}He dilution refrigerator that can reach a base temperature below 10 mK. A superconducting magnet to generate fields of up to 8 T is also incorporated in the device. With this cryostat we investigated the low temperature transport of carbon nanotubes in a unique sample layout: Two parallel CNTs in a ring structure, each tunable by a separate gate. Our gate- and bias-dependent low-temperature transport measurements are presented in Secs. 4.3.1 and 4.3.2. Experiments with a similar sample are reported in Ref. 15. However, the two CNT junctions included in the ring structures desribed there were formed by parts of the same tube. Furthermore, the metal used for contacting was aluminum with a superconducting transition temperature of $T_C = 1.2$ K. The focus of the published low-temperature measurements lay on the SQUID behavior of the generated device.
With the help of numerical calculations described in Sec. 4.3.3, our experimental findings can be reproduced and interpreted as specified in Sec. 4.3.4. Up to date, all our measurement results can be explained by a model that does not take into account coherence. Magnetoresistance measurements were also performed, but proved challenging and so far showed no signs of periodic oscillations. In summary, we still cannot prove coherence in low-temperature transport through carbon nanotubes in an Aharonov-Bohm ring structure and further investigations remain to be carried out. Chapter 5 gives a detailed overview over both the work on macromolecules and carbon nanotubes performed in the framework of this thesis.

2 Theoretical and Historical Background

This chapter gives a short introduction to the field of single-molecule transport measurements in Sec. 2.1. Subsequently, the concept of electromigration, which was used in the course of this PhD project for the contacting of macromolecules, is explained in Sec. 2.2. For comparison to our experiments, previously obtained results from the low-temperature transport investigation of carbon nanotubes is presented in Sec. 2.3. Finally, tunneling through nanostructures is described in Sec. 2.4 within the framework of the *sequential tunneling model (SQTM)*. The numerical simulations developed later in this thesis for the interpretation of the data from CNT experiments are based on the concepts introduced in that section.

2.1 Single-Molecule Transport Measurements

For the incorporation of macromolecules into electronic circuits, the transport characteristics of various species have to be investigated to find a suitable component for the respective application as e. g. rectifier, switch or transistor. Measuring the electric transport through a single specimen of a molecular compound is a crucial prerequisite for this analysis. However, even today this is a challenging task.

The first transport measurements on molecules were performed using *Langmuir-Blodgett films* [16, 17] or *SAMs (Self-Assembled Monolayers)*. They were contacted with macroscopic electrodes, thus the entire layer contributed to the conductance. Initially, these experiments were aiming at the investigation of tunneling through insulating dielectrics [18]. Thin Langmuir-Blodgett films are ideal spacers for the verification of its exponential distance dependence because of their high degree of order and thus homogeneous, known and scalable thickness. Nowadays, SAMs find a wide range of present and possible future applications [19, 20]. However, aggregations of a large number of interacting molecules do not show exactly the same characteristics as a single specimen.

The invention of the *Scanning Tunneling Microscope (STM)* [21, 22] made the selection of and transport measurements through single molecules possible. A STM tip can serve as a contact electrode of atomic dimension. However, only spatially extended counter electrodes are feasible. To exclude modification of the conduction by the substrate, the molecules therefore have to be placed upright to reduce contact with its surface. An early approach to achieve this was again their incorporation into SAMs. Yet, in this way the environment still influences transport and addressing a single molecule is not guaranteed without further measures. Chemical bonding to tip and substrate [23] have been proposed as a solution to the latter difficulty. Nevertheless, the surrounding molecules remain a hindrance. Consequently, it is more common today to work with single molecules in solution. They are repeatedly pulled upright from a metallic surface with the STM tip whilst I-V curves are recorded. Due to the variation in con-

tact conformation, averaging over many individual contacting cycles is necessary. Results are therefore presented in the form of conductance histograms constructed from a large number of traces [24]. Consequences of molecule conformation [25] and the linker group [26–28] on transport have been investigated using this technique.
A similar method to measure single molecule transport is placing them in a *Mechanically Controlled Break Junction (MCBJ)* [29]. These devices are composed of a notched metallic structure on a flexible substrate, which is fractured by bending it with an adjustable rod. Alternatively after or prior to breaking, molecules are deposited on the junction from solution, often making use of self-assembly again [30]. The advantage of this approach is its operability in air or even vacuum and also at cryogenic temperatures as it does not require a liquid environment. Furthermore, the formed contacts are more stable than contacts with a STM. A drawback however is the slower speed of opening and closing of the electrode gap, which is nevertheless still sufficient to produce a statistically relevant amount of data [31].
All contacting techniques described so far have the disadvantage that it is not possible to include a third electrode for gating in the setup. However, this is crucial for the investigation of transport characteristics of spatially confined structures and for single molecule switching devices. Nanometer-spaced electrodes for single-molecule measurements in a planar geometry can be generated by *electromigration (EM)* which is introduced in Sec. 2.2. The experimental implementation of this technique is explained in Sec. 3.1.3 and the process of gap formation during electromigration is analyzed in detail in Sec. 4.1. The choice of molecules and their synthesis are described in Sec. 3.1.4, followed by a brief outline of the procedure of deposition from solution. Finally, the obtained measurements are discussed in Sec. 4.2.

2.2 Electromigration

The term "electromigration" refers to a thermally assisted ion diffusion process in a conductor under the influence of an applied electric field. Two force components act on the metal ions in this case: the so-called *direct* electrostatic force and the so-called *electron wind* due to the impact of conduction electrons:

$$\vec{F}_{\text{eff}} = \vec{F}_{\text{direct}} + \vec{F}_{\text{wind force}} = |e|(Z + Z^{\text{w}})\vec{E} = |e|Z^*\vec{E} \tag{2.1}$$

where $\vec{E}$ is the applied electric field and e the elementary electric charge. $|e|Z^*$ is called the effective charge. The exact dependence of the dimensionless parameter Z^* and thus the strength and direction of the resulting net force $\vec{F}_{\text{eff}}$ on electronic and structural properties of the respective material is discussed e. g. in Ref. 32. Experimentally found values for various metals are also summarized in this review. For gold, which was used for the measurements described here, atomic motion follows the electron flow.
Electromigration has been known and studied in bulk metals for more than a century, but it only attracted real attention when it became technologically relevant as a major cause for the failure of aluminum conductors in microelectronic circuits in the 1960s. In thin films, ion displacement occurs mainly along grain boundaries and surfaces, but as in bulk, it is essentially determined by two parameters: temperature T and current density j [32]. However, these two

quantities cannot be tuned independently because of Joule heating. Thus, if electromigration is to be employed for the formation of nanometer-sized junctions, the experimental parameters have to be optimized with respect to two competing requirements. On the one hand, material transport accelerates with T and j. For observability on a reasonable time scale an increase of both variables and hence a sufficiently large electric power is necessary. On the other hand, melting of the material and associated droplet formation due to surface tension have to be avoided. Comparison of the electromigration process in bulk material and in thin films reveals fundamental differences with respect to the two control parameters. A thermally conducting substrate in contact with a metal layer assists heat dissipation. Therefore thin films can support a current density orders of magnitude higher than the bulk and significant material transport can be observed on much shorter time scales [32].

The ion displacement caused by electron impact leads to the formation of voids and hillocks and can ultimately break the electrical contact due to slits separating the structure. Gap formation preferably starts in spots where temperature and current density rise above average. The position of these nucleation centers can be determined by either the sample geometry (e. g. layer thickness and structure width) or the microstructure of the metal (e. g. defects or grain boundaries) [32, 33]. In summary, the electromigration process is influenced by material diffusivity, current density, temperature, conductor geometry and microstructure [33]. A control mechanism has to take into account all these quantities.

In 1999, first attempts to use electromigration deliberately for the formation of nanometer-spaced electrode pairs in thin metallic wires were made [6]. They already aimed at contacting single molecules. Electromigration was performed in an uncontrolled way by ramping a current through the sample and simultaneously monitoring the voltage drop in a four-probe configuration. A drastic conductance decrease eventually indicated breaking of the structure. Although this method was claimed to be highly reproducible, it quickly became clear that further control over the electromigration process is crucial to raise the yield of nanogaps instead of macroscopic voids.

Furthermore, uncontrolled electromigration was mostly conducted at cryogenic temperatures to avoid melting. First results on electrical transport characteristics of single molecules contacted with this method were soon published [34–36]. However, a few years later several groups found out that after electromigration at cryogenic temperatures metallic clusters often remain in the generated junctions [37–39]. Doubts arose about whether the observed Coulomb blockade and Kondo effect could really be attributed to trapped molecules. Metallic islands can show the same transport characteristics and obstruct conclusive data analysis.

At the same time an active-feedback-loop controlled electromigration method was developed [7, 37]. It has been reported to reliably produce nanogaps and to be practical even at room temperature under ambient conditions. In addition, a higher yield of empty gaps compared to uncontrolled electromigration at low temperatures have been claimed [7, 40]. Today, this method is still the state of the art and it has also been used for this work. The details of the feedback-controlled electromigration procedure are described in Sec. 3.1.3 together with our realization of it.

2.3 Previous Low Temperature Transport Measurements on Carbon Nanotubes

Carbon nanotubes are cylindrical macromolecules that consist solely of carbon and can be regarded as rolled-up graphene sheets. Their structure as well as their electronic properties can be derived from the honeycomb lattice of the two-dimensional carbon allotrope which can be seen as two interpenetrating triangular lattices spanned by the unit vectors [41, 42]

$$\vec{a}_1 = \frac{a}{2}(\sqrt{3}, 1), \qquad \vec{a}_2 = \frac{a}{2}(\sqrt{3}, -1) \tag{2.2}$$

where a is the lattice constant. It derives from the length of the in-plane carbon-carbon bonds $a_{C-C} = 1.42\,\text{Å}$ to

$$a = \sqrt{3} a_{C-C} \tag{2.3}$$

The carbon atoms in the graphene lattice are sp^2-hybridized. In-plane they are linked to three neighbors via σ-bonds. Additionally, the remaining p-orbitals perpendicular to the carbon sheet overlap with each other and form delocalized π- (bonding) and π^*- (antibonding) orbitals.
Wrapping of a two-dimensional graphene sheet into a cylindrical CNT is illustrated in Fig. 2.1. It is described by a lattice vector $\vec{C}_h$ which runs along the circumference of the tube. Expressed in terms of the basis vectors $\vec{a}_1$ and $\vec{a}_2$ it is

$$\vec{C}_h = n \cdot \vec{a}_1 + m \cdot \vec{a}_2 \quad \text{with} \quad m, n \in \mathbb{Z}. \tag{2.4}$$

The thus defined tuple (n,m) characterizes the structural and electronic properties of every tube. Foremost, its diameter d can be derived via

$$d = \frac{|\vec{C}_h|}{\pi} = \frac{a}{\pi}\sqrt{n^2 + nm + m^2}. \tag{2.5}$$

Second, the chirality of the CNT is equally determined by the integer pair (n,m) because the tilt angle θ of the hexagons with respect to the nanotube axis is given by

$$\cos\theta = \frac{\vec{C}_h \cdot \vec{a}_1}{|\vec{C}_h| \cdot |\vec{a}_1|} = \frac{2n + m}{2\sqrt{n^2 + nm + m^2}}. \tag{2.6}$$

Furthermore, periodic Born-von Karman boundary conditions restrict the electronic states of the CNT along its circumference. Applying the Bloch theorem to the wavefunction $\psi_{\vec{k}}(\vec{r})$, it can be expressed as [8, 41, 43]:

$$\begin{aligned} \psi_{\vec{k}}(\vec{r} + \vec{C}_h) &= \mathrm{e}^{i\vec{k}\vec{C}_h}\psi_{\vec{k}}(\vec{r}) = \psi_{\vec{k}}(\vec{r}) \\ \Leftrightarrow \quad \vec{k}\vec{C}_h &= 2\pi \cdot j \quad \text{with} \quad j \in \mathbb{Z} \end{aligned} \tag{2.7}$$

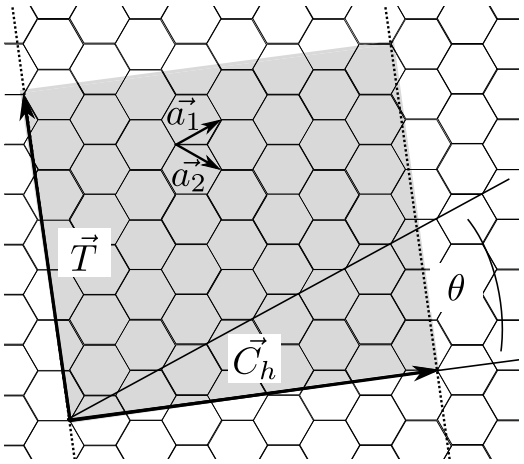

Figure 2.1 Illustration of the wrapping of a CNT along the chiral vector $\vec{C}_h$. The vector $\vec{T} \perp \vec{C}_h$ determines the length of the unit cell.

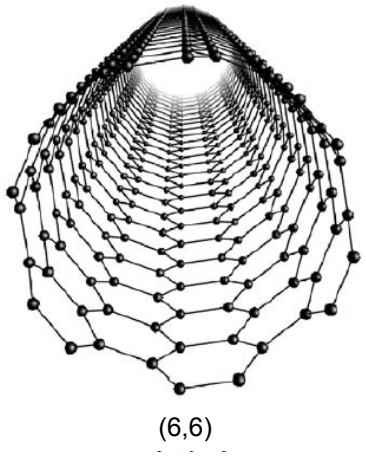

Figure 2.2 Sketch of a (6,6) carbon nanotube. Image taken from Ref. 41.

which simplified with Eq. (2.5) yields a quantization condition for $\vec{k}_\perp$, i. e. in the direction perpendicular to the nanotube axis:

$$\begin{aligned} |\vec{k}_\perp| \cdot |\vec{C}_h| &= k_\perp \cdot d\pi = 2\pi \cdot j \\ \Leftrightarrow k_\perp &= \frac{2}{d} \cdot j \quad \text{with} \quad j \in \mathbb{Z}. \end{aligned} \tag{2.8}$$

In the direction $\vec{k}_\parallel$ parallel to the nanotube axis on the other hand, the spectrum of allowed values is continuous, if the CNT is considered to be infinitely long.
The one-dimensional energy bands of CNTs can be obtained by slicing the two-dimensional energy dispersion relation of graphene. Figure 2.3 and 2.4 illustrate the projection of the allowed $\vec{k}$ vectors of a (5,5) CNT onto the Brillouin zone and the dispersion relation of graphene, respectively. The resulting one-dimensional band structure of the metallic tube can be found in Fig. 2.5. For comparison the band structure of a semiconducting (10,0) zig-zag tube is placed alongside in Fig. 2.6.
Whether a carbon nanotube is metallic or semiconducting depends on the position of the allowed $\vec{k}$ vectors in the graphene Brillouin zone with respect to the zero band-gap points, i. e. the vertices K and K'. To be an allowed electronic state of a CNT, the vector $\vec{K}$

$$\vec{K} = \frac{2\pi}{3a}(1, \sqrt{3}/3), \tag{2.9}$$

has to fulfill the quantization condition in Eq. (2.7), yielding

$$\begin{aligned} \vec{K} \cdot \vec{C}_h &= \frac{2\pi(n-m)}{3} = 2\pi \cdot j \\ \Leftrightarrow (n-m) &= 3 \cdot j \quad \text{with} \quad j, m, n \in \mathbb{Z} \end{aligned} \tag{2.10}$$

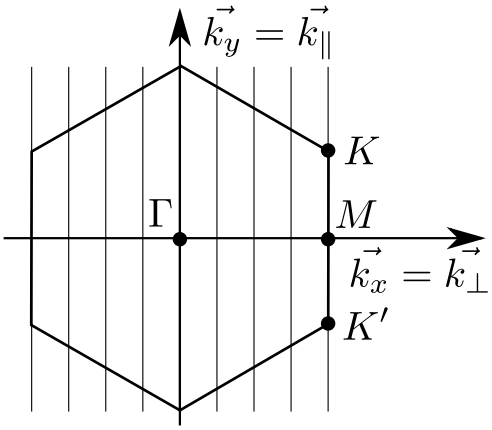

Figure 2.3 Projection of the allowed $\vec{k}$ vectors of a (5,5) CNT onto the Brillouin zone of graphene. Sketch adapted from Ref. 41.

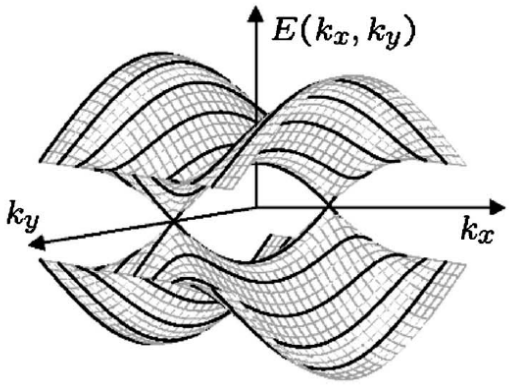

Figure 2.4 Slicing of the two-dimensional dispersion relation of graphene by the one-dimensional energy bands of a (5,5) CNT. Image taken from Ref. 41.

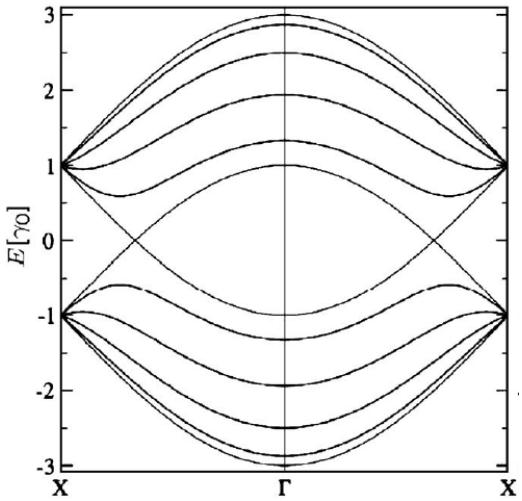

Figure 2.5 Band structure of a metallic (5,5) CNT. Graph taken from Ref. 41.

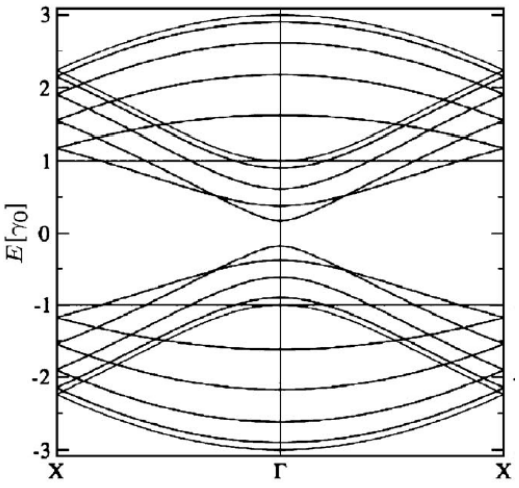

Figure 2.6 Band structure of a semiconducting (10,0) zig-zag CNT. Graph taken from Ref. 41.

i. e. a third of all CNTs is metallic and two thirds are semiconductors with varying band gaps. For this work, only metallic single-walled tubes with $d = 1.2 \pm 0.2$ nm were used.

The transport properties of carbon nanotubes have already been investigated at cryogenic temperatures by many groups. Some of the first results on single tubes have been published in Ref. 9. They were obtained with a CNT contacted by two platinum electrodes on top of a Si/SiO_2 substrate as shown in the *atomic force microscope (AFM)* image in Fig. 2.7. A third platinum electrode discernible in the upper left corner of the image served as a gate.

The published results of I-V measurements performed in a dilution refrigerator with a base temperature of 5 mK are displayed in Fig. 2.8. They show Coulomb blockade in the low-

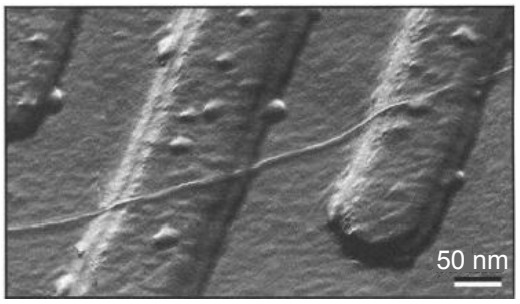

Figure 2.7 AFM tapping mode image of the sample used for the investigation of low temperature transport of CNTs in Ref. 9. The tube lies across two 15 nm thick platinum electrodes on top of a Si/SiO_2 substrate. A third contact discernible in the upper left corner of the image served as a gate.

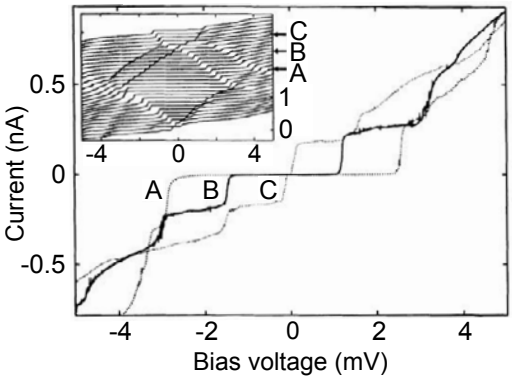

Figure 2.8 I-V curves measured on the CNT sample shown in Fig. 2.7 at 5 mK. A, B, and C denote traces taken with an applied gate voltage of 88.2 mV, 104.1 mV and 120.0 mV, respectively. Several more I-Vs are shown in the inset for $V_G = 50 - 136$ mV. Original plot found in Ref. 9.

voltage regime which is a signature of the weak coupling of the CNT to the metallic leads contacting it. This current-suppression feature is described in more detail in Sec. 2.4.

Furthermore, plateaus are visible in the I-V traces, which is a signature of a quantum dot, i. e. a spatially confined structure with a level spacing ΔU that is also larger than the thermal energy, $\Delta U > kT$. Transport through such a device is also modeled in Sec. 2.4.

If a complete gate voltage spectrum V_G is recorded, the effect of the gate voltage on the blockade regime manifests itself in *Coulomb diamonds* visible in the inset of Fig. 2.8. An example of a measurement of such features on another single CNT sample sketched in Fig. 2.9 is depicted in the color plot of Fig. 2.10.

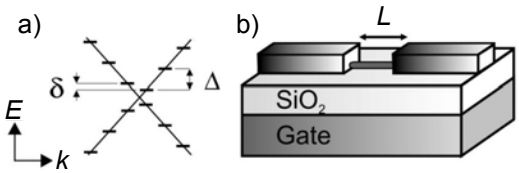

Figure 2.9 a) Scheme of the low-energy band structure of a metallic SWNT. The two bands crossing at the Fermi surface [44] are illustrated. Due to the finite length of the CNT, the wave vector $\vec{k}$ is quantized as indicated by the horizontal lines. δ is the energy mismatch of allowed states in the two bands.
b) Sketch of the sample on which the Coulomb diamonds shown in Fig. 2.10 were measured. A metallic nanotube of $L = 180$ nm and $\varnothing = 1.1$ nm is contacted via Cr/Au (5/75 nm) electrodes [10].

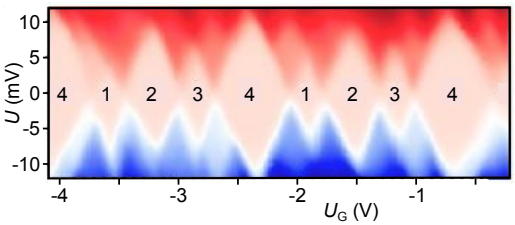

Figure 2.10 Color plot of current I vs. bias V and gate voltage V_G measured at 300 mK. Color scale from -40 nA (blue) to +40 nA (red). A fourfold pattern of Coulomb diamonds is observable [10].

It displays a fourfold periodicity which can be attributed to the crossing of two bands at the Fermi surface of metallic CNTs as illustrated in Fig. 2.9 a) [44]. Even though not always a fourfold pattern is observed, depending on the experimental conditions [45, 46], the Coulomb diamonds obtained from low temperature transport measurements on CNTs usually show some regularity, clear edges and in many cases signatures of excited states.

2.4 Sequential Tunneling Through Nanostructures

Transport through nanostructures, e. g. molecules, CNTs or small metallic islands, often displays a suppression of the current in the low-bias regime. A prerequisite for the observation of this Coulomb-blockade feature is a weak coupling of the respective structure to its surroundings via tunneling barriers with a resistance larger than the quantum resistance $R_K = h/e^2 \approx 26\,\mathrm{k\Omega}$. h here denotes Planck's constant. At the same time the self-capacitance C_Σ of the object is required to be small so that the *charging energy* $E_\mathrm{C} = e^2/(2C_\Sigma)$ is large compared to the thermal energy, $E_\mathrm{C} >> k_\mathrm{B}T$, where $k_\mathrm{B} = 1.38 \cdot 10^{-23}$ J/K is the Boltzmann constant. The blockade can be overcome if a sufficiently high bias voltage $V > e/(2C_\Sigma)$ is applied and its extent can be modified by a gate voltage V_G. For a better understanding of this phenomenon, the *Single Electron Transistor (SET)* in its normal conducting state shall be introduced here. The current through this device is derived in this section in the framework of the sequential tunneling model [47, 48]. The SQTM only takes into account independent successive tunneling events, and the time for tunneling is considered to be negligibly small in comparison to all other time scales.
The canonical version of a SET is a metallic dot coupled via tunneling barriers to two Fermi reservoirs. Transport through the island can be tuned with a third electrode, the gate. This configuration is sketched in Fig. 2.11.
"Metallic" in this context means that the electronic density of states of the dot is quasi-continuous at the Fermi energy, i. e. the level splitting ΔU is washed out by thermal broadening, $\Delta U < k_\mathrm{B}T$, as illustrated in Fig. 2.12. Under these conditions, the occupation of energy states

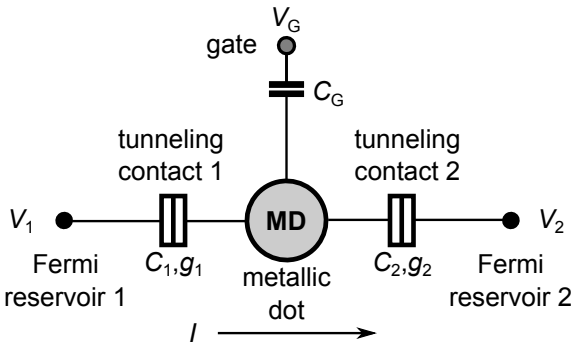

Figure 2.11 Scheme of a SET. A metallic island is coupled to two Fermi reservoirs by tunneling barriers with tunneling strength coefficient g_i and capacity C_i. Additionally, it is capacitively coupled to a gate electrode with capacity C_G.

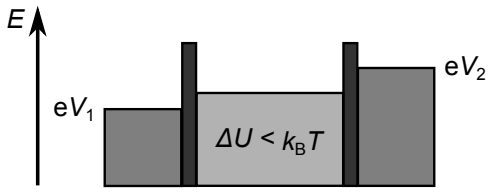

Figure 2.12 Energy spectrum of a metallic dot, i. e. with level spacing $\Delta U < k_\mathrm{B}T$, coupled to two Fermi reservoirs.

in both the dot and the electrodes can be described by the Fermi distribution

$$F(E) = \frac{1}{\exp[\beta(E - E_\mathrm{F})] + 1}, \tag{2.11}$$

where $\beta^{-1} = k_\mathrm{B}T$ and E_F is the Fermi energy.
The total capacity of the island to the environment is

$$C_\Sigma = C_1 + C_2 + C_\mathrm{G} + C_\mathrm{stray}. \tag{2.12}$$

This sets a typical scale which equals the energy stored in a capacitance C_Σ charged by one elementary charge e

$$E_\mathrm{C} = \frac{e^2}{2C_\Sigma}. \tag{2.13}$$

An applied bias V and gate voltage V_G induce an offset charge en_0, $n_0 \in \mathbb{R}$, which is given by

$$en_0 = C_1V_1 + C_2V_2 + C_\mathrm{G}V_\mathrm{G} \tag{2.14}$$

where V_i, $i \in \{1, 2\}$, is the voltage drop across contact i.
Furthermore, an uncontrolled contribution to the offset charge en_g, $n_\mathrm{g} \in \mathbb{R}$, is found in many experiments with single electron devices. The charging energy for n electrons on the island in dependence of the offset $n_0 + n_\mathrm{g}$ can be written as

$$E_\mathrm{ch}(n_0) = E_\mathrm{C}(n - (n_0 + n_\mathrm{g}))^2. \tag{2.15}$$

The total energy change $\Delta E_i(n)$ of the entire system if one additional electron is tunneling through barrier i onto the island already filled with n electrons is then

$$\Delta E_i(n) = 2E_\mathrm{C}(n - (n_0 + n_\mathrm{g}) + 1/2) + eV_i. \tag{2.16}$$

where the last term on the right-hand side is the work provided by the voltage source.
The transition rate $\Gamma_{i,n\to n+1}$ from state n to $n + 1$ across the junction i can be derived from *Fermi's Golden Rule*. As the density of states in both lead and dot is described by a Fermi distribution,

$$\Gamma_{i,n\to n+1} = \frac{g_i}{h}\frac{\Delta E_i(n)}{\exp(\beta\Delta E_i(n)) - 1} \tag{2.17}$$

results with a dimensionless factor g_i describing the tunneling conductance of contact i in multiples of the conductance quantum $G_0 = e^2/h$.
The total transition rates $\Gamma_{n\to n+1}$ and $\Gamma_{n\to n-1}$ are thus

$$\Gamma_{n\to n+1} = \sum_{i\in\{1,2\}} \frac{g_i}{h}\frac{\Delta E_i(n)}{\exp(\beta\Delta E_i(n)) - 1} \tag{2.18}$$

and

$$\Gamma_{n\to n-1} = \sum_{i\in\{1,2\}} \frac{g_i}{h}\frac{\Delta E_i(n)}{1 - \exp(-\beta\Delta E_i(n))}. \tag{2.19}$$

The total current through the island is determined by these tunneling rates and the probabilities p_n to find n electrons on the dot. They can be calculated using a master equation approach, which describes the time evolution of the p_n as

$$\begin{aligned}\frac{\mathrm{d}p_n}{\mathrm{d}t} =&\Gamma_{n+1\to n}p_{n+1} - \Gamma_{n\to n+1}p_n + \\ &\Gamma_{n-1\to n}p_{n-1} - \Gamma_{n\to n-1}p_n\end{aligned} \tag{2.20}$$

In the stationary state $\mathrm{d}p_n/\mathrm{d}t = 0$ and a simple *detailed balance* relation for p_n and $p_{n\pm1}$,

$$p_{n\pm1} = p_n \frac{\Gamma_{n\to n\pm1}}{\Gamma_{n\pm1\to n}}, \tag{2.21}$$

solves Eq. 2.20. It can be proven that Eq. 2.21 is not only a sufficient but also a necessary condition to fulfill Eq. (2.20).
The set of equations (2.21) can be solved with the normalization condition $\sum_n p_n = 1$, and as $I_1 = I_2$, the total current can then be evaluated for either of the two barriers i with

$$I = -e \sum_n p_n(\Gamma_{i,n\to n+1} - \Gamma_{i,n\to n-1}). \tag{2.22}$$

The plot in Fig. 2.13 shows I-V curves calculated with Eq. (2.22) for different gate voltages at $T = 0$. The two tunneling contacts are assumed to have identical capacitance $C_1 = C_2 = 10C_\mathrm{G}$ and conductance $G_1 = G_2 = 2G$.
Upon applying a gate voltage V_G the extent of the voltage range over which current is suppressed changes periodically. The Coulomb blockade is largest for $V_\mathrm{G} = 0$ and integer multiples of $V_\mathrm{G} = e/C_\mathrm{G}$. It is completely lifted on the other hand for half-integer multiples of

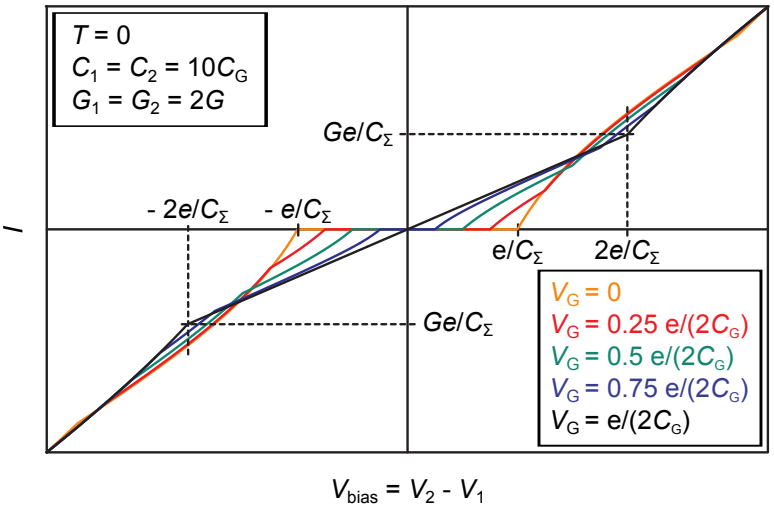

Figure 2.13 I-V curves calculated with Eq. (2.22) for various gate voltages V_G at $T = 0$. Reduction and lifting of the current suppression with V_G are demonstrated. The two tunneling contacts are assumed to have identical capacitance $C_1 = C_2 = 10\ C_\mathrm{G}$ and conductance $G_1 = G_2 = 2G$.

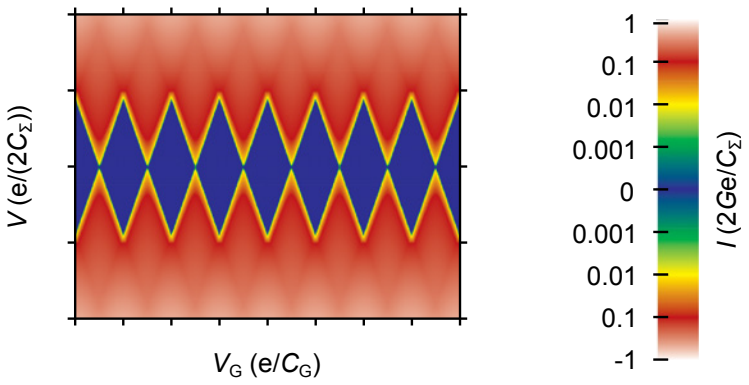

Figure 2.14 Logarithmic color-coded plot of I vs. bias V and gate voltage V_G calculated with Eq. (2.22) for tunneling contacts with $C_1 = C_2 = 10\,C_G$ and $G_1 = G_2 = 2G$ at $T = 0$. Coulomb diamonds are visible.

V_G. This periodicity reflects itself in Coulomb diamonds in a plot of I vs. V_G and bias V. An example with logarithmic color scale is shown in Fig. 2.14.

The theory described above is applicable to small metallic structures. However, it has to be modified if the level spacing ΔU is larger than the thermal broadening, $\Delta U > k_B T$. This relation holds e. g. for molecules and CNTs at low temperatures. On the basis of Refs. 49 and 50 the current through such a *quantum dot (QD)* in the configuration sketched in Fig. 2.11 can be calculated in the framework of the same master equation approach as the SET. The only difference is the discreteness of the energy spectrum, which reflects itself in the transition rates $\Gamma_{i,n\to n+1}$ between states of the system.

Applying Fermi's Golden Rule for the transition between a dot level and an individual lead state, which are coupled by the tunneling Hamiltonian, followed by a summation over the lead states results in

$$\Gamma_{i,n\to n+1} = \frac{\tilde{g}_i}{h}\frac{1}{\exp(\beta\Delta E_i(n))+1} \tag{2.23}$$

with a factor $\tilde{g}_i$ of dimension of energy quantifying the coupling strength.

If we consider the simple case of a quantum dot that can be either in the empty or singly occupied state, labeled 0 and 1, the total transition rates are

$$\Gamma_{0\to 1} = \frac{\tilde{g_1}}{h}\frac{1}{\exp(\beta\Delta E_1(0))+1} + \frac{\tilde{g_2}}{h}\frac{1}{\exp(\beta\Delta E_2(0))+1} \tag{2.24}$$

and

$$\Gamma_{1\to 0} = \frac{\tilde{g}_1}{h}\frac{1}{\exp(-\beta\Delta E_1(1))+1} + \frac{\tilde{g_2}}{h}\frac{1}{\exp(-\beta\Delta E_2(1))+1}. \tag{2.25}$$

The total current through the island is determined by these tunneling rates and the probabilities p_j, $j \in \{0, 1\}$, to find the dot in the empty or occupied state. They can be calculated using the above master equation approach, which for only two states simplifies to

$$\frac{\mathrm{d}p_0}{\mathrm{d}t} = \Gamma_{1\to 0}p_1 - \Gamma_{0\to 1}p_0 \tag{2.26}$$

and

$$\frac{\mathrm{d}p_1}{\mathrm{d}t} = \Gamma_{0\to1}p_0 - \Gamma_{1\to0}p_1. \tag{2.27}$$

As $p_0 + p_1 = 1$ and in the steady state $\mathrm{d}p_i/\mathrm{d}t = 0$,

$$p_0 = \frac{\Gamma_{1\to0}}{\Gamma_{0\to1} + \Gamma_{1\to0}} \quad \text{and} \quad p_1 = \frac{\Gamma_{0\to1}}{\Gamma_{0\to1} + \Gamma_{1\to0}} \tag{2.28}$$

results and the total current can be evaluated with

$$I = -e(p_1\Gamma_{i,1\to0} - p_0\Gamma_{i,0\to1}). \tag{2.29}$$

I-V curves numerically derived from this model for a finite temperature $T = 0.01E_\mathrm{C}$ with and without applied gate voltage are presented in Fig. 2.15. They show an unrealistically steep onset of current. Experimentally, on the other hand, a temperature-independent broadening of the current steps is observed below a threshold of the order of 1 K. Thus, the model outlined in this section does not sufficiently describe transport through a quantum dot at low temperatures. To overcome this discrepancy, temperatures elevated above the experimental conditions are usually used for modeling in the literature [51]. A more accurate theory has to take into account lifetime broadening of the dot levels, which is not trivial to implement. However, an improved approach which does just that is presented in Sec. 4.3.3.

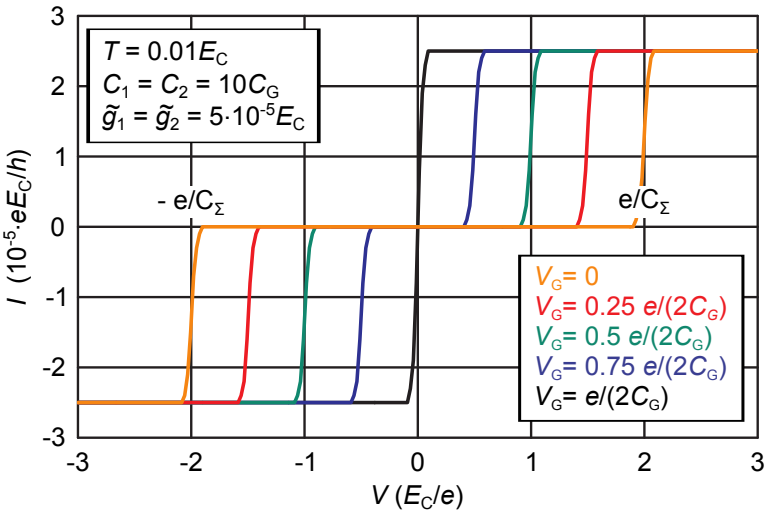

Figure 2.15 Current through a quantum dot which can be either in the empty or singly occupied state, 0 or 1, for $T = 0.01E_\mathrm{C}$, $C_1 = C_2 = 10\ C_\mathrm{G}$ and $\tilde{g}_1 = \tilde{g}_2' = 5 \cdot 10^{-5} E_\mathrm{C}$ plotted for several values of V_G.

3 Experimental Details

In this chapter the various steps required for the preparation of samples used for electromigration and macromolecule measurements on the one hand and for CNT experiments on the other hand are detailed in Sec. 3.1 and Sec. 3.2, respectively. Furthermore, the device setup for the performed measurements and in particular the dilution refrigerator are also described.

3.1 Preparation of Macromolecule Measurements

The metallic structures used for electromigration and macromolecule measurements are prepared in two main steps. In the first, a standard pattern of leads and bonding pads is pre-structured by optical lithography. This preliminary work is intended to reduce exposure time in the next preparation step. The specific design of each sample is later completed by *electron beam lithography (EBL)*. It allows positioning of the finer sample structures, which measure only a few microns, within the region defined by the already existing layout.
After fabrication of the metallic structures, nanogaps for the contacting of molecules are generated by feedback-controlled electromigration. For control over the location where ion displacement sets in, constrictions are pre-structured in the used rings and wires. As a determination of the exact gap size after the electromigration process is not possible, long molecular rods were chosen for placing on the prepared electrodes. Originally, deposition by sublimation was intended, but it had to be substituted by deposition from solution. After drying of the solvent, I-V curves of the samples were recorded.
This section starts with a description of the modus operandi of optical lithography in Sec. 3.1.1, followed by an outline of the consecutive steps of electron beam lithography in Sec. 3.1.2. The procedure of feedback-controlled electromigration is detailed in Sec. 3.1.3. Finally, synthesis of appropriate molecules and their deposition from solution are discussed in Sec. 3.1.4.

3.1.1 Optical Lithography

At the beginning of this section, special attention shall be paid to the substrates used for sample preparation. As in the semiconductor industry, oxidized silicon wafers are also standard in nanostructure research. However, the implications of their chemical and physical properties for the specific application have to be taken into account thoroughly. In our work on electromigration the influence of the substrate on the success of experiments was confirmed, as detailed in Sec. 4.1.3.
For this thesis, boron p-doped, (100)-oriented silicon wafers with a resistivity of 1-20 Ωcm, a diameter of 2" and 275 µm thickness were bought at *CrysTec* with either 400 nm thermally grown or only a few nanometers of native silicon oxide (SiO_2). For some experiments an

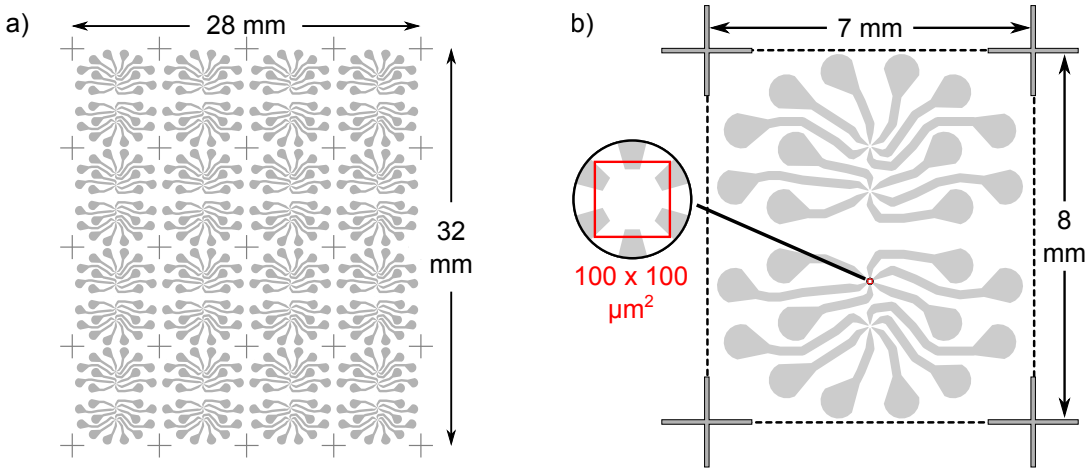

Figure 3.1 a) Layout of the mask for optical lithography on a 2" silicon wafer. b) Single $7 \times 8\,\mathrm{mm}^2$ chip. The cutout shows one of the four $100 \times 100\,\mu\mathrm{m}^2$ positions reserved for electron beam lithography, a *writing field*.

electrically well insulating layer on the sample surface is crucial because it inhibits current flow between the metallic structure on top and the doped silicon. In other cases a thin thermal barrier is more important, because it allows for better dissipation of Joule heat, as discussed in Sec. 4.1.3.

On each 2" silicon wafer, 16 identical lead configurations are fabricated. Figure 3.1 a) shows the layout of the chromium mask for optical lithography and Fig. 3.1 b) the geometry of a single chip of $7 \times 8\,\mathrm{mm}^2$. It leaves room for the finer structures in four designated $100 \times 100\,\mu\mathrm{m}^2$ squares, the *writing fields* for the SEM.

The optical lithography procedure starts by consecutively covering one of the above specified silicon wafers with 3 metallic layers: 1-2 nm titanium as adhesion promoter, 30 nm copper and finally 20 nm gold on top. A pure copper film corrodes in the following wet chemistry process and gold alone forms a poorly conducting alloy with aluminum, called *purple plague*. As aluminum is a popular superconductor in mesoscopic physics, it is often used in our group for the inner structure of samples, which makes the Ti/Cu/Au layer sequence necessary.

All three metal layers are deposited by thermal electron beam evaporation in a vacuum chamber, which is sketched in Fig. 3.2. The required material is placed in a small cup formed by hand from tungsten foil. The chamber offers room for a maximum of three sources at the same time. A loop wound from tungsten wire with a diameter of 0.2 mm is centered around each crucible at a distance of a few millimeters. To achieve evaporation, this coil is heated by a current of $I_{\mathrm{wire}} = 3.5 - 4.5\,\mathrm{A}$ after pumping to a background pressure of about 10^{-6} mbar. Thermally emitted electrons are accelerated by a voltage U of up to one kilovolt towards the crucible, where they are collected, leading to a current I between anode and cathode. The source is heated by the power $P = U \cdot I$, which is regulated to an appropriate constant, material dependent value throughout the process. The crucibles are surrounded by a massive copper block, which shields the chamber walls from metal vapor. It is additionally water cooled to avoid outgassing of surrounding parts due to excessive heating which degrades the purity of the metal

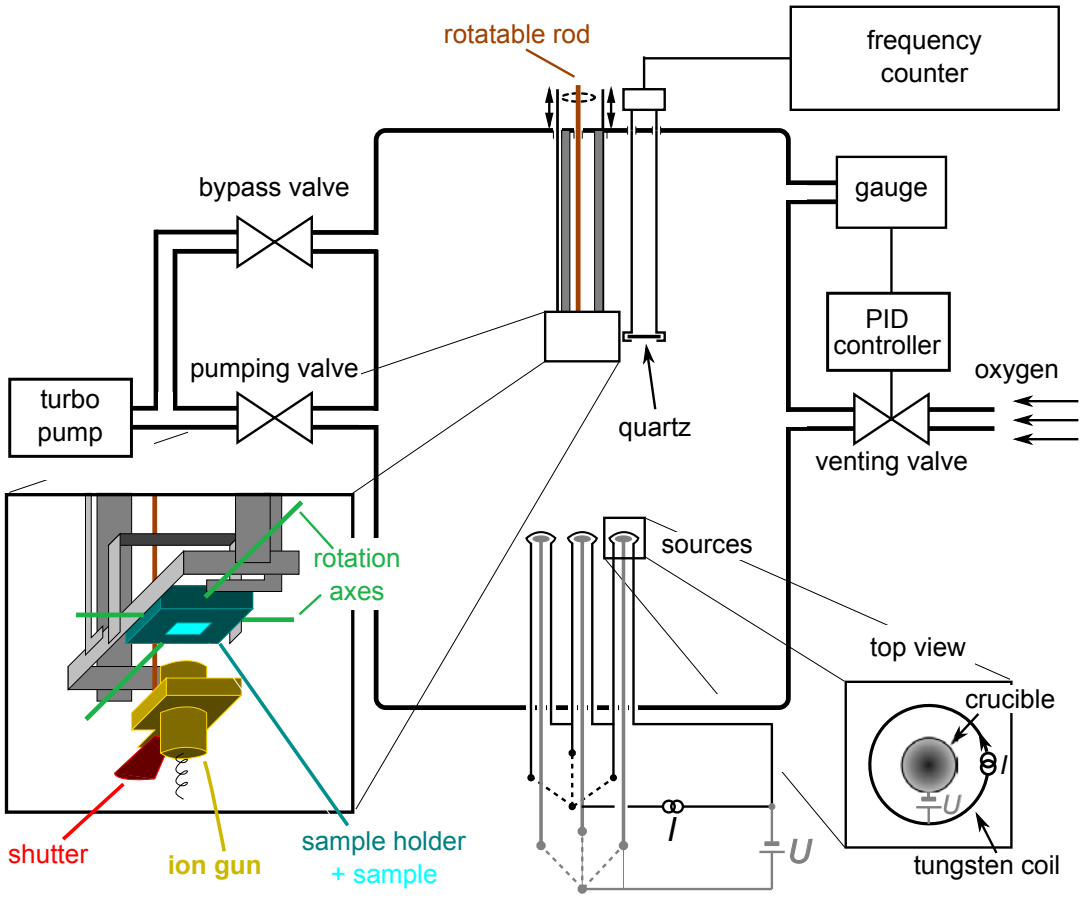

Figure 3.2 Sketch of the evaporation chamber.

vapor.
The sample holder in the vacuum chamber can be rotated around two axes perpendicular to each other. Thus, metal can be evaporated onto the substrate surface under different angles. This is necessary for *shadow evaporation*, which is explained in Sec. 3.1.2.
For determination of the thickness of the deposited layer, a quartz oscillator is mounted in close vicinity to the sample. An *Agilent 53131A Universal Counter* monitors its oscillation frequency. According to calibration measurements for gold, copper and titanium performed in the course of a previous diploma project [52], the shift Δf due to weight change translates into layer thicknesses as stated below:

$$d_{\mathrm{Au}} = \Delta f \cdot 0.011 \text{ nm/Hz}$$

$$d_{\mathrm{Cu}} = \Delta f \cdot 0.024 \text{ nm/Hz}$$

$$d_{\mathrm{Ti}} = \Delta f \cdot 0.047 \text{ nm/Hz}$$

These rates are valid for the rightmost source, which has the same distance to quartz and

sample. This is not the case for the central (left) source, therefore the film thickness then has to be corrected by a factor of 1.1 (1.2).
Following metallization of the silicon wafer, its surface is coated with the negative photo resist AZ 6632 solved in PGMEA (AZ EBR solvent) with a weight ratio of 5 : 1. Both chemicals are products of *MicroChem*. After spinning at 5000 rpm for 90 s, the layer thickness is about 1 µm. Subsequently, the resist is dried in a furnace at 100 °C for 20 min.
After the bake-out, the substrate has to be aligned under a chromium mask before exposure to UV light. Therefore its surface is carefully scratched along the wafer diameter with a diamond cutter for orientation. When the wafer has been positioned accurately in the shadow of the mask, both are brought into hard contact and exposed for 5 s. The uncovered resist can then be solved by the developer AZ 351 B also provided by *MicroChem*. It is diluted with distilled water in the volume ratio 1 : 4. The silicon substrate is washed in this mixture until the unexposed structures are visible on its surface. Immediately afterwards it is rinsed with distilled water and finally blow-dried.
Next, the unwanted metal around the structures still protected by resist is removed by ion etching. The vacuum chamber available for that purpose is first pumped to $2 \cdot 10^{-5}$ mbar before a controlled argon flow is started, which raises the pressure again to $6 \cdot 10^{-4}$ mbar. With the help of a *Commonwealth Scientific IBS Controller*, a plasma is ignited. The operation parameters are set to the following values: 20 mA beam current, 250 V acceleration voltage, 40 V discharge voltage and 2 mA neutralizer current.
Once all metal around the chip layout is removed, the silicon wafer is cut with a diamond and broken into 16 chips of $7 \times 8\,\mathrm{mm}^2$. To conclude their fabrication, the metallic structures still have to be cleaned from the remaining resist on top. Therefore the samples are first immersed in acetone for at least 12 h. Still, subsequent mechanical treatment is required starting with a 1 min application of ultrasound and subsequent spraying of the surface with a pipette or syringe. It is crucial to keep the chip surface covered by solvent during the entire cleaning process until it is finally spin-dried.

3.1.2 Electron Beam Lithography

When required, the desired sample layout is completed by electron beam lithography on one of the pre-structured chips. Contrary to the optical lithography, positive resists are used. The most common ones are mixtures on the basis of *polymethylmethacrylate (PMMA)* with different chain length in solution. Typical solvents are anisole, chlorobenzene or ethyllactate, short A, C and EL. The systematic notation for PMMA resists is PMMA x K Sy, where x specifies the molecular weight in kg/mol, S the solvent and y the content of solids, i. e. polymers, in percent. These three parameters determine viscosity and sensitivity of the resist.
For the preparation of samples intended for electromigration and macromolecule measurements, a two-layer resist system is used for electron beam lithography. The bottom one is more sensitive to electron impact and therefore a larger volume of it is chemically modified during beam exposure, i. e. an *undercut* is created, as illustrated in Figs. 3.3 and 3.4. Thus, the upper resist defines the mask for metal evaporation and the lower supports it at a certain distance from the substrate surface. The purpose of the undercut is twofold. On the one hand, the metal

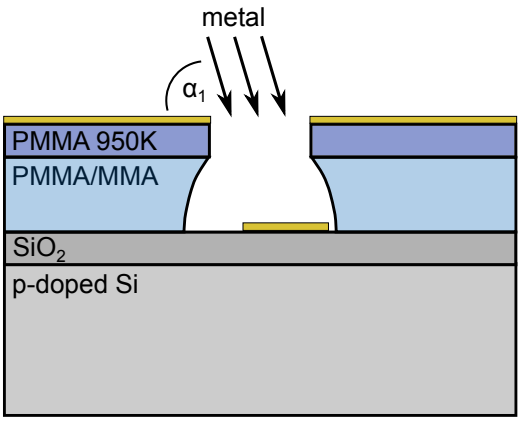

Figure 3.3 Shadow evaporation: First metal deposition step.

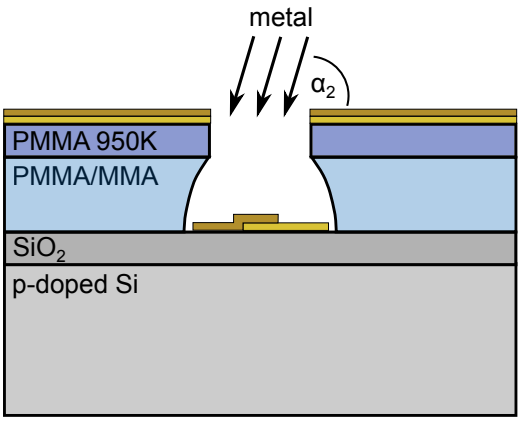

Figure 3.4 Second metal evaporation step under different angle.

structure is not in contact with the resist, as one can see in Figs. 3.3 and 3.4, which makes the lift-off easier. On the other hand, suspended resist bridges can be generated, where material can be deposited underneath by *shadow evaporation*.

This technique, whose two steps are shown in Figs. 3.3 and 3.4, was also employed for some of our samples. First, metal is deposited from an angle α_1 with respect to the substrate surface. When the desired thickness of the first layer is reached, the sample is rotated and the evaporation is finished from a second angle α_2. The two resulting metal films do not match exactly, but are shifted against each other with an overlap tunable by angle and resist thickness.

For all samples prepared in the way described in this section, PMMA 950 K A4 or A4.5 was chosen for the top resist. The resulting thickness varies only marginally. For the bottom layer PMMA 200 K C7 was used. Spin coating parameters and resulting layer thicknesses for all resists are listed in Tab. 3.1. The PMMA thicknesses specified in the data sheets were checked with a contact profilometer. Measured values are only accurate to within 50 nm, but match those given in the literature, which are stated with an error of ±10 nm.

After spin coating each resist layer is baked out in a furnace at 150 °C for 45 min. Next, electron beam writing is performed with a *Zeiss LEO 1530* SEM equipped with the lithography package *ELPHY Plus* from *Raith*. In addition to the usual stage positionable in the micron range, a

Table 3.1 Summary of the resists used for electron beam lithography and the respective spin coating parameters.

Notation	Reseller	Rotation speed	Rotation time	layer thickness	
				profilometer	data sheet
PMMA 200 K C7	*Allresist* and *MicroChem*	2000 Hz	60 s	500 nm	520 nm
PMMA 950 K A4	*MicroChem*	4000 Hz	90 s	200 nm	200 nm
PMMA 950 K A4,5	*Allresist*	4000 Hz	90 s	200 nm	230 nm

piezo-controlled platform with nanometer precision, the *Nanostage*, is built into the device.
Already during the design process of the sample layout the *proximity effect* has to be taken into account. This term refers to the fact that small structures in close proximity to larger exposed areas get a higher dose than isolated structures. The spatial distribution of the radiation dose around a spot exposed to a focused electron beam of finite radius is extended further due to several scattering effects. Modification of the polymer chains is almost entirely due to secondary electrons generated along the primary beam path within the resist as their lower energy results in a larger scattering cross section. Within several nanometers, they come to a full stop and modify the resist over this range. Further broadening of the exposure profile is caused by backscattering of primary electrons from the thick substrate. The dose actually deposited in one spot therefore depends on the exposure of its environment. Thus, an appropriate correction factor depending on the size, geometric form and position of the exposed region has to be specified for the different parts of a structure.
As mentioned in Sec. 3.1.1, the leads pre-structured by optical lithography are placed around four writing fields of $100 \times 100\,\mu m^2$ for the inner structures. Each of these areas can be scanned completely with a 20 µm aperture at a single magnification in a reasonable time. Adjustment of the apertures with respect to each other and/or stitching are therefore not necessary and mutual displacement of writing fields due to inexact alignment and/or beam drift is avoided.
When the layout file has been transferred to the SEM-control PC and the sample placed in the vacuum chamber of the device, it is pumped to a background pressure below $2 \cdot 10^{-5}$ mbar. The acceleration voltage is then run up to usually 30 kV and the beam current is measured with a *Faraday cup*. Afterwards the layout is aligned with respect to the already existing metallic structures on three distinct points (*three-point adjustment*) of the pre-structured lead geometry itself. This is sufficiently exact to move the beam close to the first writing field. A more exact positioning is then performed on a selected lead edge. As an overlap in the micron range between inner structure and leads is incorporated in the layout, separate alignment marks are not necessary. Before the inner structure is written, a dent is burnt into the resist at a distance of 100 µm to the writing field and used for local focus correction. Finally, the respective geometry is exposed. The same procedure is repeated for each of the four inner structures.
After electron beam lithography, the exposed resist is developed with a mixture of *methyl isobutyl ketone (MIBK)* and isopropanol (IPA) in a volume ratio of 1 : 3. For complete solving, the sample is washed in the mixture for 45 s, rinsed in isopropanol and subsequently spin-dried.
Subsequently the substrate is metallized in the vacuum chamber mentioned in Sec. 3.1.1. It is placed in a holder especially designed for $7 \times 8\,mm^2$ silicon chips. They are held by a metallic lid which at the same time serves as an evaporation mask. Four circular openings with a diameter of 1 mm and an elongated hole leave only the inner structures and possible test patterns in the sample center uncovered, as the photo in Fig. 3.5 shows. Thus metal is deposited only on small, separated areas, which again makes the lift-off easier.
Before metal evaporation, the sample surface is cleaned by argon sputtering. Particularly dirt on the exposed parts of the leads fabricated by optical lithography has to be removed for better electrical contact to the inner structure. The ion gun used to ignite the plasma is sketched in Fig. 3.6. It is mounted on a rotatable rod in the vicinity of the sample and can be moved to a position closely below the same. After the chamber has been evacuated to 10^{-6} mbar, an argon

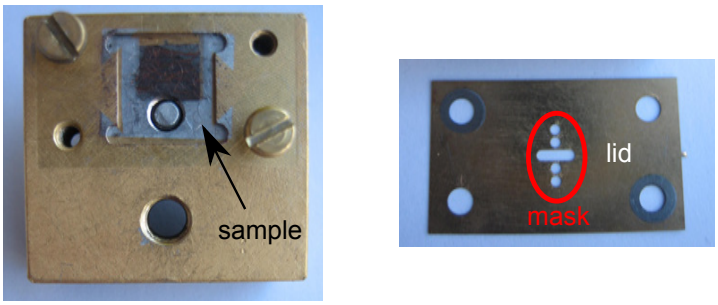

Figure 3.5 Photo of the sample holder for $7 \times 8\,\mathrm{mm}^2$ chips used for evaporation in the vacuum chamber sketched in Fig. 3.2.

flow is adjusted to establish a pressure between $2.7 - 3.0 \cdot 10^{-1}$ mbar. By applying a voltage between the anode of the ion gun which has the form of a thin wire, and the cathode which lies on chamber potential, a plasma is generated in the surrounding copper cylinder. Power is regulated to 2 W. Once the plasma burns continuously, the copper cup is brought in front of the sample. Through an opening in the cylinder lid, the plasma exits in the form of a *plume*, which is directed onto the surface for 2 min. Afterwards the ion gun is retracted, the acceleration voltage switched off and the argon flow stopped.

Once the background pressure is recovered, metallization can be started. The process has already been described in Sec. 3.1.1. It should however be pointed out that in contrast to optical lithography, no sticking layer is used for the inner structures because it proved unnecessary. Hence the material composing the inner structures remains cleaner.

A reliable removal of the metallic squares covering the area enclosed in the center of ring structures during lift-off proved challenging. Two approaches were found to overcome this difficulty. The first possibility, which is illustrated in the SEM image of Fig. 3.7, is the appli-

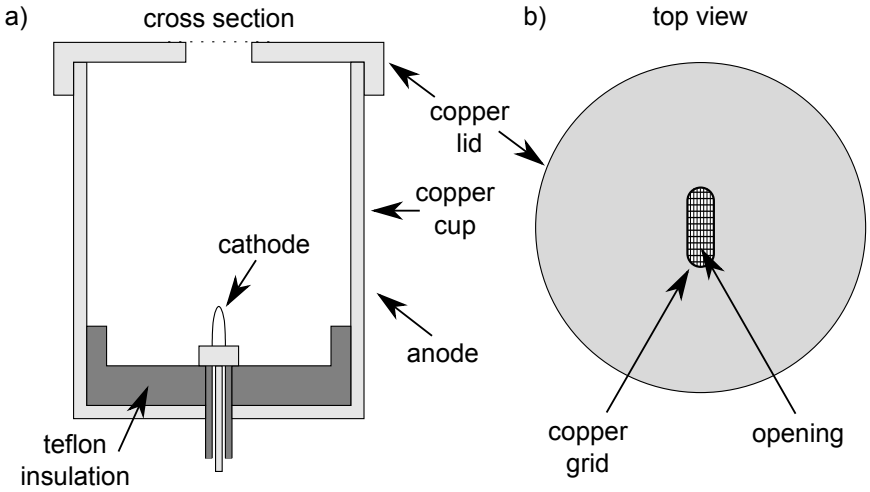

Figure 3.6 Sketch of the ion gun included in the evaporation chamber for cleaning of the sample surface with an argon plasma. a) Cut through the surrounding copper cup, which serves as the anode. b) Top view of the closed copper cylinder. Through a grid for acceleration of the gas ions the plasma plume is directed out of the gun.

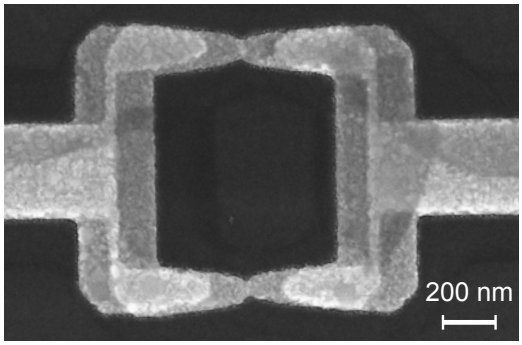

Figure 3.7 Ring deposited by shadow evaporation.

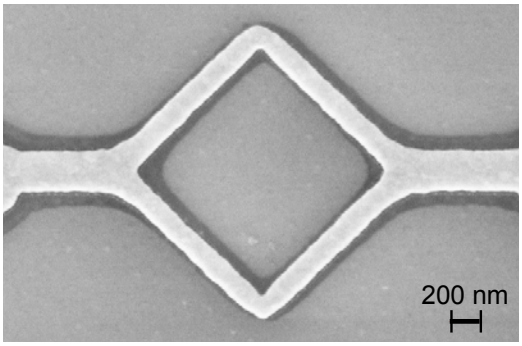

Figure 3.8 Tilted ring after successful lift-off.

cation of shadow evaporation. With the help of this technique the two ring arms were each closed under a suspended resist bridge. These two connections to the material surrounding the ring lifted the small central patch away from the substrate together with the outside metal once the underlying resist was dissolved and the inner square had started floating. With this method, its dropping back and sticking to the surface could be avoided. Note also that the ring arms in Fig. 3.7 taper towards their center. These constrictions were intended to determine the region where electromigration starts.

A second method to successfully complete the lift-off process of ring structures is holding the sample bottom up into a preheated acetone bath whilst applying ultrasound for 20–60 s. A sample prepared in this way can be seen in Fig. 3.8. Furthermore, the sample design was also changed to improve determination of the spot where electromigration sets in. The square was rotated by 45 ° as a consequence of simulations of current density and temperature in such structures that are presented in Sec. 4.1.3.

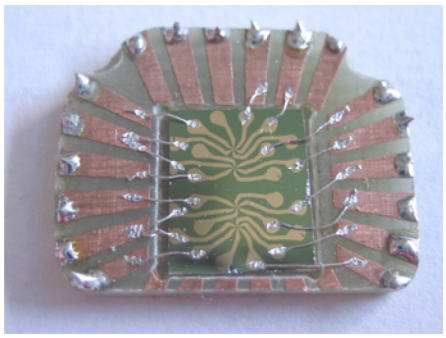

Figure 3.9 Sample glued and bonded to a glass fiber reinforced plastic board.

After successful preparation, the samples are attached to glass-fiber-reinforced plastic boards with *GE varnish*. The holders measure 17 × 17 mm^2, but size and shape are adjusted according to the application. 24 copper contacts are arranged on the top side of each board around a depression for the substrate. The 24 gold pads on the sample surface can be bonded to these copper contacts with indium wire, which is pressed against the metal with the tip of a pencil. For connection to measurement devices, leads are soldered to the outer end of the copper pads. The photo in Fig. 3.9 shows a sample glued and bonded to a plastic board, on which solder is already prepared for wiring.

3.1.3 Feedback-Controlled Electromigration

The first realization of an active-feedback loop to control electromigration was described in Ref. 7. A bias voltage V is ramped across the sample at a constant rate $\mathrm{d}V/\mathrm{d}t = r$. Simultaneously, the current I and thus the conductance G are monitored. When G has decreased by a certain threshold percentage $t = \Delta G/G$, V is quickly swept back by a predetermined ΔV at a rate higher than r and the next ramp is started. The process is finished when G has fallen below one conductance quantum G_0. Neither cooling of the sample nor vacuum were claimed to be necessary. The technique implemented in the framework of this thesis follows the method published in Ref. 53, an advanced version of the this procedure. It is aimed at limiting the power dissipated in the electromigrating structure.
At the early stage of electromigration, ion displacement starts above a certain temperature threshold, i. e. as soon as a certain critical power P_C is dissipated in the structure, as pointed out already in Ref. 7. In Ref. 53, it is confirmed that for $G \gtrsim 20\,G_0$ each electromigration cycle ends on a constant power curve and the feedback control loop is adapted accordingly. It operates based on voltage biasing and two-point measurement of the rising sample resistance. As soon as the termination criterion

$$R = (1 + \delta)R_{\mathrm{init}} \tag{3.1}$$

is reached, the voltage is instantly reset to

$$V_{\mathrm{init}} = \sqrt{p \cdot V_{\mathrm{end}} \cdot I_{\mathrm{end}} \cdot R_{\mathrm{init}}} \tag{3.2}$$

instead of gradually reducing it by a fixed value ΔV. R_{init} is the sample resistance at the beginning of a voltage ramp, $\delta = \Delta R/R_{\mathrm{init}}$ specifies the allowed percentage of resistance change ΔR and $P_{\mathrm{end}} = V_{\mathrm{end}} \cdot I_{\mathrm{end}}$ is the power dissipated by the circuit at the end of a cycle. The new ramp starts at a voltage V_{init} that corresponds to a power dissipation of a fraction p, $0 \leq p \leq 1$, of the previous maximal value P_{end} [53]. Figure 3.10 illustrates the termination criterion and the resulting start voltage V_{init} for the subsequent cycle.
The data in Fig. 3.10 is taken from two cycles of the electromigration of a gold wire performed at room temperature in vacuum. Already in the low-bias regime (red squares) the resistance shows a distinctly nonlinear behavior. This can be ascribed to Joule heating of the still unmodified metallic wire. In a very basic approach this is expected to cause a quadratic resistance increase with the applied voltage:
The temperature dependence of a conventional resistor is in linear approximation

$$R(T) = R(T_0)(1 + \alpha\Delta T) \tag{3.3}$$

where $\Delta T = T - T_0$ and α is the material-dependent temperature coefficient [54]. To first order, ΔT is proportional to the dissipated electrical power $P = V \cdot I$. For an ohmic resistor $R = V/I$ it is thus $\Delta T \propto P \propto V^2$ and consequently

$$R(V) = R(V_0)(1 + \alpha\beta V^2) \tag{3.4}$$

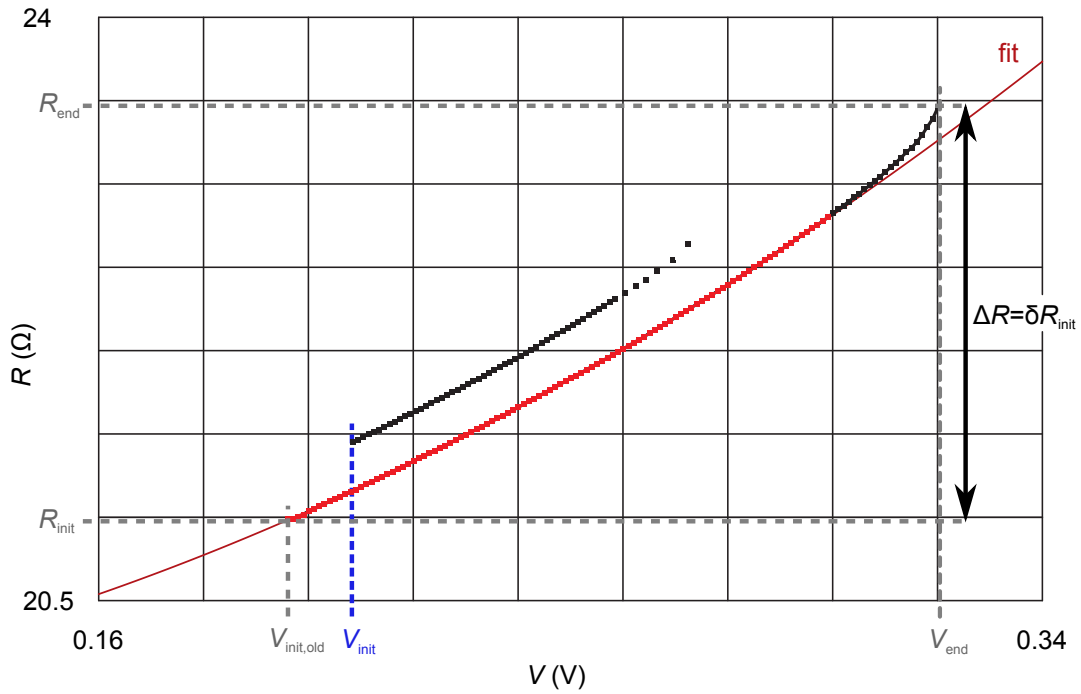

Figure 3.10 Illustration of a full voltage cycle and the initiation of the next when the criteria of the feedback control loop described in Ref. 53 are applied.

with an additional proportionality factor β which depends on details of the experimental setup such as power dissipation into the substrate. The quadratic fit (red line) in Fig. 3.10 shows that this simple model describes the data accurately in the low bias regime. The faster resistance increase at the end of the R-V trace however is irreversible and marks the onset of atom displacement and hence the beginning of electromigration.

For this work, the electromigration protocol from Ref. 53 was adapted and implemented in a C-program compatible to the existing device-control system. A *Keithley 2400* was used as a voltage source and the current was recorded with the same instrument in a four-point configuration. Initially, calculation and monitoring of the conductance instead of the resistance of the samples was chosen. Later this was changed for better comparability to results from Ref. 53.

In the course of this PhD thesis feedback-controlled electromigration was performed at room temperature under ambient conditions, in the vacuum of a SEM and at cryogenic temperatures in helium cans. For the latter purpose, a dip stick was equipped with 24 copper cables united in twisted pairs connecting a plug at the room temperature end to a fiber glass reinforced plastic board like the one shown in the photo in Fig. 3.9. For this application, 16 plug connectors where placed on the back side of the sample holder in holes drilled through the material. Electrical contact to the copper pads on the front and fixation of the plugs was established by soldering. By the same means, 16 of the dipstick cables were also connected to the respective cooper contacts. Figure 3.11 shows the front side of the thus fabricated connector with 16 plugs and

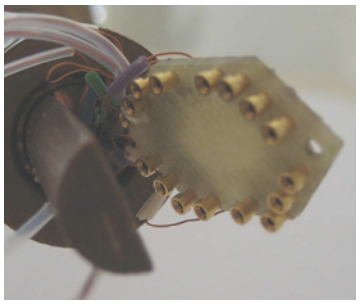

Figure 3.11 Plug at low temperature end of helium can dipstick.

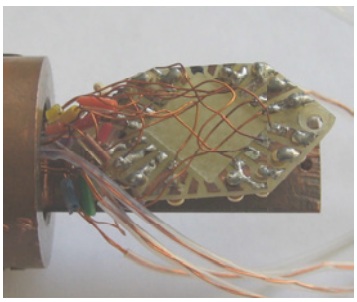

Figure 3.12 Back side of the plug soldered to 16 connectors leading to room temperature in twisted pairs.

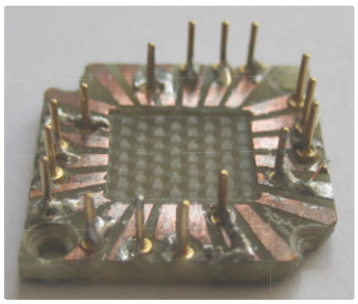

Figure 3.13 Board with 16 male connectors. Samples are glued into the notch in its center.

Fig. 3.12 its back side with the attached copper wires leading into the dip stick. The sample was then glued to a counterpart with male connectors shown in Fig. 3.13. Contacting of individual samples thus did not require soldering, only simple plugging.
We conducted measurements in liquid helium at 4.2 K as well as in cold ^{4}He gas between 5-10 K slightly above the fluid surface. Statistically relevant statements to which method should be preferred cannot be made. Working in gaseous atmosphere reliably resulted in small gap sizes and we therefore used this approach.
At room temperature electromigration on substrates covered only by native oxide instead of 400 nm thermally grown SiO_2 raised the yield of nanogaps considerably, as is discussed in more detail in Sec. 4.1.3. The thinner oxide layer however does not only reduce thermal, but also electrical insulation between the sample structure and the p-doped silicon. For the intact low-ohmic rings and wires, the parallel substrate resistance is negligible, and at low temperatures the silicon conductance freezes out. After gap generation at room temperature, on the other hand, the tunneling current between two closely spaced electrodes or the low conductance of molecules bridging them cannot be distinguished from transport through the substrate. During deposition of molecules from solution, the samples could not be cooled in the cryostat or a helium can. Yet, for immediate detection of particles incorporated in the gaps, simultaneous resistance monitoring is required, i. e. electromigration has to be performed on substrates covered by 400 nm silicon oxide. As the success of electromigration at cryogenic temperatures proved to be independent of the oxidation grade of the used substrate, as can be seen in the SEM images in Figs. 3.15 and 3.14, nanogaps for molecule deposition from solution were therefore prepared in cold helium gas. However, the reported observation of metallic clusters remaining in the gaps has to be kept in mind when using this method.

3.1.4 Synthesis and Deposition of Molecules

For reliable measurements of electronic transport through a known, specific type of molecule, working in an environment as clean as possible is crucial. The ultimate goal for our experiments would have been electromigration in the dilution refrigerator and subsequent in-situ molecule deposition by sublimation at low temperatures into the clean gaps. The completed

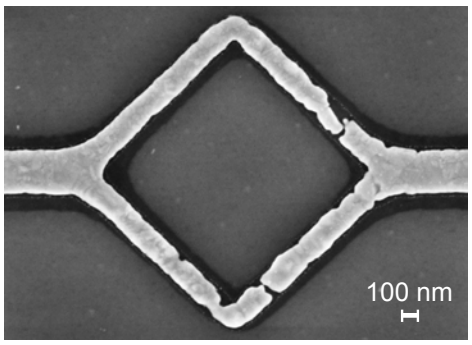

Figure 3.14 Gold ring electromigrated on a p-doped silicon substrate covered with 400 nm thermally grown oxide in cold helium gas at 8 K.

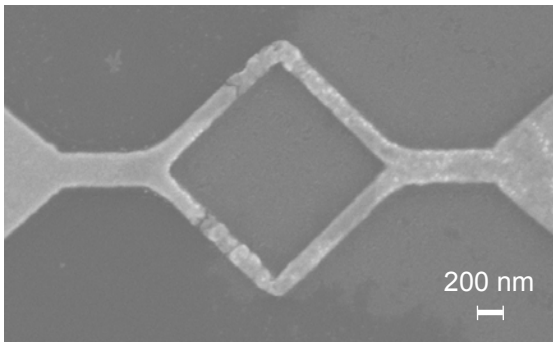

Figure 3.15 Gold ring on a p-doped silicon substrate covered with native SiO_2 after electromigration in helium gas at 8 K.

samples would not have been exposed to ambient conditions and possibly polluted by unknown kinds of molecules before measurements.
Prof. Marcel Mayor and his group at the INT, foremost Dr. Fabien Lemasson, work on the synthesis of an appropriate compound, which is long enough to bridge gaps of a few nanometers and on the other hand has a reasonably measurable conductance and is sublimable, as evaporation from solution is of course impossible in this approach. Fluorene oligomers with perfluorinated alkyl chains as side groups are promising candidates for this application. Their chemical structure is illustrated in Fig. 3.16.

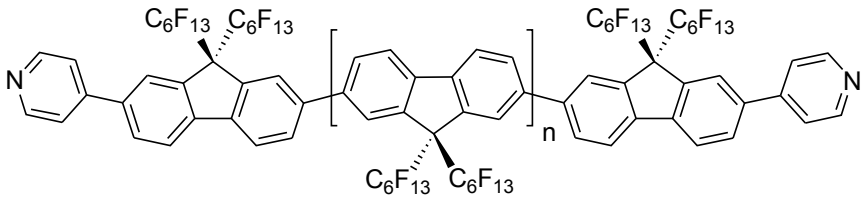

Figure 3.16 Chemical structure of fluorine-substituted fluorene oligomers.

Fluorene is characterized by a conjugated system of π-orbitals, therefore a relatively high conductivity can be expected for oligomers of this aromatic hydrocarbon. Addition of fluorine has been observed to raise the vapor pressure and to reduce sublimation enthalpy of derivatives of C_{60} [55]. Substitution of hydrogen by fluorine might have the same effect on hydrocarbons.
The molecules are not terminated by thiol groups widely used for bonding to gold electrodes, but instead by pyridine groups which have already been employed in previous single-molecule measurements with STM [24, 56] and MCBJs [57]. A better defined contact resistance than for thiol has been reported and ascribed to the π-conjugation of pyridine [26, 58–60]. Unlike in the well located sulfur-gold σ-bonds, the broader orbital overlap with the metal renders the contact conductance less sensitive to the exact atom configuration in the electrode at the contact.
Realization of the synthesis of the molecules designed specifically for this work proved a time-

consuming task and could not be finished in a reasonable time. We therefore had to resort to deposition from solution to test whether our electromigration technique yields feasible gaps in wires and especially rings for single-molecule measurements. For that purpose stiff molecular rods with a length of about 6 nm belonging to the *oligo(phenylene ethynylene)s (OPEs)* were used. Their chemical structure is shown in Fig. 3.17. Synthesis was performed by the group of Prof. Marcel Mayor at the University of Basel as described in Ref. 61 after the method introduced in Ref. 62 and reviewed in Ref. 63.

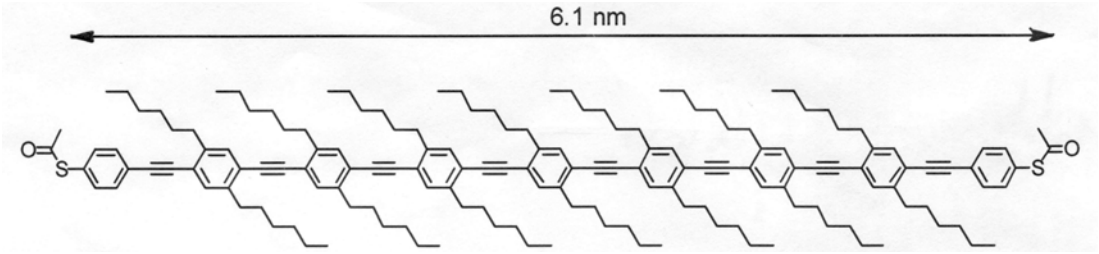

Figure 3.17 Structure of the rod molecule, an *oligo(phenylene ethynylene) (OPE)*, used for deposition from solution. Its chemical formula is $C_{158}H_{210}O_2S_2$ and its molecular weight 2205.49 g/mol.

The molecules crystallize in the form of a yellow powder. Appropriate solvents are nonpolar organic liquids like tetrahydrofuran (THF), toluene or chloroform [64]. The thiol end groups are protected as thioacetate to inhibit formation of disulfide bonds which would make the polymer insoluble. Said acetate end group is removed during the formation of the sulfur-gold bond [64, 65]. After synthesis, the OPE crystals were stored and dissolved in toluene when required. A concentration of 10^{18} molecules per liter, which corresponds to 1.7 µM/l, was estimated to have the density to produce about one monolayer. This was the dilution chosen at the beginning of all deposition experiments. In the second attempt the density was increased to 10^{20} molecules per liter to raise the probability to bridge the nanogap with one or several OPEs.

Molecule deposition was tried on in total seven rings successfully electromigrated in a helium can as described in Sec. 3.1.3. The samples were still bonded to a fiber glass board, which could be reused for in-situ four-probe connection to a *Keithley 2400*. Cross-check before molecule deposition showed no detectable conductance of the electromigrated structures on silicon substrates covered by 400 nm thermally grown oxide.

Deposition experiments were performed at room temperature under ambient pressure in argon atmosphere under steady gas flow to avoid oxidization of the molecules. Each of the ring positions on a sample was covered with a 1 µl droplet of the molecule solution. When the solvent had evaporated, the resistance of the respective structure was measured. The obtained results are described in Sec. 4.2.

3.2 Preparation of Carbon Nanotube Measurements

The preparation of the carbon nanotube samples investigated in the framework of this thesis entails three main steps, which are explained in this chapter. In the initial electron beam lithography, tungsten electrodes are prepared for the subsequent second step, the deposition of CNTs by ac-dielectrophoresis. After checking the result of tube placement in a SEM, the sample layout of selected structures is completed by the fabrication of gold contacts in another electron beam lithography step.
To optimize resolution and speed of the exposure process, two apertures are necessary. Special attention therefore has to be paid to the alignment procedures of the same with respect to the sample surface. The placing of appropriate marks in the first lithography step is described in Sec. 3.2.1 and the recovery of the SEM orientation parameters is explained in Sec. 3.2.3.
Section 3.2.2 introduces the technique of ac-dielectrophoresis and also specifies the methods of growth, dispersion and sorting of the carbon nanotubes investigated in this work. Finally, Sec. 3.2.4 describes the dilution refrigerator and the measurement setup used for low-temperature transport measurements on CNTs.

3.2.1 First Electron Beam Lithography: Deposition Electrodes

The substrates used for CNT samples consist of intrinsic silicon covered by 800 nm SiO_2 and on top 200 nm Si_3N_4 to reduce surface charges trapped by OH groups bonded to SiO. In preparation for electron beam lithography, $7 \times 8\,mm^2$ chips are cut from the wafers with a diamond cutter and subsequently spin-coated with one layer of resist. The chosen chemical is again PMMA 950 K A4. It is spread on the sample surface in 60 s at 5000 rpm, which results in a thickness of 200 nm. Afterwards the solvent is evaporated on a hot plate at 180 °C in 5 min.
Following bake-out, the electron beam exposure is performed in the same machine introduced in Sec. 3.1.2 with an acceleration voltage of 30 kV. As mentioned before, two apertures are necessary for the exposure of the CNT-deposition pattern. The finer structures are written in $100 \times 100\,\mu m^2$ writing fields with a 20 µm aperture, whilst a 120 µm one covering a $650 \times 650\,\mu m^2$ area in every stitch is used for larger objects. At the start of the electron beam lithography process, both apertures are subsequently focused on three points in the edges of the sample on dents burned into the resist. With the help of these three values, ELPHY provides automatic focus correction. Subsequently, first the smaller and then the more expanded structures are exposed successively with the respective aperture.
The details of the layout of the first lithography step are illustrated in Fig. 3.18. An overview over the entire pattern is given in Fig. 3.18 a). For orientation on the sample surface and adjustment of the two apertures in the second electron beam lithography, alignment marks of three sizes are necessary. Six large ones can be seen in the corners and at the edges of the complete layout in Fig. 3.18 a). Their shape is enlarged in Fig. 3.18 b). Three of them are actually sufficient for correction of rotation, shift and scaling parameters in the later SEM working step. The medium-sized crosses of $30 \times 30\,\mu m^2$ displayed in Fig. 3.18 d) are intended for local alignment of the 120 µm aperture. Finally, the four small marks in each $100 \times 100\,\mu m^2$ writing field shown in Fig. 3.18 e) serve for exact positioning of measurement contacts around

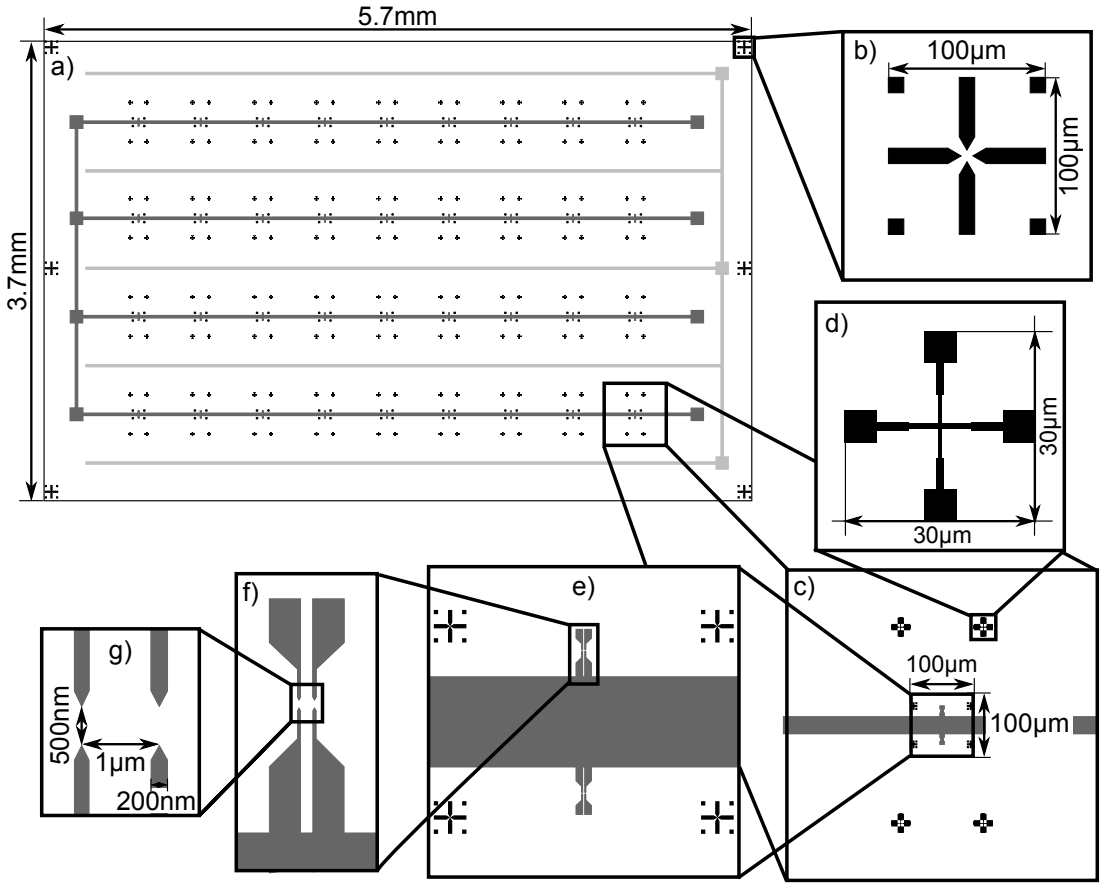

Figure 3.18 Illustration of the layout for the first EBL step. CNT-deposition electrodes placed 500 nm apart as shown in g) are created from tungsten. They are arranged in sets of four as depicted in f). Two of these sets fit into a $100 \times 100\,\mu m^2$ writing field for the 20 µm aperture displayed in e). The overview a) shows in total 72 sets connected to a common drain (dark gray) and capacitively coupled to a counter electrode (light gray). Marks of three sizes are placed for three-point adjustment (b) and aperture alignment (d, e) in the second lithography.

the deposition electrodes with the 20 µm aperture. They are again shaped as sketched in Fig. 3.18 b), though 10 times smaller.

The actual centerpiece of the layout written in the first electron beam lithography step are the electrode sets enlarged in Fig. 3.18 g). For clarity, a finished core structure incorporating two carbon nanotube conduction channels (black) in a ring is illustrated in Fig. 3.19. The tungsten electrodes are colored in gray. They are only necessary for the deposition of CNTs and not used in the transport measurements. The four gold contacts that provide for an Aharonov-Bohm-ring geometry and the two gates are shown in yellow.

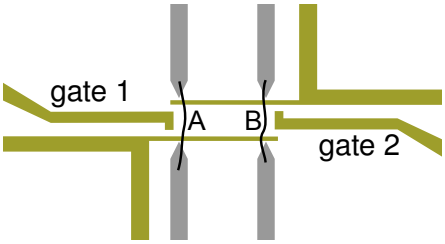

Figure 3.19 Sketch of the completed core structure of CNT samples. Two parallel tubes (black) deposited with the help of tungsten electrodes (gray) are incorporated into a ring closed with gold contacts (yellow). Each CNT is capacitively coupled to a gate.

The deposition electrodes, which are 200 nm wide and tapering into tips, are arranged in pairs spaced 500 nm apart. Always two of these pairs are aligned within a distance of 1 µm for close placement of two parallel CNTs. As can be seen in Fig. 3.18 f), one of the electrodes of each pair is always connected to a large common bus line marked in dark gray whilst the other one is left floating. It is capacitively coupled to a counter-electrode bar colored in light gray in the overview shown in Fig. 3.18 a). The role of these two common contacts in the deposition of carbon nanotubes by ac-dielectrophoresis is explained in Sec. 3.2.2.
Within every $100 \times 100\,\mu m^2$ writing field for the 20 µm aperture shown in Fig. 3.18 e), two of the deposition electrode sets from Fig. 3.18 f) are placed. In total 36 of these groups are assembled on the entire sample and thus 72 positions for possible CNT rings. This high number statistically improves the success of sample preparation and raises the yield of core structures completed as sketched in Fig. 3.19 substantially.
After electron beam exposure of the layout, development of the structures is performed in a mixture of methyl isobutyl ketone (MIBK) and isopropanol (IPA) in a volume ratio of 1:3 for 30 s. The substrate is blow-dried with nitrogen and additionally heated on a hot plate at 100 °C for 5 min to get rid of remaining solvents.
The sample is then ready for transfer into a vacuum chamber for coating with tungsten by argon sputtering. In a background pressure of 10^{-3} mbar, a plasma is ignited. Once it is stable, the sample is exposed to the tungsten vapor for 1 min. During this time interval a metal layer of about 60 nm is deposited.
Next, the substrate is placed in an acetone bath warmed on a hot plate for lift-off. Additional mechanical treatment by spraying with a pipette or syringe is sometimes necessary. After blow-drying with nitrogen, the first electron beam lithography step is finished and it is possible to proceed with CNT deposition by ac-dielectrophoresis, which is explained in the following section after specification of preparative nanotube treatment.

3.2.2 Tube Deposition by Ac-Dielectrophoresis

The CNTs used for this thesis are grown by the *pulsed laser vaporization (PLV)* technique introduced in Ref. 66 according to the procedure specified in Ref. 67 and Ref. 68 [1]. A graphite target doped with Ni and Co catalysts is vaporized in a furnace under argon atmosphere with a pulsed laser. The produced soot is then transported to a paper filter by the gas flow and collected there.
Apart from bundles of CNTs with 0.7-1.7 nm diameter spread, the raw material also contains amorphous carbon, fullerenes and metal rests. Therefore it is first ultrasonically dispersed in *dimethylformamid (DMF)*, centrifuged and decanted. This cleaning procedure is repeated three more times. Subsequently, the obtained SWNTs are re-dispersed in D_2O with a surfactant and sonicated for several hours to avoid the formation of bundles [14]. In the progress of this treatment, the tubes are separated and enveloped by surfactant molecules [69].
Still, CNTs of different length and diameter are mixed in the suspension. Selection by length is achieved by *size-exclusion chromatography*, i. e. the filtration in a glass column filled with

[1] Carbon nanotubes for this work were supplied by the group of Prof. M. Kappes at the INT.

Sephacryl S-500 gel from *Amersham Bioscience*. The SWNT suspension is pushed through the medium by compressed air. The tubes arrive at the lower end of the cylinder with a time-delay depending on their length. Thus, fractions can be collected as detailed in Ref. 70.

Sorting by diameter is even more important than by length as this parameter is linked to the chirality and thus the electronic properties of the tubes. For this purpose, *density-gradient centrifugation* is applied. This term refers to the settling of CNTs of different diameter at different depth in a aqueous solution of *iodixanol*, which forms a density gradient naturally during centrifugation. The tubes enveloped by surfactant molecules move through the medium until their density matches that of the surrounding dilution and can be extracted selectively from the fluid column [71]. By proper choice of the surfactant, selection of tubes by diameter, band gap and electronic type is possible [72].

For the sample preparation process explained in the remainder of this chapter, a solution of metallic CNTs with a length distribution of $L = 1 \pm 0.5\,\mu\text{m}$ and diameter $d = 1.2 \pm 0.2\,\text{nm}$ in D_2O with a concentration of about 10^9 CNTs/µl is used. The specific methods applied for growth, cleaning, suspension, sorting and enrichment of metallic tubes are detailed in Ref. 14. In the same text, a description of ac-dielectrophoresis according to the method published in Ref. 73 and Ref. 13 can also be found. The customary procedure is illustrated in Fig. 3.20.

First, the deposition electrode structure is completely covered with a droplet of CNTs in solution. An alternating voltage of amplitude V_{rms} and frequency f is then applied between the metallic deposition electrodes and a back gate formed by the conducting substrate. After waiting a time span t, the solution is diluted with more D_2O and then gradually substituted with

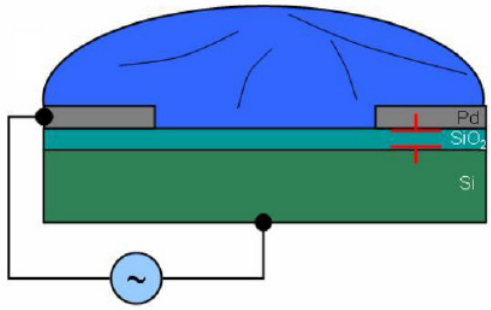

Figure 3.20 Sketch of the standard setup for CNT deposition by ac-dielectrophoresis. The metallic electrodes on the sample surface are covered by a droplet of tubes in solution. An alternating voltage is then applied between the metal and the back gate formed by the conducting substrate for several minutes. Image taken from Ref. 14.

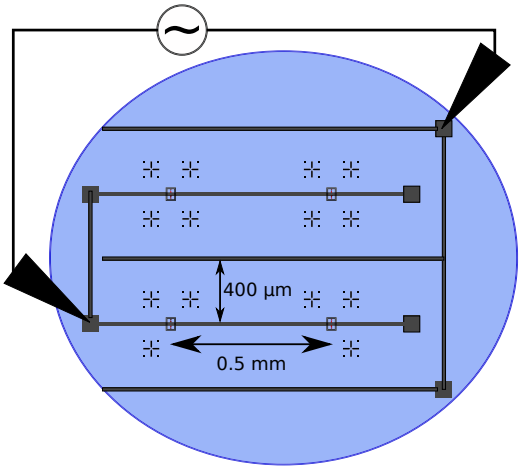

Figure 3.21 Schematic top view of one of the samples described in the previous section during ac-dielectrophoresis. For simplicity, only four of the deposition electrode sets shown in Fig. 3.18 g) are sketched. The voltage is here applied between the common bus line connecting all electrode pairs and a lithographically structured counter-electrode bar substituting the back gate.

a pipette by methanol, which is finally blow-dried with nitrogen. The organic solvent is less likely than water to tear away deposited CNTs from the electrodes again because of its lower surface tension. However, as it is very volatile, it is not suitable for a permanent dispersion of CNTs. Thus the solvent exchange is necessary.
As the substrate used for CNT samples is not conducting, back-gating is not possible. Therefore a metallic bar from tungsten is created lithographically as the layout overview in Fig. 3.18 a) shows. The ac-voltage is then applied between this counter electrode and a common bus line connecting all CNT electrode pairs for several minutes as sketched in Fig. 3.21. The deposition parameters are varied around the default values $V_{\mathrm{rms}} \approx 1\,\mathrm{V}$, $f = 50\,\mathrm{kHz}$ and $t = 5 - 10\,\mathrm{min}$ if required. The remaining procedure is the same as detailed before. Even though the capacitive coupling between the common bus line and the counter electrode is very small, this method proved to work reliably. However, further investigation into field distribution and the mechanism attracting CNTs has to be carried out.
After the deposition of carbon nanotubes, the result was checked and documented in the SEM for each of the 72 possible ring positions. An example image of successful tube placement can be seen in Fig. 3.22.
To get rid of the charges implanted by electron beam exposure during imaging, the samples are subsequently annealed in a vacuum furnace. After pumping to a background pressure around $5 \times 10^{-6}\,\mathrm{mbar}$, the temperature is ramped to $T = 600\,^{\circ}\mathrm{C}$ in 2 h. Shortly afterwards, the heating is switched off and the oven left to cool for at least 2 h before removing the substrate. The sample layout can then be finished in another lithography step, which is the subject of the next subsection.

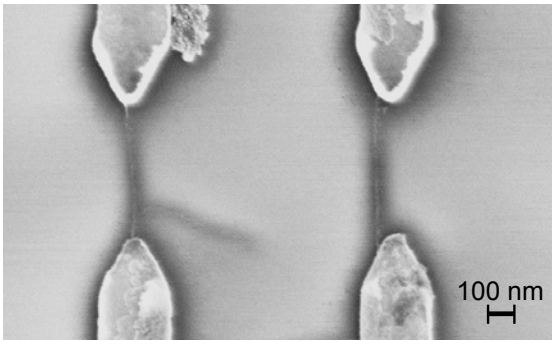

Figure 3.22 Sample after deposition of carbon nanotubes by ac-dielectrophoresis. A single tube or bundle is bridging each tungsten electrode pair.

3.2.3 Second Electron Beam Lithography: Measurement Contacts

In the final preparation step of CNT samples, gold contacts are structured by electron beam lithography. The second application of this technique is similar to the procedure described before in Sec. 3.2.1. The used resist, spin-coating and SEM parameters are identical. However, additional alignment steps are now required before exposure of the layout illustrated in Fig. 3.23.

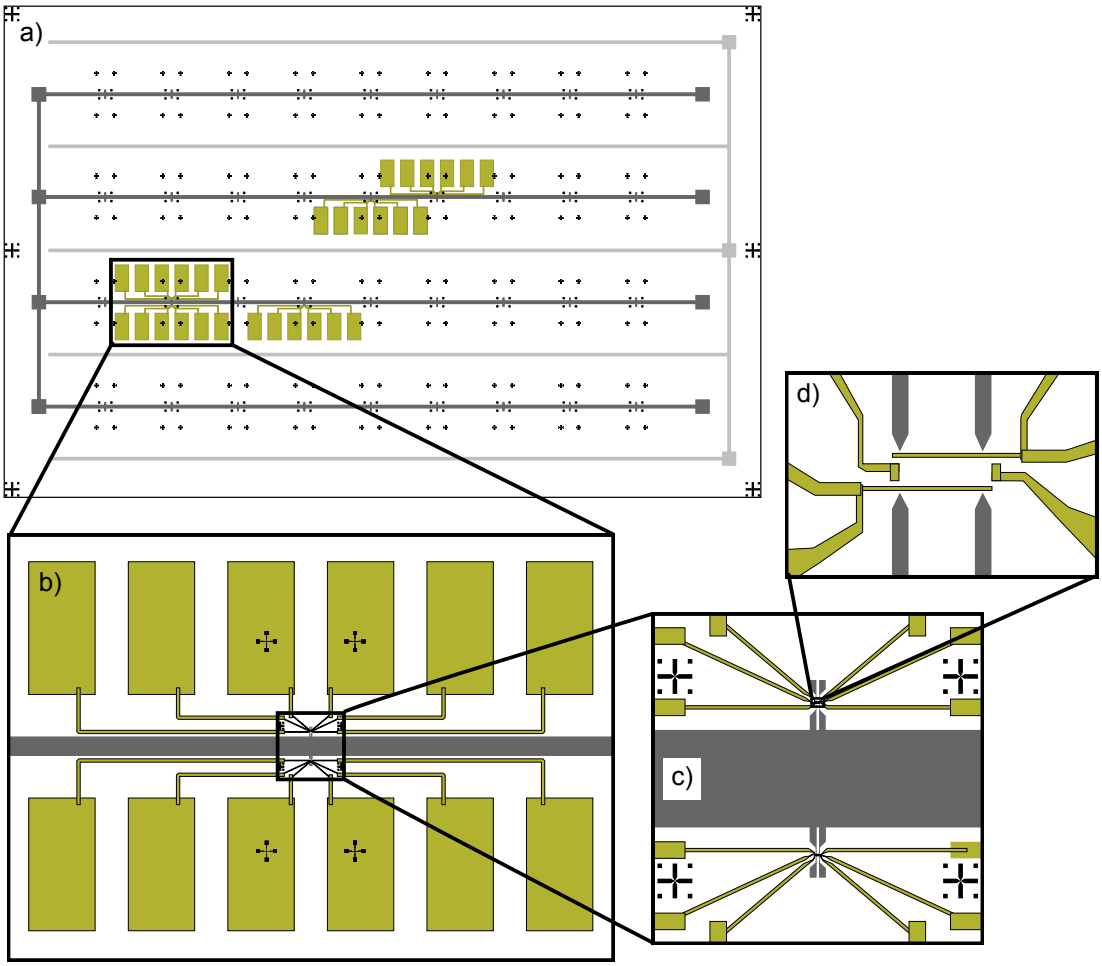

Figure 3.23 Illustration of the second electron beam lithography step. As the overview a) shows, structures selected during SEM imaging are contacted via gold bonding pads. Their layout depicted in b) is connected to the measurement contacts and gates (see c)) placed around the tungsten deposition-electrode four-sets as shown in d).

At the beginning, the layout is aligned with the sample structure in the three-point adjustment. For this purpose the central coordinates of three of the large alignment crosses placed around the layout as in the overview in Fig. 3.23 a) are determined. Scaling, rotation and shift matrices can be calculated from these values. At the same time, both apertures are focused on the three chosen points.

Those of the 72 structures with two single CNTs deposited between parallel electrode pairs as shown in Fig. 3.22 were selected during SEM imaging and are now completed by placing gold measurement contacts and gates around the tubes as depicted in Fig. 3.23 d). The horizontal bars connecting both CNTs are only 50 nm wide and spaced 400 nm apart, thus accurate positioning is required. Therefore, the 20 µm aperture is locally aligned again immediately before exposure of the respective $100 \times 100\,\mu m^2$ writing field on the small alignment marks visible

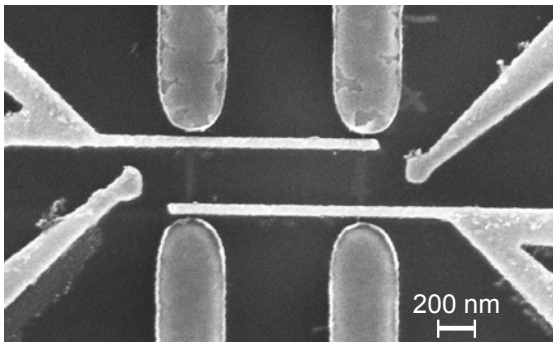

Figure 3.24 Completed ring structure incorporating two parallel CNT channels. Each side of the sample is contacted by a current and a voltage probe. Additionally the two independent gates left and right can be seen.

in Fig. 3.23 c). Large $100 \times 200\,\mu m^2$ gold pads for bonding are then connected to the finer structure as illustrated in Fig. 3.23 b) with the 120 µm aperture, which is also readjusted on the nearest medium alignment crosses.

This time-consuming repeated manual alignment before each exposure step yielded good lithography results, as can be seen in the SEM image displayed in Fig. 3.24. However, the sample shown there has not been measured. All samples investigated at low temperatures were destroyed by electrostatic discharge after removal from the dilution refrigerator and before imaging.

Following removal from the SEM, the samples are developed and baked out according to the usual recipe. Afterwards a layer of 50 nm gold is deposited by thermal electron beam evaporation as detailed in Sec. 3.1.1 in the vacuum chamber introduced in Fig. 3.2.

For the lift-off, the sample is placed in *N-ethyl-pyrrolidone (NEP)* continuously stirred with a magnet bar on a hot plate switched to 60 °C until the metal layer starts to crease. This takes 1-3 h. The removal of superfluous gold is then assisted mechanically, if necessary, by spraying with a syringe.

After blow-drying with nitrogen, the resistance of the prepared structures is tested at room temperature with two *Süss MicroTec* needle probes. As selective conditioning of the CNTs by voltage ramping as described in Ref. 74 is geometrically not possible, only those rings with a resistance of less than 10 MΩ indicating good contact to the CNTs are chosen for bonding. Before this last treatment, the samples are glued to glass fiber boards as described previously in Sec. 3.1.2. However, the gold pads are too small for the indium contacting procedure employed before and are therefore ultrasonically bonded to the board pads with aluminum wire using a commercial bonder. After this final step, the samples can be inserted into the dilution refrigerator for low-temperature transport measurements.

In total 8 samples with the final layout described in this section were fabricated. After deposition of CNTs, 15-25 electrode pairs were usually simultaneously bridged by single tubes or bundles. After completion of the second electron-beam lithography however, only 3-5 ring structures showed a reasonably low resistance (below 1 MΩ) and no leakage current to the two gates. Most of these samples were destroyed by electrical discharge during bonding or sol-

dering to the wiring of the dilution refrigerator. Only one device was finally measured in the cryostat, which is introduced in the following section along with the device setup used for the experiments.

3.2.4 Dilution Refrigerator and Electrical Setup

The low-temperature transport measurements on CNTs, which are described and analyzed in Sec. 4.3, were performed in a *Kelvinox MX250* ^{3}He/^{4}He dilution refrigerator from *Oxford Instruments*. At 100 mK it has a cooling power of 250 µW. Additionally, it is equipped with a superconducting magnet system controlled with an *IPS 120-10 Superconducting Magnet Power Supply* unit. The maximum central field at 4.2 K is 8 T.
The experimental setup is built into the cryostat in thermal contact to the mixing chamber. A RuO_2 thick-film resistor measures the temperature close to the sample position. It is calibrated down to 50 mK, but by extrapolation its $R(T)$ dependence can be approximated down to about 10 mK. During operation of the dilution refrigerator, the recorded temperature usually falls below this limit. Hence the base temperature of the cryostat used in the course of this thesis lies below this value.
In total 21 wires are fed into the cryostat. Six of them are required for four-point readout of the RuO_2 resistor and for driving current through a resistive heater placed at the sample chamber stage to allow temperature-dependent measurements. The remaining 15 cables are available for the contacting of samples. All leads are collected on a common loom. From room temperature to the 1 K-pot stage the wires consist of a beryllium-copper alloy. It has a higher resistivity and thus lower thermal conductivity than pure copper. The following loom section is made from superconducting NbTi leads, which are used to reduce Joule heating and the total serial resistance as well as the thermal conductivity. At the mixing chamber level, they are substituted by copper, which even in the milli-Kelvin range is a normal conductor and provides thermal coupling of the experiment to the mixing chamber.
Several filter stages are implemented in the cryostat wiring to reduce noise caused by electromagnetic radiation. First, Π-filters are installed at the entrance of the leads into the all-metallic cryostat shield. Second, a RC-filter board adapted for the specific application is prepared for every measurement and thermally anchored to the mixing chamber. Even closer to the experiment, right at the metallic cylinder surrounding the sample, copper powder filters are integrated into the wiring. There are described in more detail in Ref. 75.
Following sample preparation, the CNT ring samples are inserted into the dilution refrigerator and cooled to base temperature. Transport through the device is investigated by applying a bias voltage with an *Agilent 33250A Function Generator* across a 1:100 voltage divider. At the same time a voltage can be applied to each of the two gates with a *Keithley 213 Quad Voltage Source* across a 1:10 voltage divider. The current through the device is amplified with the measurement circuit shown in Fig. 3.25. An *OPA 128 operational amplifier* from *Burr-Brown* is implemented as a transimpedance amplifier with a feedback resistance of $R_{\text{feedback}} = 100\,\text{M}\Omega$ and thus a ratio of 100 MV/A=1 V/10 nA. Its output voltage is recorded with an *Agilent 3458A Multimeter*.

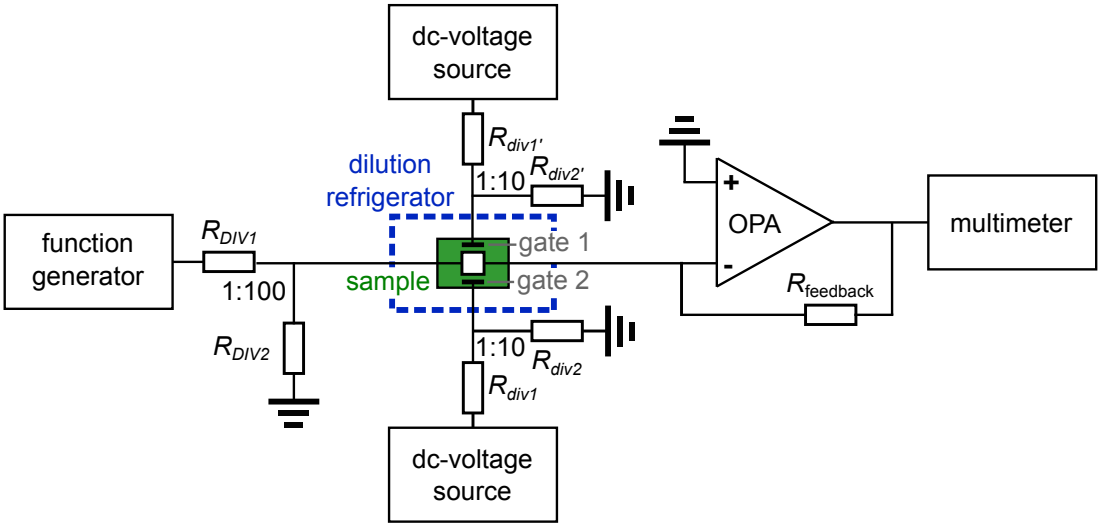

Figure 3.25 Measurement circuit for low-temperature transport investigation of CNT rings.

4 Measurements and Discussion

After the introductory part and the description of the various sample preparation methods, this chapter presents the results of measurements performed on different nanostructures. First, Sec. 4.1 reports on the electromigration of gold thin-film rings and wires. In continuation, Sec. 4.2 discusses I-V curves recorded after the deposition of macromolecules in the gaps generated in these metallic structures. Finally, the observed low-temperature transport behavior of carbon nanotubes incorporated in gold rings is shown and interpreted in Sec. 4.3.

4.1 Electromigration

This section details various observations made during electromigration experiments performed on gold rings and wires. All these metallic structures were treated with the feedback-controlled method described in Sec. 3.1.3. In the initial Sec. 4.1.1, the progress of the measured resistance increase during this process is inspected closely. Subsequently, in-situ imaging of electromigrating samples in a SEM clarifies the simultaneously occurring structural changes in Sec. 4.1.2. In conclusion, Sec. 4.1.3 deals with the influence of the thermal conductivity of the substrate on local heating of the metallic nanostructures and the resulting gap size.

4.1.1 Progress of the Electromigration Process

According to the experience gathered in the course of this PhD thesis, the electromigration process separates into three characteristic regimes. They are illustrated in the following on the basis of one of our early experiments conducted at room temperature under ambient conditions with a gold ring on a p-doped silicon substrate covered by 400 nm oxide. All data plots shown in this subsection were recorded during feedback-controlled electromigration of this sample. A SEM image of the ring taken after electromigration is shown in Fig. 4.1.

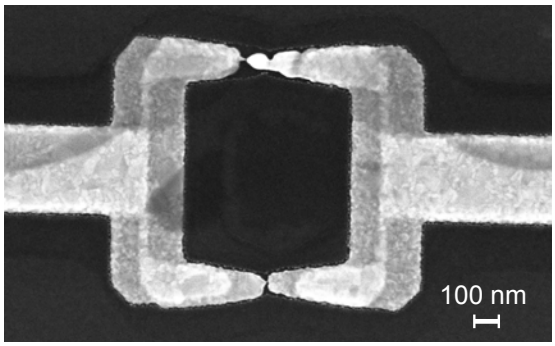

Figure 4.1 Final SEM image of the gold ring during whose electromigration the data shown in this subsection was recorded.

At the beginning of the electromigration process an increase of the sample conductance as illustrated in Fig. 4.2 is observed, which we ascribe to annealing of defects in the thermally evaporated gold structures. It was usually even more pronounced, as can be seen e. g. in Fig. 4.11.

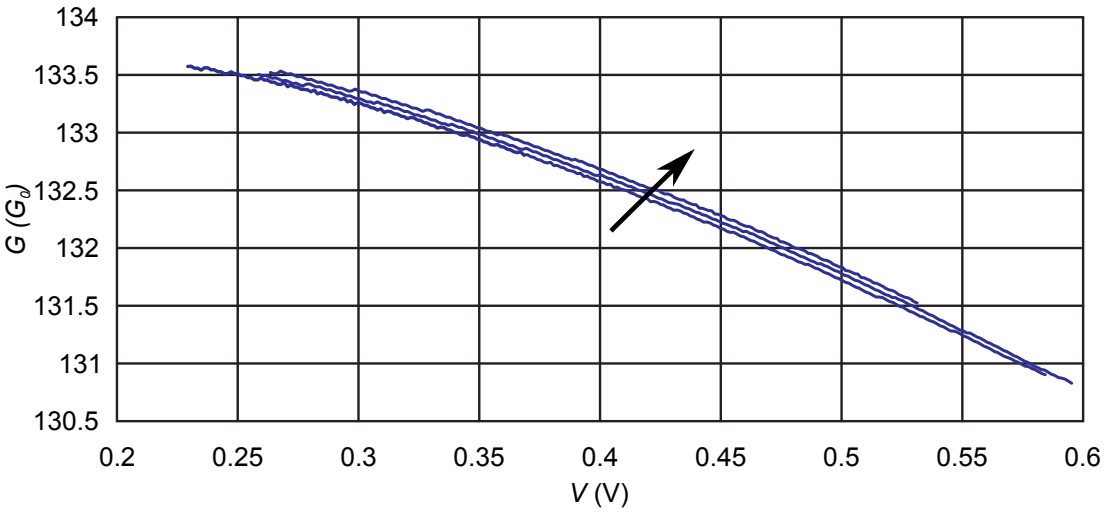

Figure 4.2 Conductance increase for subsequent cycles due to thermal annealing of the gold structure.

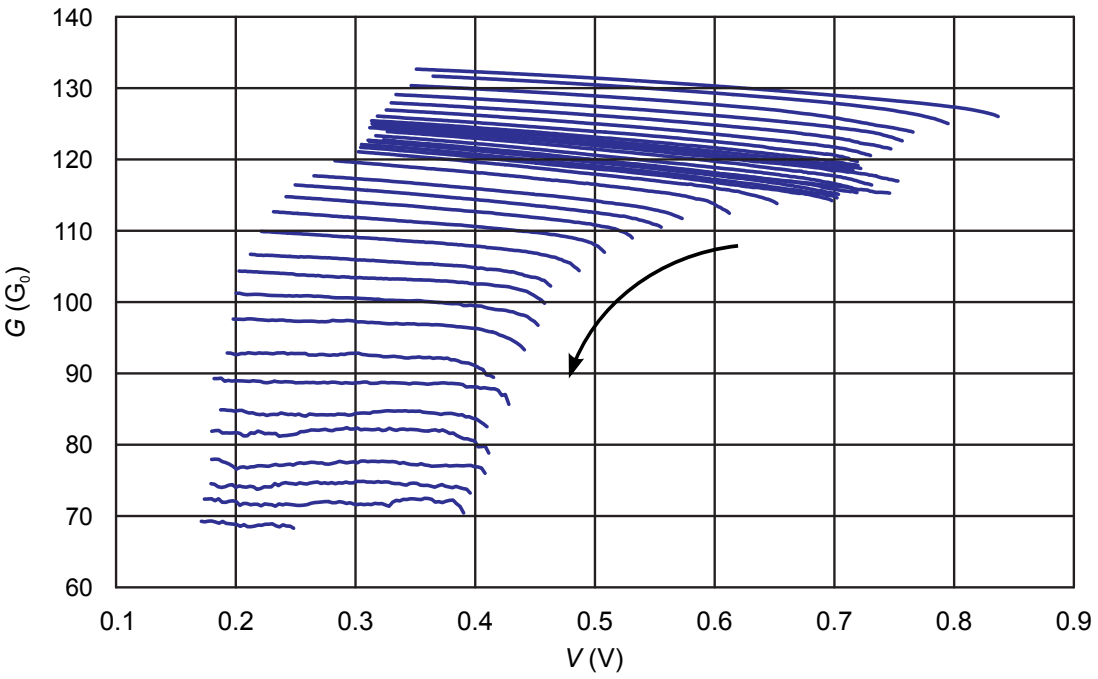

Figure 4.3 Gradual conductance decrease controlled by the feedback mechanism.

After several voltage ramps the overall conductance starts to fall gradually as shown in Fig. 4.3. G-V traces are characterized by a monotonic decrease during one voltage ramp and a clear step-like reduction compared to the previous cycle due to the faster $G(V)$ decrease toward the end of each cycle. This behavior continues down to about $80\,G_0$. In this regime, the feedback control is easiest to handle. Fitting a constant power curve to the data as in Fig. 4.4 confirms that each voltage ramp ends when a critical power is reached.

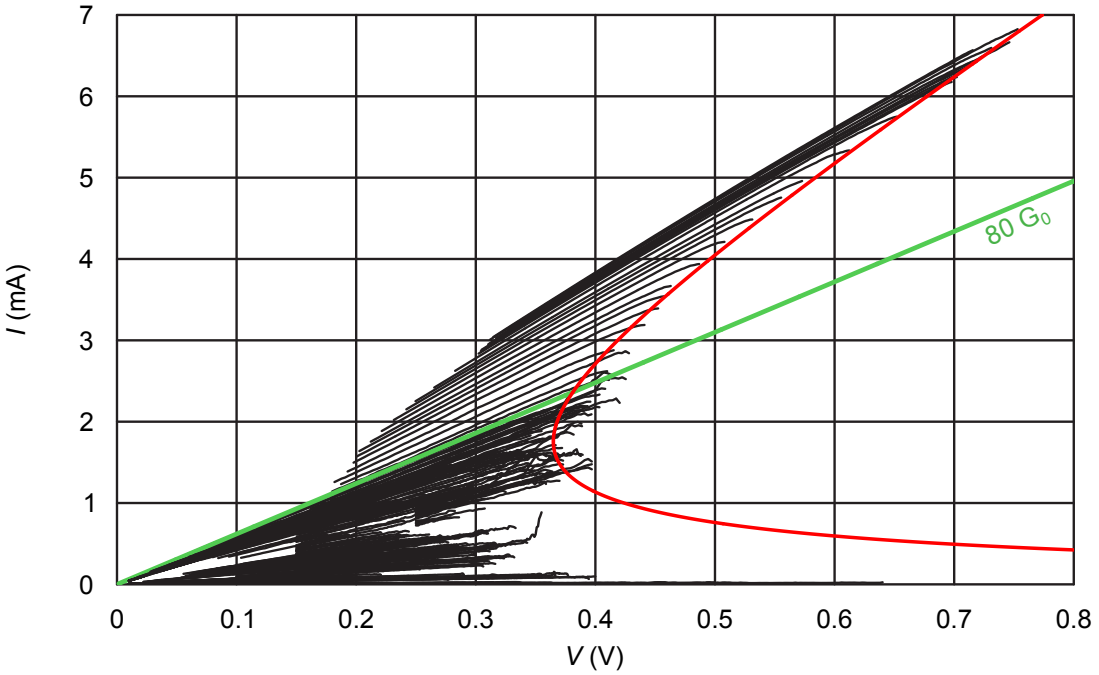

Figure 4.4 Fit of a constant power curve to an I-V plot of the data.

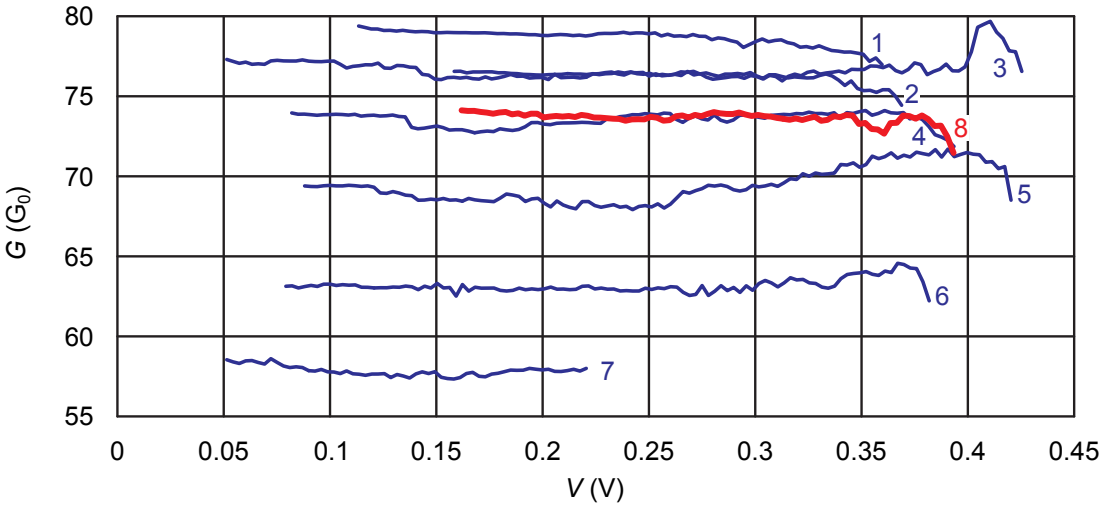

Figure 4.5 Non-monotonic and discontinuous conductance evolution below 80 G_0.

The next electromigration regime is much more difficult to control, but also much more interesting. Below about 80 G_0, the conductance evolution no longer proceeds monotonically. Instead, it often shows no clear trend or even increases towards the end of a cycle. Furthermore, jumps in the traces can be observed more frequently (compare Figs. 4.3 and 4.5). Sometimes a measurement cycle also starts at a higher conductance than the previous one ended. This is highlighted in Fig. 4.5, where the red curve is the last trace of the series.

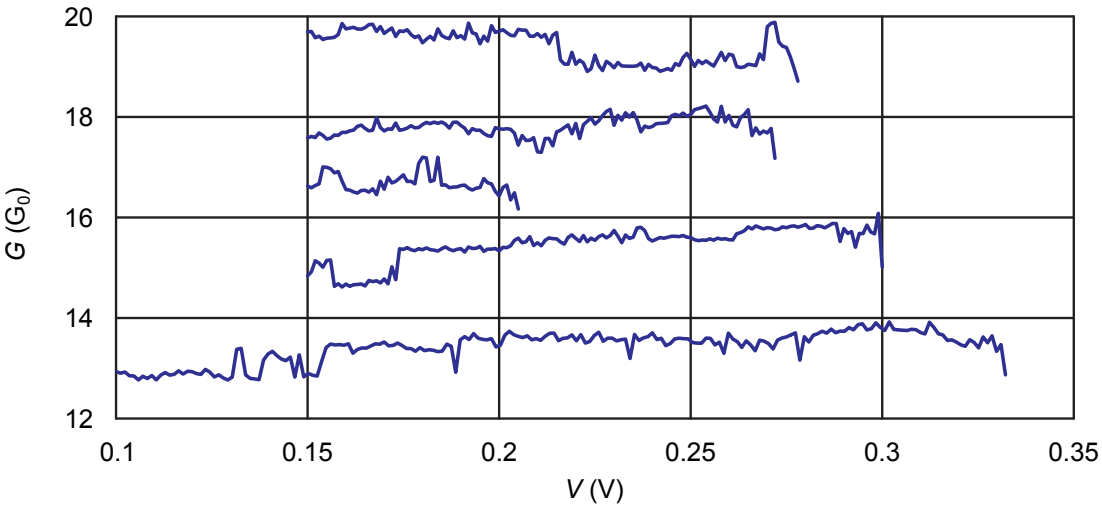

Figure 4.6 Telegraph noise in the low conductance regime.

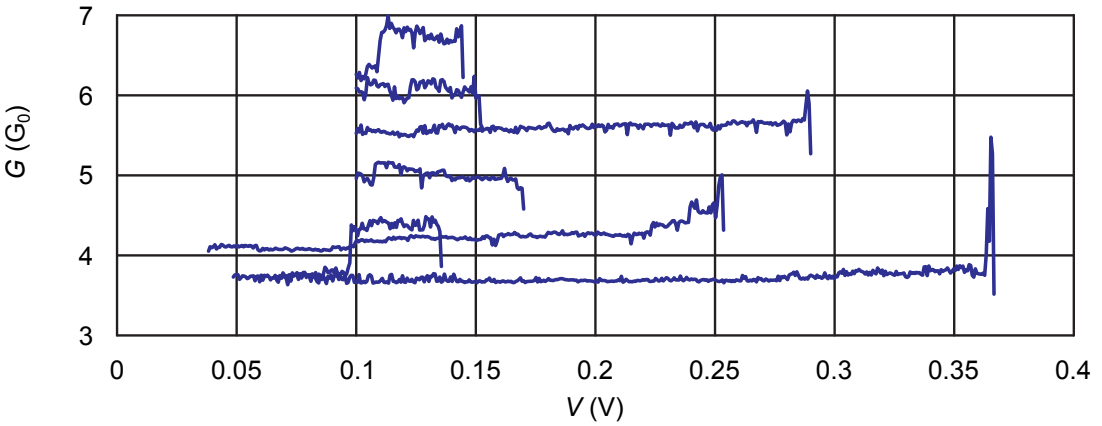

Figure 4.7 Conductance plateaus and reduced noise at few G_0.

Below about 20 G_0, discrete jumps between two conductance values can be made out, as in the first and fourth curve of Fig. 4.6. These two-level fluctuations or this *telegraph noise* is a sign of atomic and thus conduction channel rearrangement [76]. Apart from that, the conductance is now nearly independent of the applied voltage and evolves with a very small negative or sometimes positive slope. However, G-V traces do not follow discrete levels, i. e. conductance does not show obvious quantization.

Conductances of only a few G_0 were seldom reached in the electromigration experiments. More often the structures broke irreversibly in the range of 40-20 G_0. In the case that this was avoided, the G-V traces exhibited less noise below about 5 G_0 and stayed on conductance plateaus during one voltage ramp. However, these levels were not only found at well defined multiples of G_0 but at various, irregularly spaced values as illustrated in Fig. 4.7.

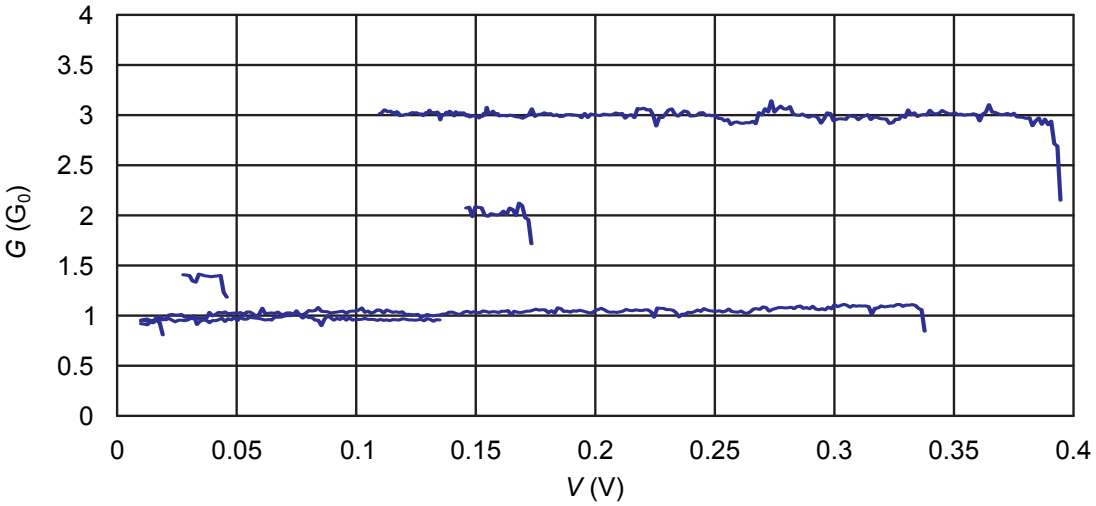

Figure 4.8 Conductance decrease in quantized steps.

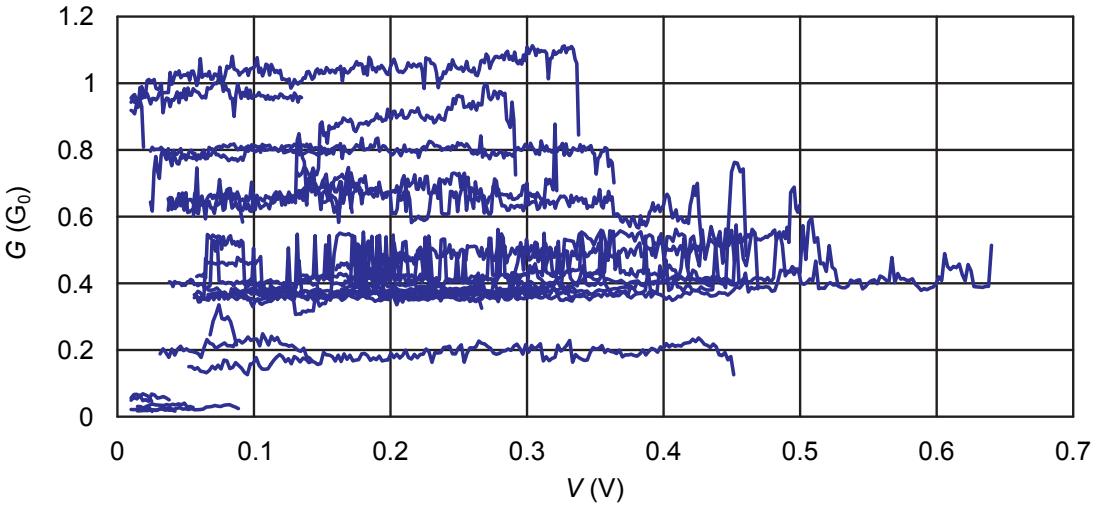

Figure 4.9 Non-vanishing conductance below G_0.

Conductance decrease in quantized steps as in the five subsequent traces in Fig. 4.8 rarely occurred. This indicates that the transmission of the conductance channels in our samples does not correspond to unity. Unfortunately, the gathered statistics are not sufficient to determine the most frequent conductance values.

The electromigration process was usually concluded by a sudden breaking of the structure and abrupt vanishing of conductance. A few times however, values below G_0 were observed as shown in Fig. 4.9. In previous investigations of I-V curves of electromigrated junctions, a high percentage was reported to show Coulomb blockade or Kondo effect, which is generally attributed to metal clusters remaining inside the gap [37–40]. In the experiments described

here, neither the current-voltage dependence nor the temperature dependence were investigated systematically. Therefore, it cannot be excluded that such metallic islands caused the residual conductance. However, the available data is not sufficient to identify the mechanism causing transport.
For electromigration in ultra-high vacuum an unusual decrease of the resistance with applied bias during voltage ramps has been reported in Ref. 77. The slope of R-V curves was repeatedly found to turn from positive to negative values after several electromigration cycles when a resistance of the order of several 100 Ω had been reached. This was also observed a few times in the course of our electromigration experiments. It mainly occurred during electromigration in cold helium gas. In view of the reports of metallic clusters remaining in gaps generated by electromigration, especially if it was performed at cryogenic temperatures, these observations have to be treated with care and investigated further. An attempt to explain this effect with tunneling junctions in parallel to the resistive contact can be found in Ref. 77.

4.1.2 In-situ Monitoring by Scanning Electron Microscopy

The electromigration of metallic wires has already been monitored in-situ before by several groups, by scanning electron microscopy (SEM) [78] as well as by transmission electron microscopy (TEM) [79, 80]. Also in the course of the PhD work described here, several gold wires, as well as rings, were electromigrated in an SEM to find out whether the process showed any obvious differences when performed with our specific setup and samples [1]. Furthermore we intended to investigate how void formation develops in the two arms of rings.
In this subsection, selected frames from the electromigration movie of a gold wire with a representative initial resistance of about 20 Ω (see Fig. 4.10) on a p-doped silicon substrate covered with native oxide are presented. The measurement was performed at room temperature in a vacuum of 10^{-5} mbar. Here, the resistance served as the control parameter for the feedback loop. Right after each voltage ramp a corresponding SEM image was taken.
In the left panel of Fig. 4.10 the still unmodified, as-prepared wire structure can be seen. The constriction at its center was designed to mark this spot for electromigration. The right end of the wire is connected to the positive side of the voltage source, i. e. electrons flow from left to right. The right panel displays the R-V trace recorded during the first feedback loop cycle. Due to Joule heating, the resistance does not increase linearly with applied voltage, but quadratically. However, no irreversible changes occur during this first cycle and the following measurement curve therefore matches perfectly.
Figure 4.11 illustrates the annealing regime observed at the beginning of the electromigration procedure. Significant material displacement can already be seen in the SEM picture. Voids form at the left edge of the wire and hillocks accumulate in the central constriction. However, the resistance traces still show an overall decrease (similar to the data in Fig. 4.2) and no increase towards the end of each voltage ramp. Annealing and electromigration take place simultaneously but the effect of the latter on the resistance is not significant.

[1] The instrument together with a sample holder electrically wired to the outside were put at our disposal by Prof. Ralph Krupke and his PhD student Christoph Marquardt.

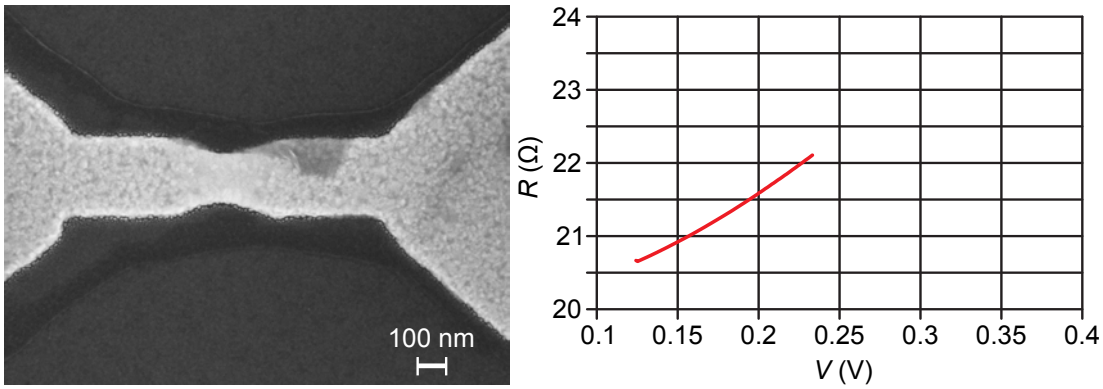

Figure 4.10 Initiation of a controlled electromigration experiment. Left panel: SEM image of a gold wire after sample preparation. Right panel: Resistance recorded during the first voltage ramp applied to the wire.

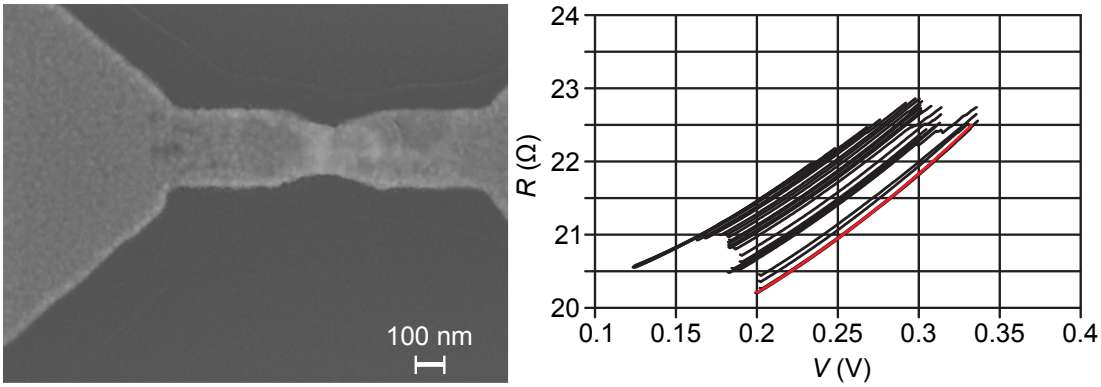

Figure 4.11 Annealing regime of the electromigration process. The SEM picture on the left was taken immediately after the R-V trace marked in red had ended. Left panel: Material transport has already taken place in the gold wire. Right panel: Successive voltage ramps applied to the wire on the left. Overall resistance is still decreasing.

In Fig. 4.12, electromigration dominates the changes in the resistance. In this second regime of smooth electromigration, the traces show a monotonic increase and a clear resistance step separates consecutive traces. A large gap has already opened up in the wire. The connection almost seems to be broken, even though the initial resistance of about 20 Ω has only about doubled up to this point.

As the process enters its third regime, which is the most difficult to control, no structural changes can be made out any more in the SEM; there is no visual difference between the images in Fig. 4.12 and Fig. 4.13. The jumps in the R-V curves indicate that the configuration of the remaining contacts bridging the gap becomes increasingly unstable.

A sudden increase of resistance to values beyond the measurement range as in the $R(V)$ plot in Fig. 4.14 usually marks rupture of the final connection across the slit that has opened in the wire. The corresponding SEM image shows, that at their smallest separation the spacing of the two resulting electrodes is below the resolution of the instrument.

It is a common observation that void formation due to electromigration often happens at the

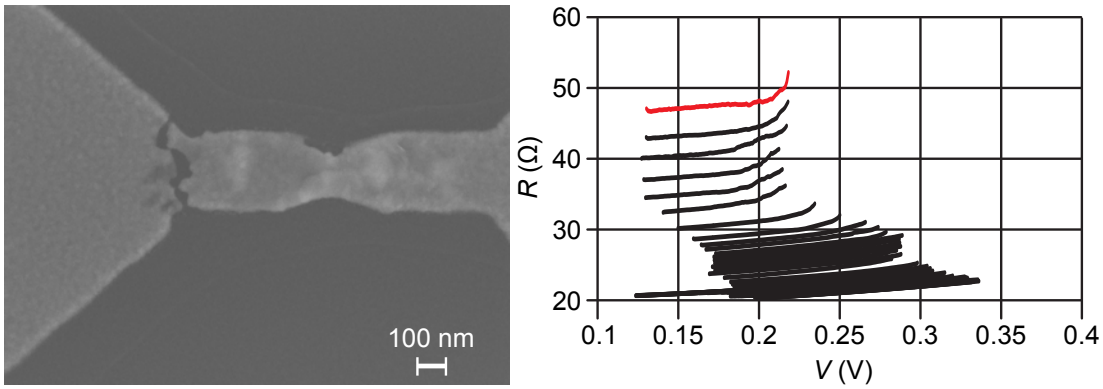

Figure 4.12 Electromigration proceeds smoothly. Left panel: Large voids have already opened up in the wire and it barely seems to be connected any more. Right panel: The measured resistance has only about doubled and is still increasing continuously.

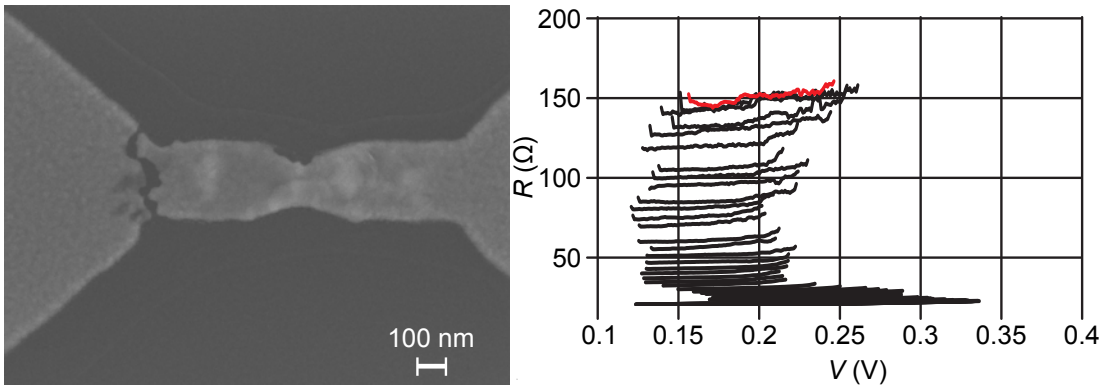

Figure 4.13 Third, unstable regime of electromigration. Left panel: No changes in configuration of the wire can be made out any more. It seems to be broken already. Right panel: The trend of R-V traces is no longer straightforward but the total resistance has not even increased by an order of magnitude.

edge of a metallic film connected to the lower source potential [33, 79]. This phenomenon is also observed here. As atom mobility depends on temperature and the wire is heated more than the leads, ions are transported away from the cathode end of the nanostructure due to the electron wind but are not replaced there. Consequently, the chance of breakage at the wire edge is raised compared to the center. Here, this trend could not be overcome by the pre-structured constriction in the middle of the wire. Apparently, the resistance in that spot was not high enough.

The movies of electromigrating structures obtained with the SEM helped to understand why electromigration becomes so difficult to control already around only 150 Ω. This corresponds to previous observations analyzed in Sec. 4.1.1 where the third regime starts below about $80\,G_0 \approx 1/(300\,\Omega)$.

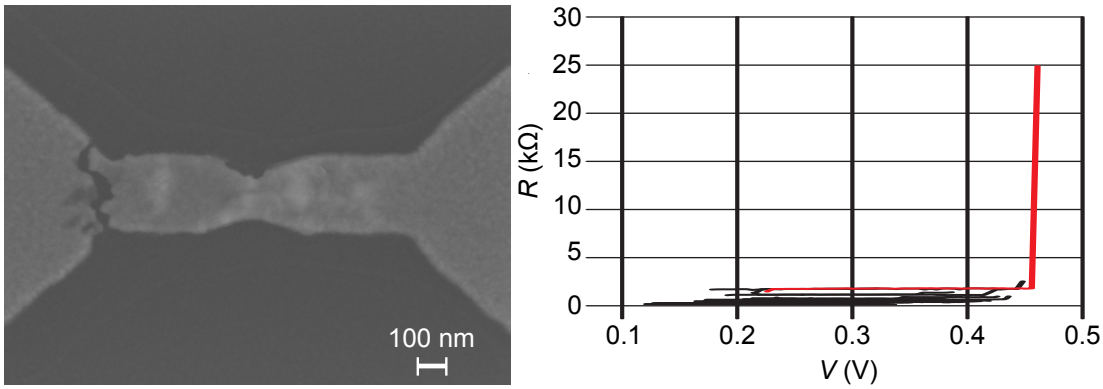

Figure 4.14 End of the controlled electromigration. Left panel: In its narrowest point, the width of the resulting gap is below the resolution of the SEM. Right panel: A sudden resistance increase indicates final rupture of contact in the structure.

4.1.3 Effect of Thermal Coupling to the Substrate

As stated before in Sec. 2.2, the progress of electromigration in a conductor is determined by two related quantities: its temperature T and the density j of the current passing through it. The metal ions become more mobile at elevated T and can then be pushed more effectively by impacting electrons. Also, the more electrons, the higher the momentum transfer. Thus, to accelerate ion displacement, temperature and current density have to be increased. At the same time, however, melting due to Joule heating has to be avoided. Otherwise control over the amount and the direction of material transport is impossible.

To attune these two competing objectives and optimize the electromigration process, external cooling is required. Heat dissipation by the environment is a possible way to achieve this, i. e. efficient coupling to a good thermal conductor is necessary. Thin films are usually placed on a supporting substrate, which can fulfill this task.

For the preparation of the first samples electromigrated in the course of this PhD thesis, thermally oxidized silicon wafers with a SiO_2 thickness of 400 nm were used. They had proved advantageous for previous work with high ohmic SET structures. The conductance of the p-doped substrates freezes out at the cryogenic temperatures where experiments are performed. However, for testing the samples at room temperature, a well insulating layer between the devices and the conducting silicon is necessary. Furthermore, this layer has to be thick enough to be resistant against scratching, ion etching or even ultrasonic bonding. 400 nm had been established as sufficient for all these purposes.

Electromigration on these substrates, on the other hand, turned out to be difficult. Even when low values were chosen for the feedback-loop parameters, i. e. the resistance change ratio δ and the power ratio p introduced in Sec. 4.1.1, the samples often broke unexpectedly at low resistance values, without previous indication in the measured data. When the result of such an experiment was checked afterwards in the SEM, the structure seemed to have been melted rather than electromigrated. An example is shown in Fig. 4.15.

When we started working with substrates of p-doped silicon covered only by a few nanometers

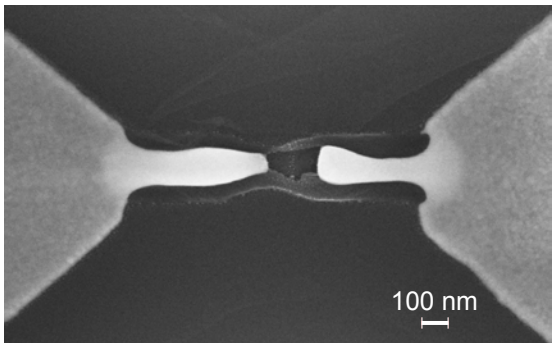

Figure 4.15 Gold wire electromigrated at room temperature on a p-doped silicon substrate covered with 400 nm thermally grown SiO_2.

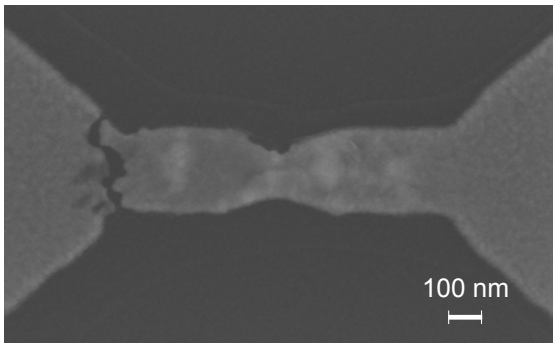

Figure 4.16 Sample after room-temperature electromigration on p-doped silicon only covered by native oxide.

of native oxide, the yield of nanogaps rose notably. The resistivity of these wafers is specified by *CrysTec* with 1-20 Ωcm. Since the intact gold wires and rings initially have a resistance of well below 100 Ω, the conductance through the substrate can be assumed to be negligible, at least at the beginning of the electromigration procedure. Once a higher resistance regime is entered, the substrate acts as a high ohmic shunt and protects the metallic structure from discharge damage during the final interruption of contact at the end of the electromigration process.

The main difference of the natively oxidized to the artificially oxidized material, however, is the better thermal coupling to the underlying doped silicon. At room temperature, the latter has a thermal conductivity in the range of $k_{\mathrm{Si}} = 150\,\mathrm{W/(K{\cdot}m)}$ [81], whereas for silicon oxide $k_{\mathrm{SiO_2}} = 1.1\,\mathrm{W/(K{\cdot}m)}$ [81] is found. Thus heat dissipation is significantly higher for the structures on native oxide, which helps to prevent excessive temperature rise and melting of the metallic sample structures. In our electromigration experiments on these substrates we found that the devices are not as sensitive to voltage changes, do not break as abruptly as before and generally at lower conductances. Furthermore, we could also visualize the impact of the improved thermal coupling to a large heat reservoir with the SEM, as the image in Fig. 4.16 demonstrates. The generated nanogap is below the resolution of the instrument, i. e. narrower than 10 nm.

To confirm these experimental results, as well as to optimize the sample structure and layout, we tried to reproduce them by numerical simulations. These take into account the contribution of two heat transport paths to dissipation: along the leads connecting the nanostructure to the outside world and across the underlying substrate. For the explanation of the successive calculational steps, a basic sample layout is initially considered here: a straight wire of rectangular cross section with two identical leads of the same form adjacent on either side, as illustrated in Fig. 4.17. The geometry is fully described by width, length and layer thickness of the nanostructure and the connections. Experimentally realistic values are $w = 200\,\mathrm{nm}$, $L = 1\,\mu\mathrm{m}$ and $d = 30\,\mathrm{nm}$ and $w' = 2\,\mu\mathrm{m}$, $L' = 40\,\mu\mathrm{m}$ and $d' = 30\,\mathrm{nm}$. We furthermore assume that all components consist of the same material, in our case gold, with a thermal conductivity of $k_{\mathrm{Au}} = 316\,\mathrm{W/(K{\cdot}m)}$ [81]. Later in this section the developed model is applied to the actual,

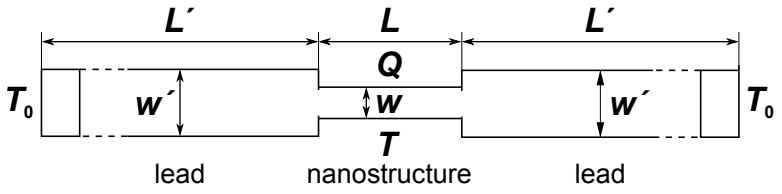

Figure 4.17 Sketch of a basic sample geometry. A wire of width w, length L and thickness d is connected to two leads with width w', length L' and thickness d'. All components consist of the same metal with thermal conductivity k_{metal}.

more complex sample structures.
A current I passing through the sample causes Joule heating. The power dissipated in the wire is $P = U \cdot I = RI^2 = R_\square \cdot LI^2/w$, where $R_\square = R \cdot w/L$ is the sheet resistance. From the dimensions and the measured resistance of several wires we determined $R_\square \approx 2\,\Omega$ for our samples at room temperature.
For appropriate description of the temperature distribution in the complex planar sample geometries used for electromigration experiments, especially the rings, consideration of one-dimensional heat transport is not sufficient. We therefore aimed for an extension of the calculations found in the literature [33] to two dimensions. The model developed for this purpose describes the temperature rise due to an electric current I in a metallic structure of thickness d, sheet resistance $R_\square$ and thermal conductivity k_{metal} on top of a substrate (e. g. Si) described by k_{subs}. Both layers are separated by a thermally nearly insulating barrier (e. g. SiO_2) of thickness b with thermal conductivity k_{barrier}. For the sake of simplicity, $R_\square$ is taken to be constant, neglecting its temperature dependence.
The heat distribution in the structure obeys the two-dimensional Poisson equation

$$k_{\mathrm{metal}} d \nabla^2 T + \dot{q} = 0 \tag{4.1}$$

where $\dot{q} = (\vec{j})^2 R_\square$ is the heat current density and $\vec{j}$ is the two-dimensional electrical current density. Equation (4.1) ignores the heat transfer to the substrate. However, the assumption that the p-doped silicon remains completely "cold" if it is only separated from the metallic structure by a very thin oxide layer is not justified. Therefore, heat transport in the silicon substrate has to be included. If we assume a temperature T_{s} at the surface of the substrate, i. e. directly beneath the barrier, this leads to a modified Poisson equation

$$k_{\mathrm{metal}} d \nabla^2 T + \dot{q} - \frac{k_{\mathrm{barrier}}}{b}(T - T_{\mathrm{s}}) = 0 \tag{4.2}$$

This equation can be solved numerically on a square sampling grid with cells of size h^2. The Laplace operator of a scalar field $u(x, y)$ is approximated by the finite difference

$$\nabla^2 u \to 1/h^2 [u(x-h, y) + u(x+h, y) + u(x, y-h) + u(x, y+h) - 4u(x, y)]. \tag{4.3}$$

Changing from spatial coordinates to an indexed notation $(x, y) \to (i, j)$ gives

$$\nabla^2 u \to 1/h^2 [u(i-1, j) + u(i+1, k) + u(i, j-1) + u(i, j+1) - 4u(i, j)] =: \frac{\mathrm{D}^2 u}{h^2}. \tag{4.4}$$

In analogy to the convenient shorthand notation D^2 for the discretized Laplace operator expressed in the brackets, an abbreviation $\vec{\mathrm{D}}$ can be used for the discretized gradient of a scalar field $u(x, y)$

$$\nabla u \to \frac{\vec{\mathrm{D}}u}{h} = \frac{1}{2h}\begin{pmatrix} u(i+1,j) - u(i-1,j) \\ u(i,j+1) - u(i,j-1) \end{pmatrix}. \tag{4.5}$$

These definitions allow to write Eq. (4.2) in the dimensionless form

$$\mathrm{D}^2 t + \left(\frac{R}{R_\square}\right)^2 p - m(t - t_\mathrm{s}) = 0 \tag{4.6}$$

where

$$t = t(i,j) = \frac{d \cdot k_\mathrm{metal}}{R_\square I^2} T(ih, jh) \tag{4.7}$$

labels the discrete temperature distribution and the parameter m

$$m = \frac{h^2 k_\mathrm{barrier}}{b \cdot d \cdot k_\mathrm{metal}} \tag{4.8}$$

is introduced.
The numerical power density p derives from the normalized potential drop V across the structure by

$$p = (\vec{\mathrm{D}}V)^2. \tag{4.9}$$

where V obeys the Laplace equation

$$\nabla^2 V \to \mathrm{D}^2 V = 0 \tag{4.10}$$

with the boundary conditions $V_\mathrm{left} = 1$ and $V_\mathrm{right} = 0$ on the left and right cross sections of the metallic structure, respectively. On all other boundaries we assume von-Neumann boundary conditions, i. e. $\nabla V \cdot \vec{n} = 0$, where $\vec{n}$ is the surface normal.
Equation (4.10) can be solved by numerical relaxation. The resulting potential map for the simple wire geometry introduced in Fig. 4.17 is shown in the color coded plot of Fig. 4.18.

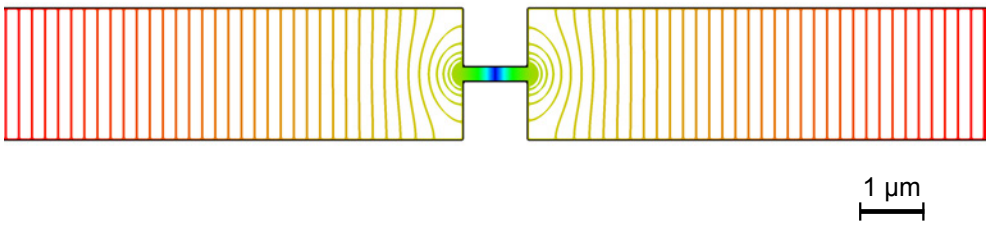

Figure 4.18 Normalized electrical potential V for an electromigrating wire found by numerical relaxation. The contour lines are spaced $\Delta V = 0.1 \cdot R_\square I$ apart and the potential drop across the wire itself corresponds to $5.5 \cdot R_\square I$.

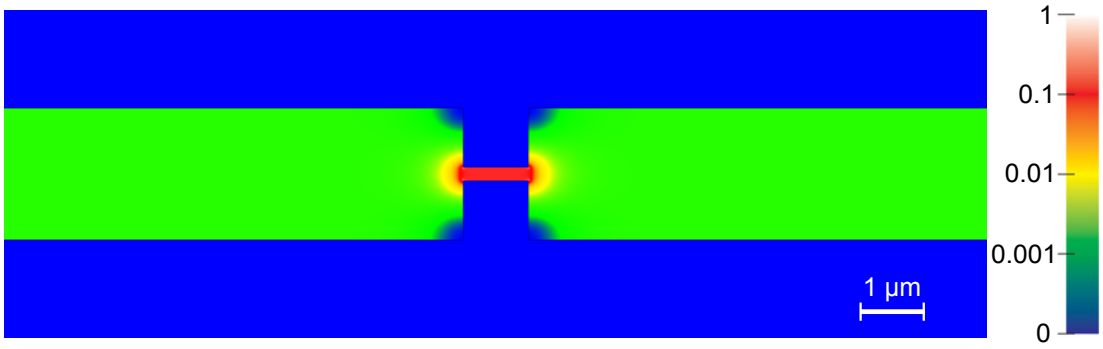

Figure 4.19 Power density map for an electromigrating wire derived from the potential V in Fig. 4.18 in units of $p_{\max}/I^2 = 212\,\mu\mathrm{W}/(\mathrm{mA}^2\mu\mathrm{m}^2)$.

After computation of the potential distribution, the current density $\vec{j}$ can be derived by

$$\vec{j} = \vec{\mathrm{D}}V\frac{U}{R_\square h}. \tag{4.11}$$

with $U = U_{\max} - U_{\min}$, the voltage applied to the structure. The total current I is then

$$I = \int\limits_{\substack{\text{cross}\\ \text{section}}} \vec{j}\mathrm{d}\vec{n} \approx \frac{U}{2R_\square h}\sum_j [V(i+1,j) - V(i-1,j)]h. \tag{4.12}$$

If the notation

$$I_{\mathrm{num}} = \frac{1}{2}\sum_j [V(i+1,j) - V(i-1,j)] \tag{4.13}$$

is introduced, it relates

$$I = \frac{U\cdot I_{\mathrm{num}}}{R_\square} = \frac{R\cdot I\cdot I_{\mathrm{num}}}{R_\square}, \tag{4.14}$$

i. e. we have $I_{\mathrm{num}} = R_\square/R$.
The result of this numerical step is illustrated again with the help of a straight wire in Fig. 4.19. Clearly, the current density rises highest in the nanostructure itself.
If we proceed by

$$\dot{q} = (\vec{j})^2 R_\square \rightarrow (\vec{\mathrm{D}}V)^2\frac{U^2}{R_\square h^2} = (\vec{\mathrm{D}}V)^2\frac{R_\square I^2}{h^2 I_{\mathrm{num}}^2}. \tag{4.15}$$

and multiply Eq. (4.2) by $h^2 I_{\mathrm{num}}^2/R_\square I^2$, we arrive at the expression in Eq. (4.6), which relates the temperature of the metallic structure and the substrate.
We assume that the wafer is heated from the top by a heat flow and stays at ambient temperature on its far side. The situation can be described by the three-dimensional Laplace equation

$$\nabla^2 T_{\mathrm{s}} = 0 \tag{4.16}$$

in conjunction with the von-Neumann boundary condition of heat flow at the substrate surface,

$$\nabla T_{\mathrm{s}}\cdot\vec{n} = (k_{\mathrm{barrier}}/b)(T - T_{\mathrm{s}}). \tag{4.17}$$

As the two Eqs. (4.2) and (4.16) for heat transport in the metallic structure and the substrate both include T and T_s, their solutions are mutually dependent. A simultaneous, self-consistent solution of their numerical equivalents t and t_s by alternating iterative relaxation is required. For this purpose, a starting distribution for the temperature of the metallic structure is first calculated by numerical relaxation of Eq. (4.6), assuming an unelevated substrate temperature t_s and making use of the previously determined power-density map. The point spread function describing the heat distribution around a single point source on the surface of a half space is once computed by a *DFFT (discrete fast Fourier transform)* method.
Subsequently, the resulting heat flow $m(t-t_s)$ is convoluted with this precomputed point spread function. This yields updated values for the substrate temperature t_s, which are then used again for another relaxation step of Eq. (4.6). The procedure converges on an ordinary PC work station for grid sizes of 3000 × 1000 pixel in less than an hour. The obtained values can be compared to the experimental parameters via

$$T(ih, jh) = \frac{R_\square I^2}{d \cdot k_{\text{metal}}} \cdot t(i, j). \tag{4.18}$$

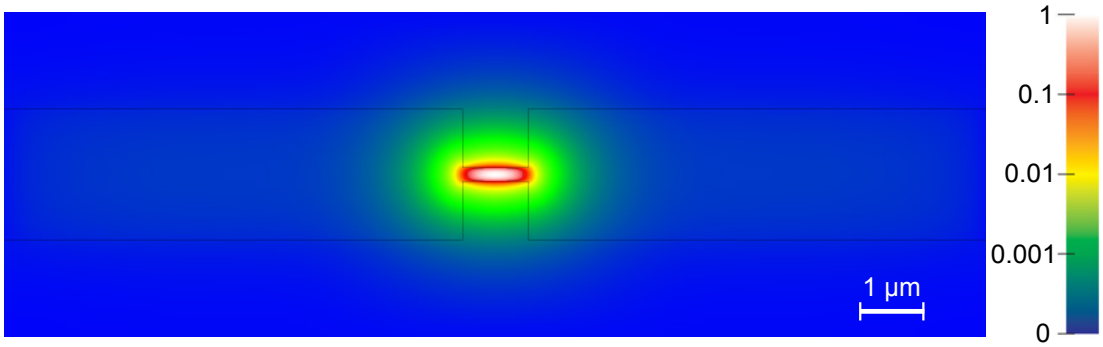

Figure 4.20 Excess temperature distribution in the substrate directly beneath an electromigrating gold wire with $d = 30\,\text{nm}$. The metallic structure is separated from the Si substrate by only a thin SiO_2 layer of 1 nm. The temperature is plotted in units of $R_\square I^2/(d \cdot k_{\text{metal}}) = 67 \cdot I^2\ \text{mK/(mA)}^2$ for the parameters mentioned in the text.

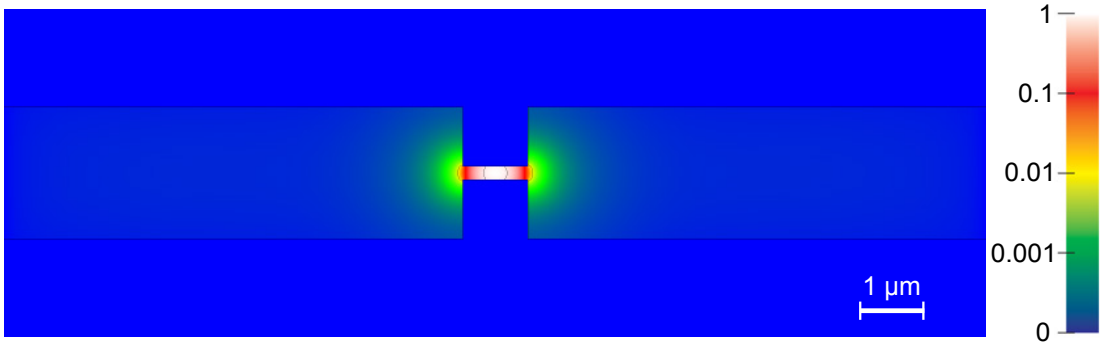

Figure 4.21 Excess temperature map for an electromigrating wire in good thermal contact to a heat reservoir in units of $R_\square I^2/(d \cdot k_{\text{metal}}) = 0.11 \cdot I^2\ \text{K/(mA)}^2$. The metallic structure is separated from the substrate by only a thin SiO_2 layer of 1 nm.

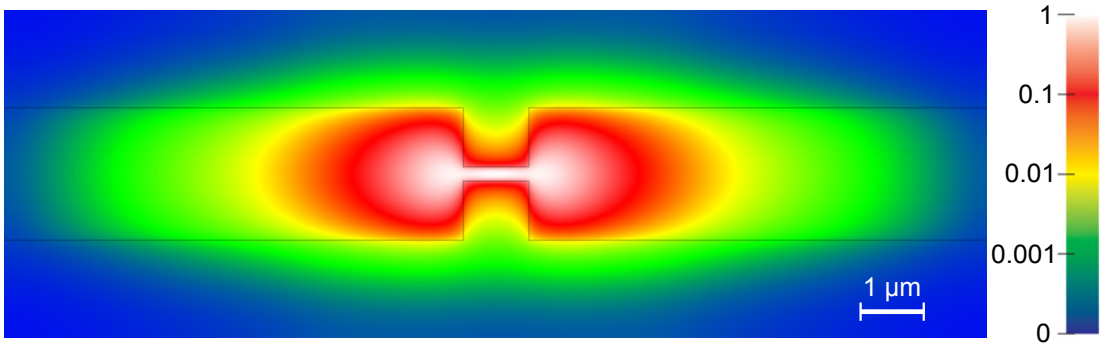

Figure 4.22 Excess temperature map of the substrate directly beneath an electromigrating wire in units of $R_\square I^2/(d \cdot k_{\mathrm{metal}}) = 11 \cdot I^2\,\mathrm{mK/(mA)^2}$. A 400 nm thick SiO_2 layer covers the silicon wafer.

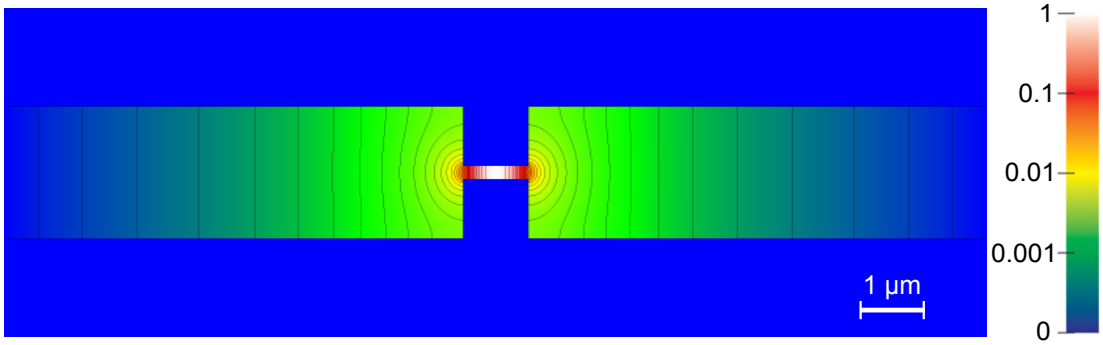

Figure 4.23 Excess temperature map for an electromigrating wire thermally weakly coupled to a heat reservoir in units of $R_\square I^2/(d \cdot k_{\mathrm{metal}}) = 1.7 \cdot I^2\,\mathrm{K/(mA)^2}$. A 400 nm thick SiO_2 layer inhibits heat loss to the substrate.

Figure 4.21 shows the numerically obtained temperature map for a 30 nm thick gold wire on a silicon substrate. Heat flow between the two layers is only inhibited by a thin native oxide layer of $b = 1$ nm in this case. Clearly, heating is mainly restricted to the nanowire. The leads and also the substrate, whose temperature is plotted in Fig. 4.20, are only warmed up in a small region around it. For comparison, the heating of a metallic wire of identical shape on a substantially thicker thermally generated oxide layer of $b = 400$ nm is illustrated in Fig. 4.22. It extends over a much larger area.

We now apply the two-dimensional heat transport description developed above to the wire geometry we most commonly used. It is illustrated in Fig. 4.24. The nanostructure is constricted at its center and contacted via four leads. The potential computed for this layout by numerical relaxation is color-coded into the same image. It serves as a starting point for the calculations. Figure 4.25 shows the power density derived from this potential according to Eq. (4.11). Finally, the temperature distribution mapped in Fig. 4.26 represents the situation on native oxide, whilst in Fig. 4.27 the more extensive heating of the structure on 400 nm oxide again manifests itself.

For a comparison not only of the extent of the heated area but also of the values and slopes of the temperature distribution, cuts along the central wire axis are plotted in Fig. 4.28 for

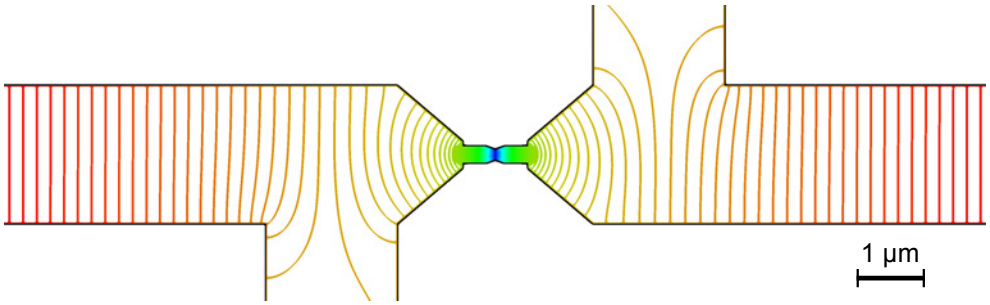

Figure 4.24 Potential calculated for the layout of a constricted wire in a four probe configuration. The distance of the contour lines corresponds to $\Delta V = 0.1 \cdot R_\square I$ and the potential drop across the thin central wire is $5.5 \cdot R_\square I$.

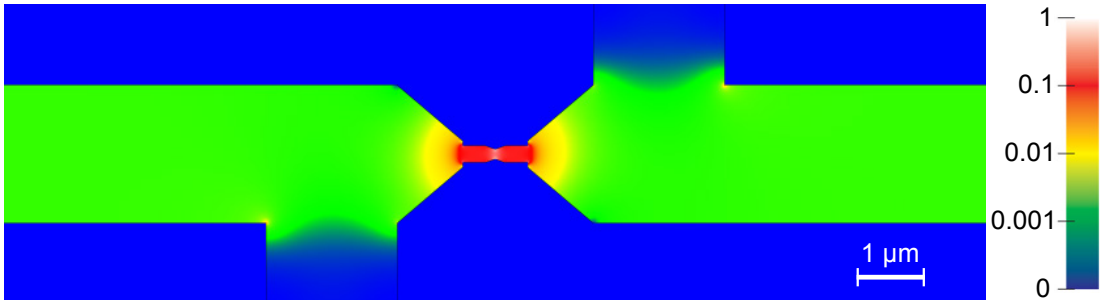

Figure 4.25 Power density derived from the potential in Fig. 4.24 in units of $p_{\max}/I^2 = 159\,\mu\mathrm{W}/(\mathrm{mA}^2\mu\mathrm{m}^2)$.

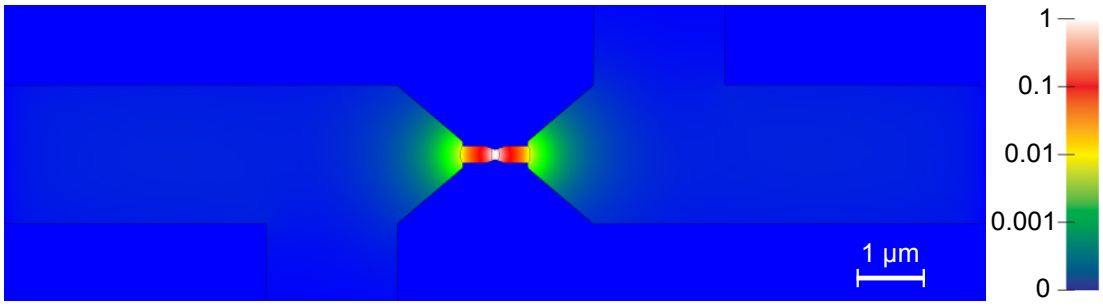

Figure 4.26 Temperature map of a constricted wire in units of $0.11 \cdot I^2\,\mathrm{K}/(\mathrm{mA})^2$. The gold structure is only separated from the p-doped silicon substrate by a native SiO_2-barrier of thickness $b = 1$ nm.

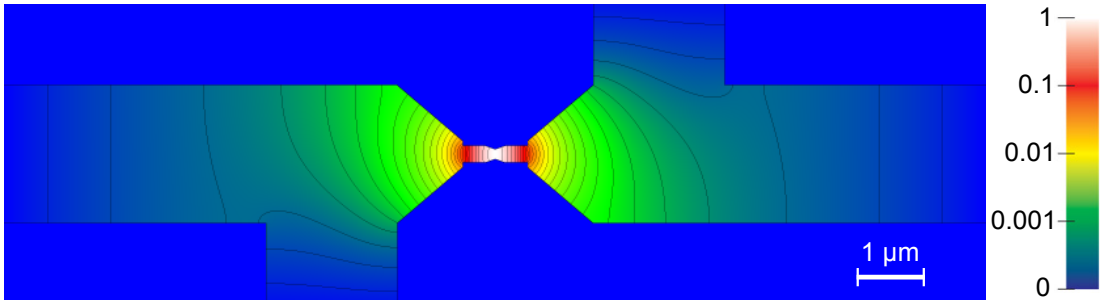

Figure 4.27 Temperature map of a constricted wire in units of $1.5 \cdot I^2\,\mathrm{K}/(\mathrm{mA})^2$. The gold structure is separated from the p-doped silicon substrate by a thermally insulating SiO_2-barrier with $b = 400$ nm.

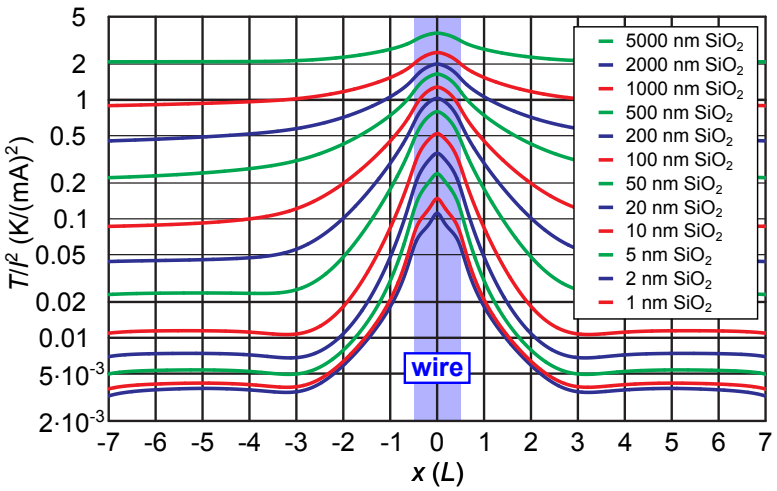

Figure 4.28 Comparison of the temperature rise along the central axis of the layout shown in Fig. 4.24 parallel to the wire for different SiO_2 barrier thicknesses b calculated with the approach described in the text. The extent of the wire itself is marked in blue.

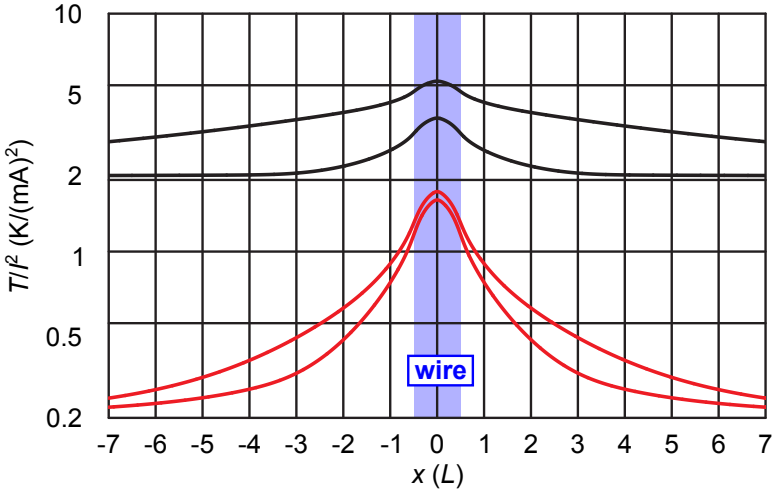

Figure 4.29 Illustration of the cooling effect of the two voltage probes for wires with the shape shown in Fig. 4.17 on 500 nm and 5 µm SiO_2. The temperature reduction is more pronounced for the thicker insulating layer.

different b. The respective calculations conducted for barrier thicknesses from 1 nm to 5000 nm in a 1-2-5 series confirm that from the thermal point of view a thin oxide layer is preferable for electromigration experiments.

Furthermore, calculations performed with the two-dimensional model also demonstrate the cooling effect of the two additional voltage probes. They cause a significant reduction in temperature at the contact positions as illustrated in Fig. 4.29. Note, however, that the efficiency of this cooling effect depends on available space for connecting wide leads. This space is more efficiently used in the current path, where it would reduce the power density quadratically in

the lateral dimensions.
At the conclusion of this section, the developed heat transport model shall finally be applied for its original aim: to determine the points in a ring structure that carry the highest current and are heated most by Joule heating. The ring structure we initially prepared for electromigration is sketched in Fig. 4.30. As this plot shows, the current density is elevated not only in the center of the ring arms, but also at the T-junctions of the square ring and the leads. This makes them a possible starting point for electromigration, which competes with the prestructured constrictions. To avoid the excess current density at the edges to the leads, we shaped the transition region more smoothly by tilting the square ring as Fig. 4.31 shows. If we look at the lead-ring junction again, the current density is not raised there any more, only at the constrictions centered in the ring arms. The temperature profile of both ring shapes, on the other hand, appears very similar, as illustrated by the comparison of the numerical results plotted in Fig. 4.32 and Fig. 4.33.

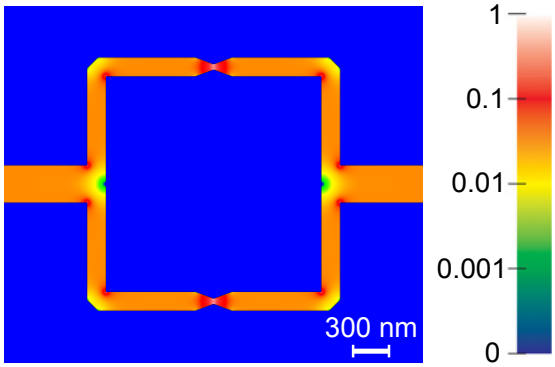

Figure 4.30 Power density in the square ring structure initially used for electromigration derived with a two-dimensional model in units of $p_{\max}/I^2 = 442\,\mu\mathrm{W}/(\mathrm{mA}^2\mu\mathrm{m}^2)$.

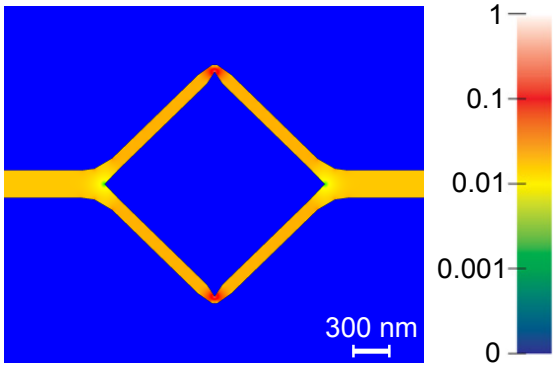

Figure 4.31 Power density of a tilted square calculated in a two-dimensional approach in units of $p_{\max}/I^2 = 1414\,\mu\mathrm{W}/(\mathrm{mA}^2\mu\mathrm{m}^2)$. The ring-lead junctions are smoothed to avoid current density rise in these spots.

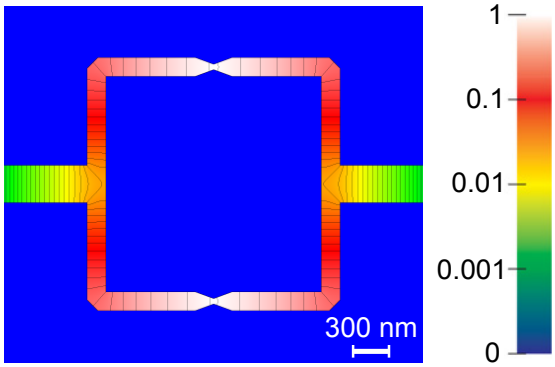

Figure 4.32 Temperature distribution in a square ring structure on top of a thermally insulating barrier of t =400 nm SiO_2 in units of $5.2 \cdot I^2$ K/(mA)^2.

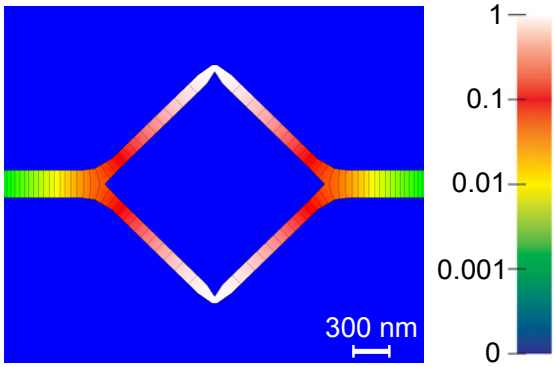

Figure 4.33 Temperature distribution in a tilted ring structure on top of a thermally insulating barrier of t =400 nm SiO_2 in units of $8.6 \cdot I^2$ K/(mA)^2.

In summary, according to the simulations described here, the tilted ring layout leads to an increase of both the decisive quantities for onset of electromigration, namely current density and temperature, in the upper and lower ring edge. No other spots are likely starting points for electromigration because of an excessive current density rise and indeed a shift of slits generated by electromigration away from the ring-lead junction towards the center of the ring arms was observed. However, gaps still did not reliably form at the edges pre-structured for that purpose. It seems that other high-resistive spots like grain boundaries and further defects still prevailed in the electromigration experiments and displaced the nanogaps. Thus, the design can still be fine-tuned concerning the ratio of arm width and constriction in future experiments to optimize the location of generated junctions.

4.2 Transport through Macromolecules

During application of the molecule-toluene solution as described in Sec. 3.1.4, the respective ring structure was connected in a four probe configuration to a *Keithley 2400* source and measure unit. Cross-check before molecule deposition showed no detectable conductance of the electromigrated structures on silicon substrates covered by 400 nm thermally grown oxide.
After each ring position had in turn been wet with solution and the solvent had dried, a voltage was ramped across the respective structure and the current was measured. This was tried on in total seven successfully electromigrated rings. In one case a non-vanishing resistance could be recorded after a second deposition attempt with a molecule concentration of 10^{20} per liter. Two consecutively measured I-V traces are plotted in Fig. 4.34. The blue curve was obtained during an upward bias ramp from -3 to $+3$ V, the red one in the following downward sweep.

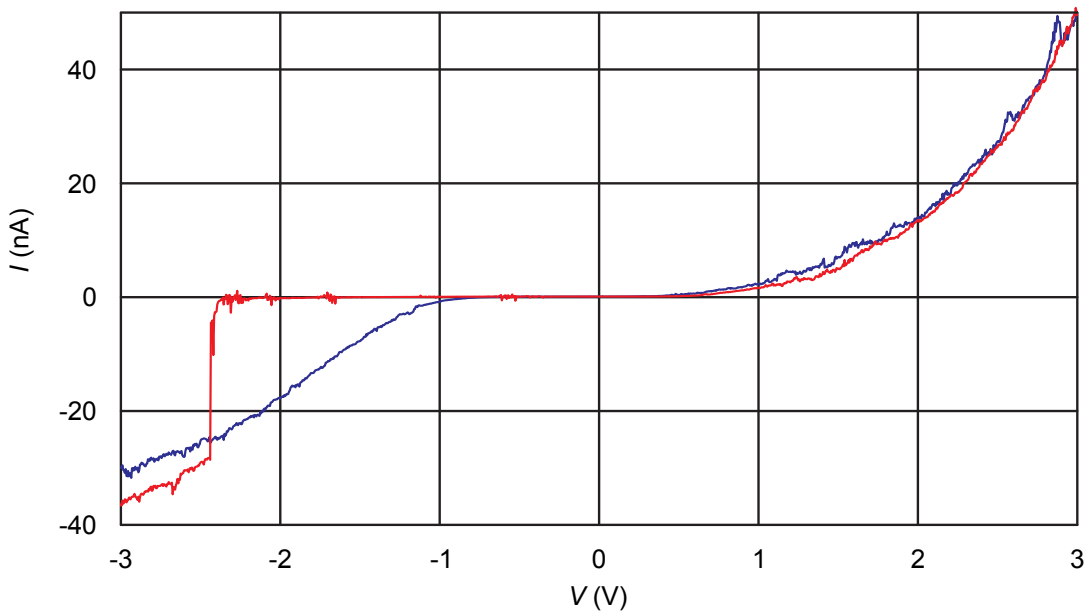

Figure 4.34 I-V curves of an electromigrated gold ring measured at room temperature after deposition of OPEs from solution. The trace obtained during an upward (downward) voltage ramp is marked in blue (red).

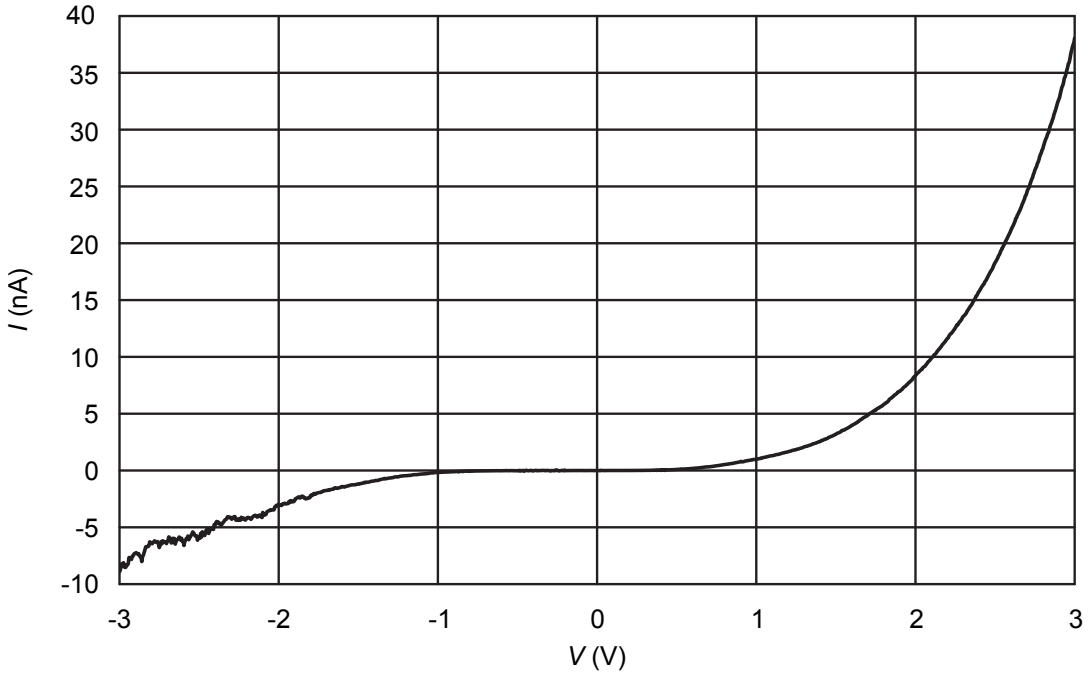

Figure 4.35 Averages over all I-V curves obtained for an applied bias of ±3 V.

All measurements presented here were conducted at room temperature on a single device. Unfortunately, the sample substrate broke when it was removed from the glass fiber board for transfer to the dilution refrigerator. Therefore no temperature dependent data is available. Furthermore, the gate influence has not been investigated either. This complicates the identification of the transport mechanism responsible for the observed I-V curves. Nevertheless, a discussion of the measurements within these limits is given in the following.
Initially, discrete jumps between different conductance states occurred repeatedly, especially in the negative bias regime. One example can be seen in Fig. 4.34 (red curve). After several voltage ramps however, the I-V curves gradually smoothed and settled on a trace of lower conductance. The average over all these traces is displayed in Fig. 4.35.
In the low voltage regime, the current increases linearly with a very small slope. This can be formulated as [82]

$$I = G_{\mathrm{eq}} \cdot V \tag{4.19}$$

where G_{eq} is called the equilibrium conductance. From fitting to the averaged data in a range of ±0.1 V, a value of $G_{\mathrm{eq}} = 24\,\mathrm{pS}$ was extracted.
Both G_{eq} and the overall conductance of the junction are lower compared to values reported elsewhere for similar OPE derivatives [14, 83], though no data is available for the specific compound used here. Together with the fluctuations observed in the I-V dependence, this indicates that possibly at least one of the molecule-gold bonds was not fully formed.
For higher voltages, conductance rises clearly nonlinearly and asymmetrically. Possible transport mechanisms include thermionic emission, hopping conduction, direct tunneling and

Fowler-Nordheim tunneling. As the first two are thermally activated processes, making statements about their contribution to transport in the measurements shown here is difficult. On the other hand, neither of the tunneling processes shows any changes with temperature. Furthermore, during both direct and Fowler-Nordheim tunneling, the phase memory of the transported charge carriers is preserved [51], which is an important prerequisite for a possible occurrence of interference.

The tunneling regimes can be summed up in the framework of the Simmons model [84–86]. It describes the tunnel effect between metallic electrodes separated by a thin insulating film of (effective) width s constituting a potential barrier $\varphi(x)$ of arbitrary shape with the mean height $\overline{\varphi}$. Due to its simplicity, it is the most widely-used theory for the extraction of physical parameters from presumably single-molecule data [51, 87–89]. However, results for molecule parameters obtained from fitting this model are seldom robust [82]. Furthermore, it is difficult to reproduce asymmetric shape of I-V curves with this approach. It is thus not sufficient for neither a quantitative evaluation nor qualitative interpretation of the experimental data presented here.

Yet, asymmetry of transport through a metal-molecule-metal junction can be interpreted qualitatively following the approach described in Sec. 2.4 for the modeling of current through a quantum dot. Again only two states of the system are considered, namely empty and filled molecular level, 0 and 1. However, no gate electrode is taken into account here, i. e. $V_\mathrm{G} = C_\mathrm{G} = 0$. Coupling to the electrodes is described by the capacities C_1 and C_2 together with the tunneling coupling coefficients $\tilde{g}_1$ and $\tilde{g}_2$ as illustrated in Fig. 4.36. Only thermal broadening of the density of energy states in the leads is taken into account, which at the elevated temperature $T \approx 300\,\mathrm{K}$ and for only moderate applied bias V is sufficient.

The molecule possesses a self-capacitance C_Σ, which is dominated by the two junction capacities C_1 and C_2 for the case considered here, $C_\Sigma = C_1 + C_2 + C_\mathrm{stray}$. Thus the offset charge en_0 induced on the island by an applied voltage V is given by

$$en_0 = C_1 V_1 + C_2 V_2 \tag{4.20}$$

where V_i, $i \in \{1, 2\}$, is the voltage drop across contact i. Otherwise the theory detailed in Sec.

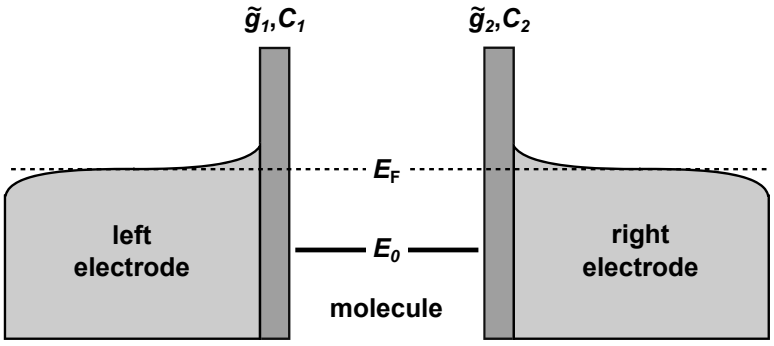

Figure 4.36 Molecule with a single energy level coupled to two metallic electrodes via tunneling barriers described by the tunneling coupling constants $\tilde{g}_1$ and $\tilde{g}_2$ and the capacities C_1 and C_2.

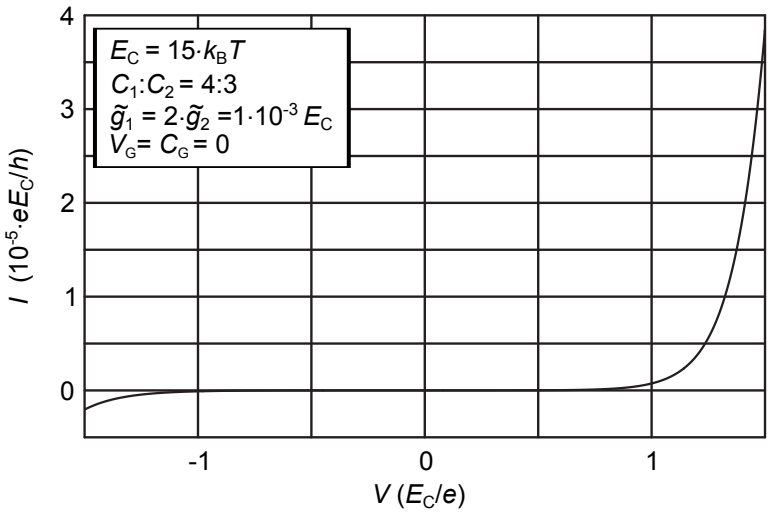

Figure 4.37 Numerically calculated I-V response of a quantum dot coupled to metallic electrodes via tunneling barriers with the tunneling coupling constants $\tilde{g}_1 = 1 \cdot 10^{-3} E_C$ and $\tilde{g}_2 = 5 \cdot 10^{-4} E_C$ and the capacitance ratio $C_1 : C_2 = 4 : 3$ at $T = 1/15 \cdot E_C$.

2.4 can be applied identically and the current through the device can be calculated according to Eq. (2.29).

Figure 4.37 shows an I-V curve calculated with this simple numerical model of a quantum dot connected to two Fermi reservoirs. It can reproduce the asymmetric Coulomb blockade and the asymmetric current slope. Both features are caused by an unequal ratio of the capacitances C_1 and C_2. For the current suppression to be observable at a given temperature, the charging energy has to exceed the thermal energy, $E_{ch} > k_B T$. At room temperature, $T \approx 310\,\mathrm{K}$, where the experiments where performed, a total capacitance of the molecule C_Σ of less than the order of 1 aF, i. e. weak capacitive coupling to the two electrodes and low self-capacitance, are required to fulfill this condition. For the plot in Fig. 4.37, a capacitance ratio of $C_1 : C_2 = 4 : 3$ was chosen.

The energy offset of the molecular LUMO with respect to the Fermi energy can be shifted with a gate electrode, which was unfortunately not implemented. As the offset is not known in the experiment, the gate voltage and capacitance were set to zero, $V_G = C_G = 0$. The complete simulation parameters can be found in the inset of Fig. 4.37.

Even if the asymmetry of the measured I-V curve can be explained within the framework of the simple model described here, the exact current slope can, however, not be matched. Overall, it appears to be steeper than in the graph in Fig. 4.35. On the one hand this can be attributed to the current fluctuations observed in the experiment which also lead to deviations in the averaged data. On the other hand the slope mismatch reflects the deficiencies of the SQTM. Cotunneling and intrinsic level broadening are not considered. The latter issue is studied in more detail in Sec. 4.3.3.

In summary, it can neither be confirmed nor excluded with certainty that the experimentally observed conductance is the response of an OPE deposited in the electromigrated gap. The

shape of the measured I-V curves qualitatively corresponds to common molecule transport signatures which are usually evaluated with a simplification of the Simmons model. However, it was unfortunately not possible to extract quantitative results for comparison with previously reported experimental results due to a lack of knowledge about the junction parameters. Furthermore, the asymmetry of the recorded I-V traces is unexpected as the molecule in itself is symmetric. A dissimilar junction capacitance is a possible explanation as illustrated with the calculation presented in the last part of this section. Possibly one gold-molecule bond was not fully formed, as is also indicated by the pronounced current fluctuations in the negative bias regime. Last, the gradual change in conductance over time might be due to conformational changes of the conjugated OPE system triggered by voltage application, or it might be caused by a changing number of molecules contributing to transport. For a conclusive interpretation and evaluation of the I-V curves presented here, further experimental data is required.

4.3 Low Temperature Transport Measurements on Carbon Nanotubes

This section treats the investigation of low-temperature transport through a gold ring incorporating two carbon nanotube channels. The structure layout was already shown in Fig. 3.19. All measurements described in the following were performed below 10 mK on a single sample. The used dilution refrigerator as well as the device setup and circuitry are described in Sec. 3.2.4. In the first Sec. 4.3.1 here, the effect of a voltage applied to a single gate on the sample conductance whilst the second gate is kept grounded is visualized and noteworthy features of the results are pointed out. In Sec. 4.3.2 then, I-V curves recorded while both gates were addressed at the same time are presented and described. A detailed analysis and discussion of the observed transport characteristics based on numerical simulations explained in Sec. 4.3.3 are given in Sec. 4.3.4.

4.3.1 Coulomb Diamond Measurements

The first experiments described here were aimed at the verification of the functionality of both gates. For that purpose, I-V curves of the sample were measured by ramping a bias across the CNT ring whilst at the same time the offset voltage applied to one of the gates was stepped from V_{min} to V_{max} in intervals of ΔV. The other gate remained grounded. The resulting I-V traces are presented in color plots in Fig. 4.38 for the first gate with $V_{\mathrm{g1,min}} = -1\,\mathrm{V}$, $V_{\mathrm{g1,max}} = 1\,\mathrm{V}$ and $\Delta V_{\mathrm{g1}} = 6\,\mathrm{mV}$, and for the other gate in Fig. 4.39 with $V_{\mathrm{g2,min}} = -500\,\mathrm{mV}$, $V_{\mathrm{g2,max}} = 500\,\mathrm{mV}$ and $\Delta V_{\mathrm{g2}} = 4\,\mathrm{mV}$.
In accordance with the theory for transport through quantum dots explained in Sec. 2.4, Coulomb diamonds can be observed in both plots. However, their appearance differs from the numerically calculated blockade pattern displayed in Fig. 2.14, as well as from the observed low-temperature-conductance behavior of CNTs shown in Fig. 2.10, in quite a few unexpected points. The first difference is that the onset of conductance is not sharp. Furthermore, size, shape and sequence of the diamonds are not regular. No traces of excited states are

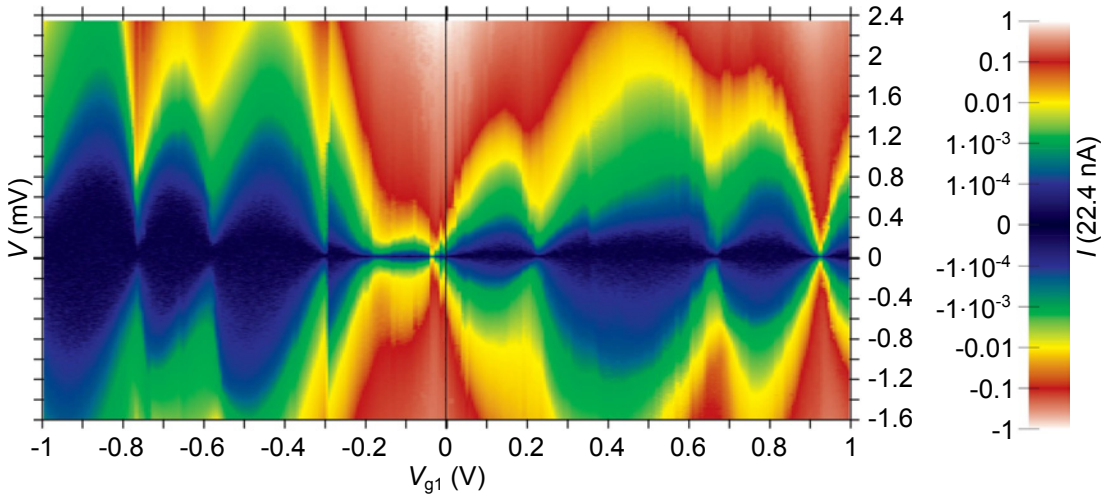

Figure 4.38 Coulomb diamonds measured by recording I-V traces and stepping the offset voltage applied to one gate from $V_{\mathrm{g1,min}} = -1\,\mathrm{V}$ to $V_{\mathrm{g1,max}} = 1\,\mathrm{V}$ in $\Delta V_{\mathrm{g1}} = 6\,\mathrm{mV}$ intervals while the other gate was grounded. The axes show the bias and gate voltage, respectively. The measured current is color-coded according to the logarithmic scale on the right.

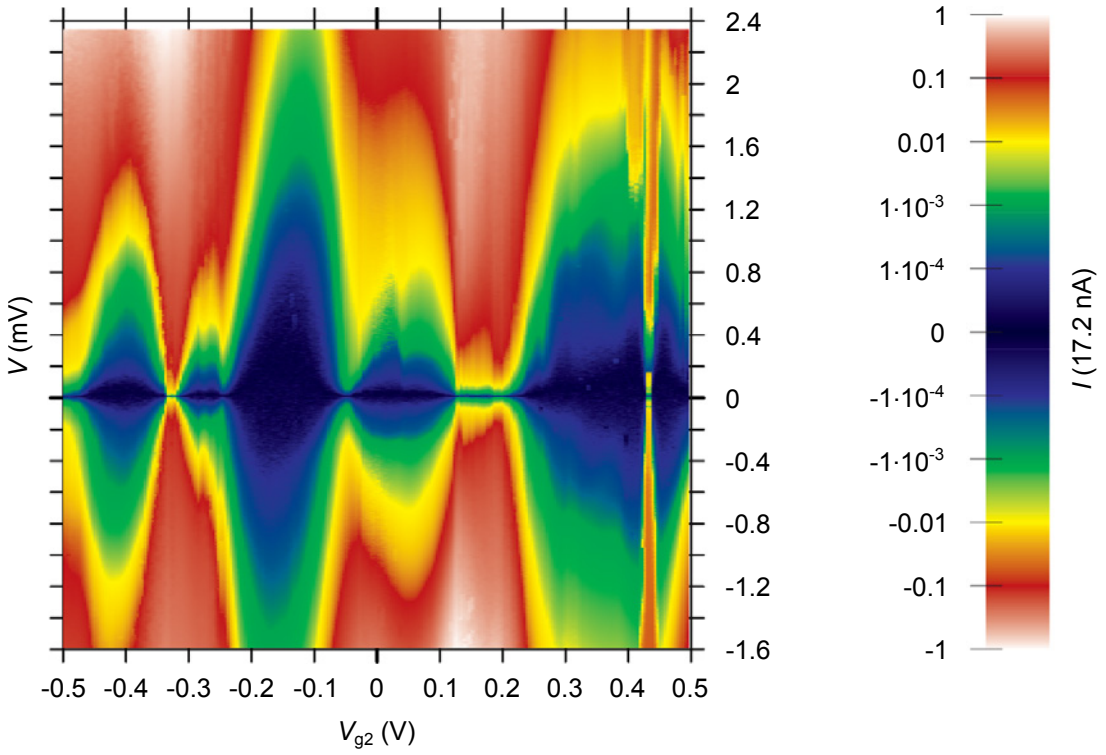

Figure 4.39 Coulomb diamonds measured and plotted identically to Fig. 4.38 but with interchanged gates. The applied voltage is stepped from $V_{\mathrm{g2,min}} = -500\,\mathrm{mV}$ to $V_{\mathrm{g2,max}} = 500\,\mathrm{mV}$ in $\Delta V_{\mathrm{g2}} = 4\,\mathrm{mV}$ intervals.

detectable either and in certain continuous voltage intervals, e. g. between $V_{g2} \approx 110 - 220\,\mathrm{mV}$ in Fig. 4.39, Coulomb blockade appears to be suppressed. Before analyzing this data in detail, however, further results obtained by simultaneously addressing both gates are presented.

4.3.2 Simultaneous Gating Measurements

The setup for simultaneous gating measurements was the same as the one used in the preceding experiments. However, instead of grounding one gate whilst addressing only the second, now the voltages applied to both were stepped. Throughout the entire measurement, the bias voltage was kept at a low value $V = 75\,\mu\mathrm{V}$ in the linear response regime. A current value was then recorded for every parameter pair V_{g1} and V_{g2}. The result of this measurement is presented in Fig. 4.40 and analyzed in the following.

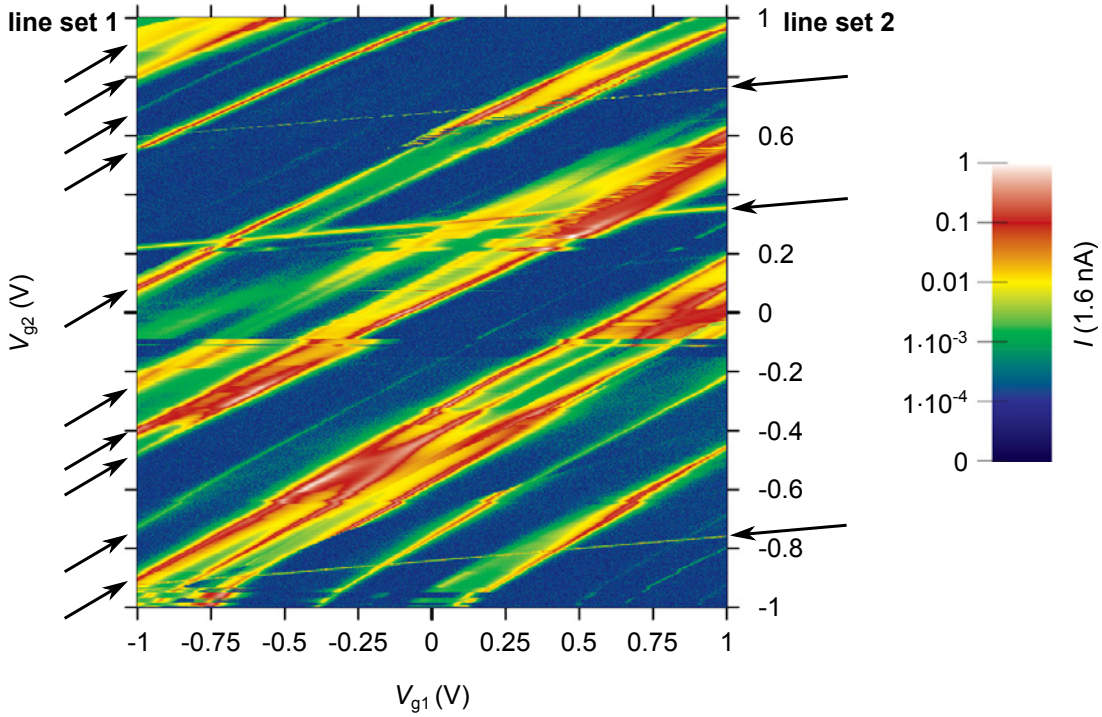

Figure 4.40 Current recorded for a fixed bias voltage $V = 75\,\mu\mathrm{V}$ and simultaneously stepped gate voltages V_{g1} and V_{g2}. It is plotted with a logarithmic color scale shown on the right.

Figure 4.41 illustrates the capacitive coupling between two CNTs A and B and two side gates g1 and g2. The measurement contacts are not included in the sketch. For a symmetric sample geometry with equal capacity of each gate with respect to the nearest CNT, $C_{Ag1} = C_{Bg2}$, and no coupling to the opposite CNT, $C_{Ag2} = C_{Bg1} = 0$, a square pattern of conductance peak lines as illustrated schematically in Fig. 4.42 is expected. The pattern in Fig. 4.40 does indeed show two sets of approximately parallel lines which can be attributed to two different CNT transport channels. They are marked by arrows. However, these sets are both inclined with respect to the

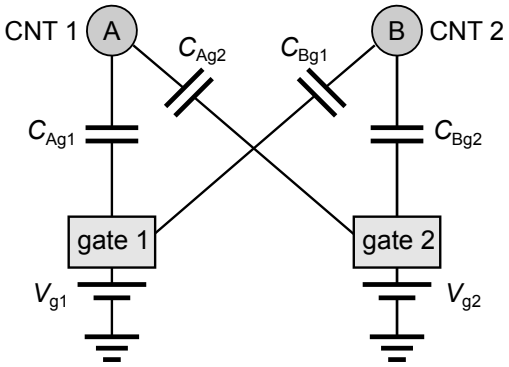

Figure 4.41 Illustration of the capacitive coupling between two CNTs and two side gates. The ring circuitry is not shown.

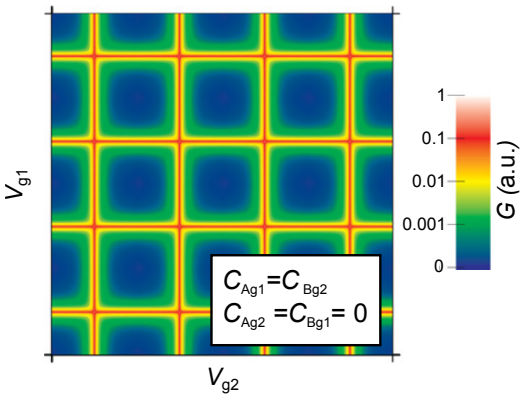

Figure 4.42 Expected conductance peak traces for symmetric capacitive coupling of each gate to the respective nearest CNT, $C_{Ag1} = C_{Bg2}$, and no coupling to the opposite transport channel, $C_{Ag2} = C_{Bg1} = 0$.

gate axes. This proves that both gates indeed have an effect on the conductance of the device, but are each capacitively coupled to both tubes, $C_{Ag2} \neq 0$ and $C_{Bg1} \neq 0$.

Furthermore, the two line sets are sloped in the same direction, which suggests weaker capacitive coupling C_{Ag1} and C_{Bg1} of the first gate to both its near as well as its far tube compared to the coupling C_{Ag2} and C_{Bg2} of the other gate to the two CNTs, i. e. $C_{Bg2} > C_{Ag2} > C_{Ag1} > C_{Ag2}$. This might result from an asymmetric placement of the gate electrodes with respect to the transport channels. One gate is probably located considerably farther away from the CNT ring than the other gate.

Other features of the simultaneous gating measurement are not so easy to explain. First of all, one line set is observed much more frequently than the other, i. e. the two sets have different line spacing. Furthermore the individual lines of the more prominent group are separated by irregular distances. They appear as single lines as well as clustered in pairs and triples. Even the lines of a triple do not show equal spacing over the entire V_{g1}-V_{g2} range and are also not exactly parallel, as indicated by the dashed lines in Fig. 4.43 which presents a section of the pattern shown in Fig. 4.40. On top of that the conductance can vary between different as well as along one trace as pointed out by the circles in the same image. Finally, Fig. 4.44 shows a crossing point of two lines belonging to different sets. Fluctuations and extensive conductance rise wash out the same, but clearly the line in more horizontal direction really consists of two parallels separated by an offset. One of these two lines vanishes on either side of the crossing point, as highlighted by the arrows.

It was also attempted to track one of the crossing points of two conductance lines attributed to the two different CNT channels. At these intersections, the Coulomb blockade of both quantum dots is lifted and both contribute simultaneously to the total transport through of the system. Only then it does effectively form a ring, and only then Aharonov-Bohm oscillations in the magnetoresistance of the device might be expected if electrons additionally retain their phase memory during passage through the CNTs. However, due to fluctuating background

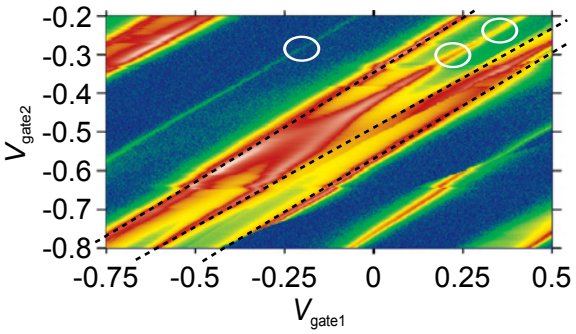

Figure 4.43 Cutout from the plot in Fig. 4.40 with identical scale and color-coding of the current. The conductance traces marked by the dashed lines are not spaced equidistantly and are not exactly parallel. The white circles point out intensity variations within and between lines.

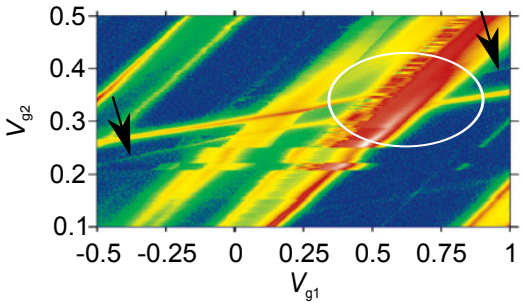

Figure 4.44 Cutout from the plot in Fig. 4.40 with identical scale and color-coding of the current. A crossing point of two lines belonging to different sets (white circle) and the two offset parallels vanishing on either side (black arrows) are marked.

charges and gate drift, maintaining a well-defined transport state of the sample could not be achieved for a sufficiently long time to ramp a considerable field interval. Therefore, periodic magnetoresistance oscillations could not be observed so far. Further measurements for the investigation of coherence in transport through CNTs need to be carried out on similar samples. For reasons that become clear in the course of Sec. 4.3.4, an observation of Aharonov-Bohm signatures would furthermore have been hindered by the specific assembly of the sample presented here. Nevertheless the data collected up to now supplies material for a detailed analysis which is presented in the following.

4.3.3 Transport Simulations

The observation of double and triple lines in the more prominent set 1 of the simultaneous gating measurements presented in the previous chapter in Fig. 4.40 lead to the assumption that one of the CNT arms might consist not only of a single, but of a bundle with at least two closely spaced tubes as illustrated in Fig. 4.45.

Thus, a model was developed for the investigation of transport through several CNTs connected via tunneling barriers to two Fermi reservoirs, capacitively coupled to two gates and additionally among each other. Its evaluation showed that the features observed in the measurements can be reproduced if three quantum dots are considered. The equivalent circuit of such a device is sketched in Fig. 4.46.

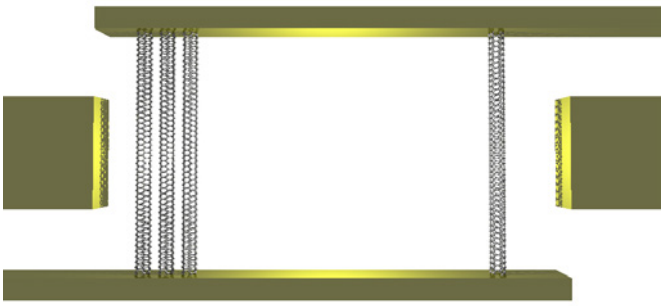

Figure 4.45 Sketch of a CNT sample with three closely spaced tubes instead of a single one forming one of the ring boundaries.

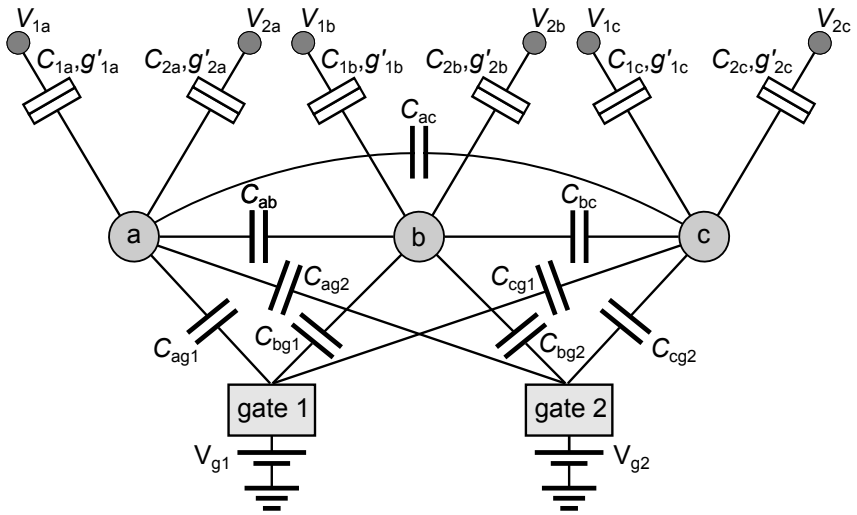

Figure 4.46 Circuit of three quantum dots connected via tunneling barriers to the two same Fermi reservoirs 1 and 2. All three are capacitively coupled to two gates $g1$ and $g2$, and additionally also among each other.

In principle, the current through this setup can be calculated following the same master equation approach as applied to the SET and QD in Sec. 2.4. However, a state $\vec{n}$ of the system is now no longer described by the number of electrons on one island. A matrix formulation of the respective equations is therefore required to describe the mutual dependence of every dot on all others. This is also detailed in the appendix of Ref. 75.

For simplicity, we first consider only three capacitively coupled dots with one energy level each that can either be singly occupied or empty. Furthermore, transport shall again be determined by sequential tunneling. Thus, eight states of the device and a limited number of allowed transitions listed in Tab. 4.1 have to be considered.

Table 4.1 Overview over the states $\vec{n}$ of the system sketched in Fig. 4.46 if each dot j has a single energy level that can either be singly occupied or empty. The allowed transitions between states considering only sequential tunneling are also listed.

state $\vec{n}$	**dot occupation (a, b, c)**	**allowed single electron transitions from state** $\vec{n}$ $\vec{n} \longrightarrow \vec{m}$
$\vec{0}$	(0, 0, 0)	$\vec{0} \longrightarrow \vec{1}$, $\vec{0} \longrightarrow \vec{2}$, $\vec{0} \longrightarrow \vec{3}$
$\vec{1}$	(1, 0, 0)	$\vec{1} \longrightarrow \vec{0}$, $\vec{1} \longrightarrow \vec{4}$, $\vec{1} \longrightarrow \vec{5}$
$\vec{2}$	(0, 1, 0)	$\vec{2} \longrightarrow \vec{4}$, $\vec{2} \longrightarrow \vec{0}$, $\vec{2} \longrightarrow \vec{6}$
$\vec{3}$	(0, 0, 1)	$\vec{3} \longrightarrow \vec{5}$, $\vec{3} \longrightarrow \vec{6}$, $\vec{3} \longrightarrow \vec{0}$
$\vec{4}$	(1, 1, 0)	$\vec{4} \longrightarrow \vec{2}$, $\vec{4} \longrightarrow \vec{1}$, $\vec{4} \longrightarrow \vec{7}$
$\vec{5}$	(1, 0, 1)	$\vec{5} \longrightarrow \vec{3}$, $\vec{5} \longrightarrow \vec{7}$, $\vec{5} \longrightarrow \vec{1}$
$\vec{6}$	(0, 1, 1)	$\vec{6} \longrightarrow \vec{7}$, $\vec{6} \longrightarrow \vec{3}$, $\vec{6} \longrightarrow \vec{2}$
$\vec{7}$	(1, 1, 1)	$\vec{7} \longrightarrow \vec{6}$, $\vec{7} \longrightarrow \vec{5}$, $\vec{7} \longrightarrow \vec{4}$

Each of the three CNTs j, $j \in \{a, b, c\}$, carries a different offset charge $en_{0,j}$ induced by the bias drop across the respective tunneling barrier i, $i \in \{1, 2\}$, and both gate voltages $V_{\mathrm{g}1}$ and $V_{\mathrm{g}2}$

$$en_{0,j} = C_{1j}V_{1j} + C_{2j}V_{2j} + C_{j\mathrm{g}1}V_{\mathrm{g}1} + C_{j\mathrm{g}2}V_{\mathrm{g}2}. \tag{4.21}$$

These quantities can be summarized in an *offset charge vector* $\vec{n}_0$.
The energy scales relevant for transport can be listed in a *charging energy matrix* $\mathbf{E}_\mathrm{C}$ given by

$$\mathbf{E}_\mathrm{C} = \frac{e^2}{2}\mathbf{C}^{-1} \tag{4.22}$$

where the diagonal elements describe the charging energies and the off-diagonal terms the coefficients of inter-dot coupling. $\mathbf{C}^{-1}$ denotes the inverse of the capacitance matrix defined by $C_{ii} = C_{\Sigma i}$ and $C_{ij} = C_{ji}$ for $i \neq j$

$$\mathbf{C} = \begin{pmatrix} C_{\Sigma 1} & -C_{ab} & -C_{ac} \\ -C_{ab} & C_{\Sigma 2} & -C_{bc} \\ -C_{ac} & -C_{bc} & C_{\Sigma 3} \end{pmatrix}. \tag{4.23}$$

The energy required to charge up the system by $e\vec{n}$ is then with $\Delta\vec{n} = \vec{n} - \vec{n}_0$

$$E_{\mathrm{ch}}(\vec{n}) = \Delta\vec{n}\mathbf{E}_\mathrm{C}\Delta\vec{n}. \tag{4.24}$$

In accordance with Ref. 75, $E_{\mathrm{ch}}(\vec{n}_0) = 0$ is chosen as the zero-point of energy. If one electron tunnels onto island j via barrier i, an energy change

$$\Delta E_{i,j}(\vec{n}) = E_{\mathrm{ch}}(\vec{n}_j) - E_{\mathrm{ch}}(\vec{n}) + eV_{ij} + o_j, \tag{4.25}$$

results, where $\vec{n}_j$ denotes the charge vector with j-th entry $n_j + 1$ if n_j is the initial charge on dot j before the transition. Furthermore, an additional offset o_j of the energy level of dot j with respect to the Fermi surface is included in Eq. (4.25).
Next, the transition rates from a state $\vec{n}$ to a state $\vec{m}$, $\Gamma_{\vec{n}\to\vec{m}}$, have to be determined. In Sec. 2.4, tunneling through a single quantum dot was described assuming infinitely sharp energy levels. In this case, the rates resulting from Fermi's Golden Rule for the transition from a state n to a state $n + 1$ across the tunneling barrier i are, as stated in Eq. 2.23,

$$\Gamma_{i,n\to n+1} = \frac{\tilde{g}_i}{h}\frac{1}{\exp(\beta\Delta E_i(n)) + 1}$$

with a factor $\tilde{g}_i$ of dimension of energy quantifying the coupling strength of the dot level to contact i. Yet, this approach does not describe the situation accurately at temperatures near $T = 0$, as pointed out at the conclusion of Sec. 2.4. In the SQTM, an energy level of the dot and the Fermi energy of the respective electrode have to be exactly aligned to allow tunneling, otherwise energy conservation would be violated. However, in resonance the intermediate level is occupied only for a very short time. This finite lifetime τ_n leads to an "intrinsic" level broadening caused by the uncertainty relation between time and energy [90] derived from

Heisenberg's uncertainty principle [91]. To improve results for low temperatures, this lifetime broadening of the dot levels has to be included in the transport model.
For resonant tunneling through an isolated quantum dot with only a single level at energy ϵ_0, one finds in the literature a resulting net current [51]

$$I = \frac{2e}{h}\int_{-\infty}^{\infty} T(E,V)[F(E-eV)-F(E)]\mathrm{d}E, \tag{4.26}$$

where $F(E)$ is the Fermi function

$$F(E) = \frac{1}{\exp[\beta(E-E_\mathrm{F})]+1}$$

introduced in Eq. (2.11) with $\beta = (k_\mathrm{B}T)^{-1}$.
The transmission $T(E,V)$ can be approximated by

$$T(E,V) = \frac{4\mathbf{\Gamma_1}\mathbf{\Gamma_2}}{(E-\epsilon_0)^2+(\mathbf{\Gamma_1}+\mathbf{\Gamma_2})^2}. \tag{4.27}$$

Here, the scattering rates $\mathbf{\Gamma_1}$ and $\mathbf{\Gamma_2}$ have dimensions of energy. They describe the strength of the coupling to the electrodes and thus the lifetime broadening of the resonant level. For the transition rates $\Gamma_{i,n\to n+1}$ from state n to $n+1$ across contact i (in Hz), this formulation motivates the phenomenological ansatz

$$\Gamma_{i,n\to n+1} = \frac{g_i'}{2}\int_{-\infty}^{+\infty}\mathrm{d}E\frac{\gamma_{n+1}\cdot h}{(E-E_\mathrm{ch}(n+1))^2+(\gamma_{n+1}\cdot h/2)^2}\cdot F(E-\Delta E_i(n)), \tag{4.28}$$

where $\gamma_n \propto \tau_n^{-1}$ and g_i' is given in units of $e^2/(2hC_i)$. $F(E)$ is the Fermi distribution of the electrodes, $\Delta E_i(n)$ the energy difference specified in Eq. (2.16) and h denotes Planck's constant. At $T = 0$ the integral can be solved analytically and Eq. (4.28) can be written in the form

$$\Gamma_{i,n\to n+1} = g_i'\cdot\left[\mathrm{atan}\left(\frac{-2\Delta E_i(n)}{\gamma_{n+1}\cdot h}\right)+\frac{\pi}{2}\right]. \tag{4.29}$$

As the lifetime of every level n is dominated by sequential tunneling events, it is

$$\gamma_n = \Gamma_{n\to n+1}+\Gamma_{n\to n-1}, \tag{4.30}$$

where

$$\Gamma_{k\to m} = \Gamma_{1,k\to m}+\Gamma_{2,k\to m}, \tag{4.31}$$

Via this relation and Eq. (4.28) the transition rates are inversely defined. Numerically, the resulting set of equations can be solved by iteration. Afterwards the probabilities p_n to find the dot in a respective state can be determined via the master equation method detailed before in Sec. 2.4 (see Eqs. (2.20) and (2.21)).
If we consider again, similarly to Sec. 4.2, the simple case of just one level that is either filled or empty, it is

$$\gamma_0 = \Gamma_{0\to 1} \text{ and } \gamma_1 = \Gamma_{1\to 0} \tag{4.32}$$

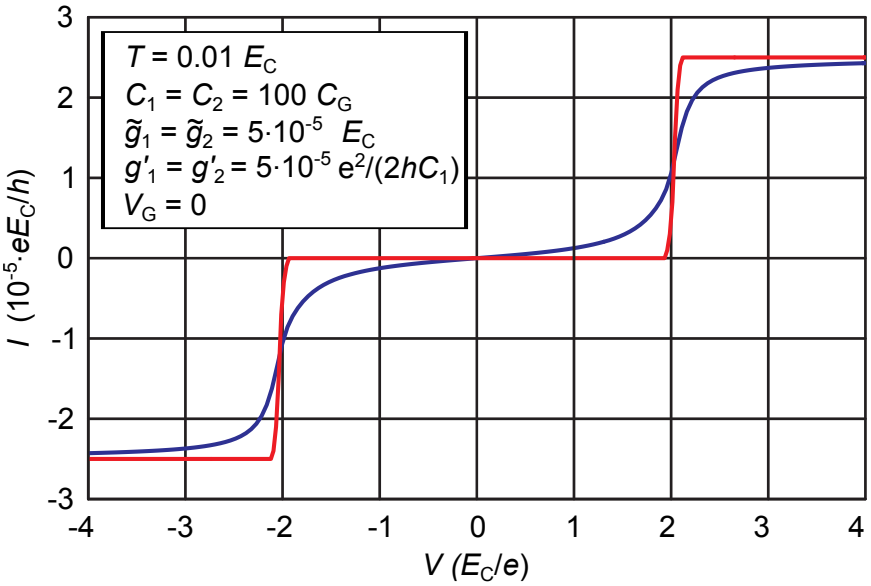

Figure 4.47 Current through a quantum dot with one level that can be either in the empty or occupied state. Two different computational models are compared. In the first, only thermal broadening of the density of states of the electrodes is taken into account (red curve) whilst in the second also lifetime broadening of the dot states is considered (blue curve).

In Fig. 4.47 the current derived according to Eq. (2.29)

$$I = -e(p_1\Gamma_{i,1\to 0} - p_0\Gamma_{i,0\to 1})$$

is compared for the case that only thermal level broadening of the dot states is considered with the transition rates given by Eq. (2.23) (red curve) and the case that the effect of intrinsic level broadening is included using Eq. (4.28) (blue curve). The reduced transition width in the red curve is obvious.

The model can also be expanded to include more than one energy level of the quantum dot. The current through such a system in dependence of bias and gate voltage is shown in the Coulomb-blockade pattern in Fig. 4.48. Comparison to the Coulomb diamonds of a metallic dot in Fig. 2.14 illustrates the gradual onset of current below the Coulomb blockade threshold instead of a sharp onset at this voltage.

We now proceed with the calculation of transport through a system of three capacitively coupled quantum dots. Intrinsic level broadening shall be taken into account in this case, too. In view of the recursive definition of the lifetime broadening of the levels of a single dot given in Eq. (4.28) we approximate

$$\Gamma_{i,\vec{n}\to\vec{m}} = \frac{g'_{i,j}}{2}\int_{-\infty}^{+\infty} \mathrm{d}E \frac{\gamma_{\vec{m}}\cdot h}{(E \pm E_{\mathrm{ch}}(\vec{m}))^2 + (\gamma_{\vec{m}}\cdot h/2)^2}\cdot F(E \mp \Delta E_{i,j}(\vec{n})), \tag{4.33}$$

where $\vec{n}$ now no longer denotes the amount of electrons on a dot, but the number assigned to the respective state of the entire system. This formulation is only valid for all transitions $\vec{n} \to \vec{m}$

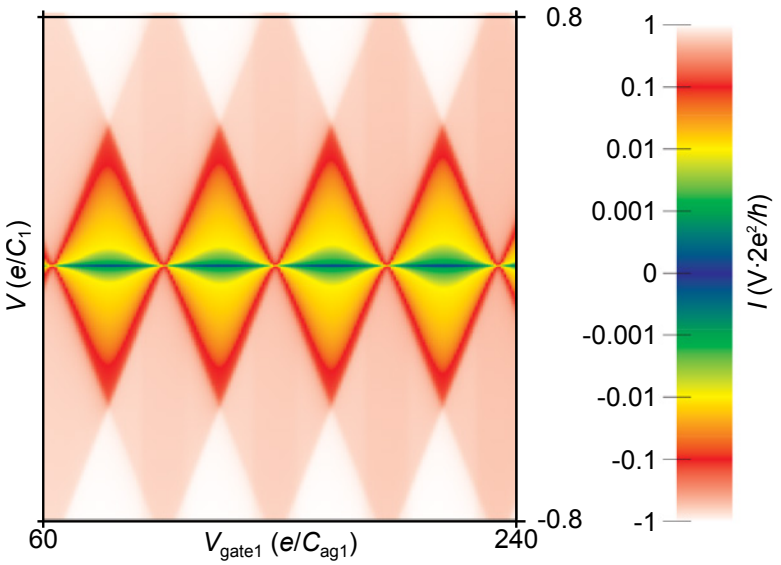

Figure 4.48 Coulomb blockade pattern of a quantum dot with several energy levels. Intrinsic level broadening is taken into account in the numerical calculation of the current through the device in dependence of bias and gate voltage. The used parameters are $C_1 = C_2 = 50C_G$, $g_1' = g_2' = 5 \cdot 10^{-3} e^2/(2hC_1)$ and $T = 0$.

allowed within the SQTM, i. e. which involve only one dot j, $j \in \{a, b, c\}$ (see Tab. 4.1). Thus, for a given process $\vec{n} \to \vec{m}$, j is fixed. The signs depend on whether an electron is removed from or added to that respective dot.
As before, $\gamma_{\vec{n}} \propto \tau_{\vec{n}}^{-1}$ is determined by the rates of allowed transitions from state $\vec{n}$ to other states, which are all given in Tab. 4.1:

$$\begin{aligned} \text{(I)} \quad \gamma_{\vec{0}} &= \Gamma_{\vec{0}\to\vec{1}} + \Gamma_{\vec{0}\to\vec{2}} + \Gamma_{\vec{0}\to\vec{3}} \\ \text{(II)} \quad \gamma_{\vec{1}} &= \Gamma_{\vec{1}\to\vec{0}} + \Gamma_{\vec{1}\to\vec{4}} + \Gamma_{\vec{1}\to\vec{5}} \\ \text{(III)} \quad \gamma_{\vec{2}} &= \Gamma_{\vec{2}\to\vec{4}} + \Gamma_{\vec{2}\to\vec{0}} + \Gamma_{\vec{2}\to\vec{6}} \\ &\vdots \end{aligned} \tag{4.34}$$

Thus, the transition rates are recursively defined by Eq. (4.33) and the equation set (4.34), which can be solved numerically.
With the resulting $\Gamma_{\vec{n}\to\vec{m}}$, stationary state master equations for the probabilities $p_{\vec{n}}$, $\sum_{\vec{n}} p_{\vec{n}} = 1$, to find the system in state $\vec{n}$ can be set up, again including all the allowed transitions listed in Tab. 4.1, namely

$$\begin{aligned} \text{(I)} \quad 0 &= p_{\vec{0}}(\Gamma_{\vec{0}\to\vec{1}} + \Gamma_{\vec{0}\to\vec{2}} + \Gamma_{\vec{0}\to\vec{3}}) - p_{\vec{1}}\Gamma_{\vec{1}\to\vec{0}} - p_{\vec{2}}\Gamma_{\vec{2}\to\vec{0}} - p_{\vec{3}}\Gamma_{\vec{3}\to\vec{0}} \\ \text{(II)} \quad 0 &= p_{\vec{1}}(\Gamma_{\vec{1}\to\vec{0}} + \Gamma_{\vec{1}\to\vec{4}} + \Gamma_{\vec{1}\to\vec{5}})) - p_{\vec{0}}\Gamma_{\vec{0}\to\vec{1}} - \dots \\ \text{(III)} \quad 0 &= p_{\vec{2}}1(\Gamma_{\vec{2}\to\vec{4}} + \Gamma_{\vec{2}\to\vec{0}} + \Gamma_{\vec{2}\to\vec{6}}) - \dots \\ &\vdots \end{aligned} \tag{4.35}$$

This equation set, too, can be solved numerically. The total current through the device can then be derived by summing over the contributions of all three quantum dots

$$I = I_{\mathrm{a}} + I_{\mathrm{b}} + I_{\mathrm{c}}. \tag{4.36}$$

For each CNT the current is determined by the allowed transitions $\vec{n} \rightarrow \vec{m}$. For I_{a} e. g. it results

$$\begin{aligned} I_{\mathrm{a}} = I_{1\mathrm{a}} = I_{2\mathrm{a}} = -e[&(p_{\vec{0}}\Gamma_{i,\vec{0}\rightarrow\vec{1}} - p_{\vec{1}}\Gamma_{i,\vec{1}\rightarrow\vec{0}}) + (p_{\vec{2}}\Gamma_{i,\vec{2}\rightarrow\vec{4}} - p_{\vec{4}}\Gamma_{i,\vec{4}\rightarrow\vec{2}}) + \\ &(p_{\vec{3}}\Gamma_{i,\vec{3}\rightarrow\vec{5}} - p_{\vec{5}}\Gamma_{i,\vec{5}\rightarrow\vec{3}}) + (p_{\vec{6}}\Gamma_{i,\vec{6}\rightarrow\vec{7}} - p_{\vec{7}}\Gamma_{i,\vec{7}\rightarrow\vec{6}})] \end{aligned} \tag{4.37}$$

where $\sigma(\vec{n}, \vec{m})$ is the difference of the number of electrons on the system in state $\vec{n}$ and state $\vec{m}$. The results of these calculations are presented in color-coded plots of I vs. V_{g1} and V_{g2} in the next section.

4.3.4 Comparison of Experiment and Calculations

In the previous section the current through a system of three, instead of one, CNTs connected via tunneling barriers to two Fermi reservoirs and capacitively coupled to two gates was calculated. If three identical islands without capacitive coupling to each other are considered, the conductance of the system simply rises a by a factor of three compared to the single conductor. Still, only one peak appears in the dependence of the current I on the two gate voltages V_{g1} and V_{g2} as illustrated in Fig. 4.49. Yet, as soon as capacitive coupling among the dots is switched on, three individual conductance peak lines can be distinguished as shown in Fig. 4.50. Due to their mutual coupling, a charge on one island also shifts the energy spectrum of the other two with respect to the Fermi energy E_{F} and vice versa, i. e. the three CNTs mutually gate each other. Thus, the dots drive each other in and out of transport and the system is only in a steady state, not in equilibrium, for a given gate-voltage configuration.
In contrast to the simulation plot in Fig. 4.50 however, the conductance line triples appearing in the simultaneous-gating measurements in Fig. 4.40 are not equidistant over the entire V_{g1}-V_{g2} range. This variance in spacing can also be reproduced with our model if the offset o_j of the energy level of one of the three dots is shifted with respect to the Fermi level (see Fig. 4.51). In addition, this parameter change leads to different conductance of the three lines as well as to the appearance of additional resonances caused by the displacement of level spectra with respect to each other.
The observed experimental features also include different slope of lines belonging to the same set, as indicated in the cutout shown in Fig. 4.43. Confirmed by the numerical simulations, this can be attributed to stronger capacitive coupling of one CNT to one of the gates, as illustrated in Fig. 4.52. Furthermore, the variance of conductance along one single line can be explained with dissimilar capacitive coupling C_{jgi} and tunneling strength $g_{i,j}$ of the CNTs to the two Fermi reservoirs. The result of the corresponding calculations is displayed in Fig. 4.53. The influence of a weaker coupled dot on the energy shift and conductance of the other islands is equally weaker. Figure 4.54 finally summarizes all these effects, which yield a strong similarity to the data of Fig. 4.43.

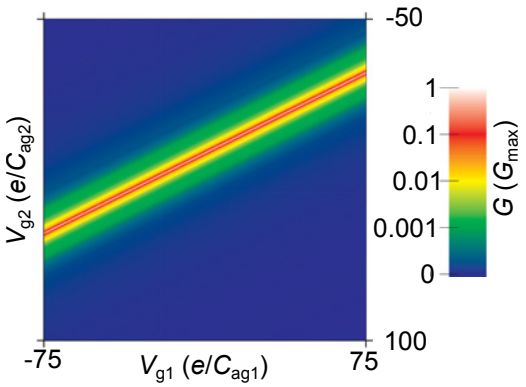

Figure 4.49 Color-coded current vs. gate-voltages plot of three identical, isolated transport channels. Only one narrow conductance peak appears in the V_{g1}-V_{g2} spectrum. The parameters used for the simulation are, in units of C_{a1}: $C_{a1} = C_{b1} = C_{c1} = C_{a2} = C_{b2} = C_{c2} = 1$, $C_{ag1} = C_{bg1} = C_{cg1} = 0.02$, $C_{ag2} = C_{bg2} = C_{cg2} = 0.01$, $C_{ab} = C_{bc} = C_{ac} = 0$, $g'_{a1} = g'_{b1} = g'_{c1} = g'_{a2} = g'_{b2} = g'_{c2} = 0.005\, e^2/(2hC_{a1})$, $o_a = o_b = o_c = 0$, $V_{g1} = -75 - 75\, e/C_{ag1}$, $V_{g2} = -50 - 100\, e/C_{ag2}$, $V = 1 \cdot 10^{-5}\, e/C_{a1}$ and $T = 0$.

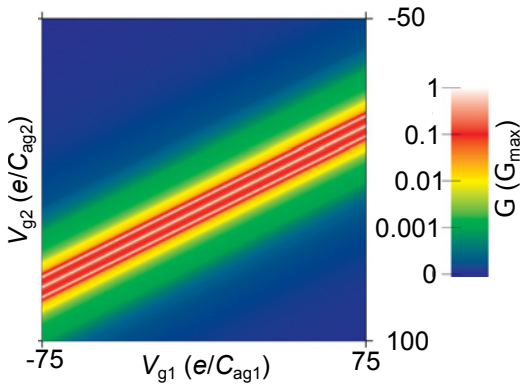

Figure 4.50 Color-coded current vs. gate-voltages plot of three identical, but additionally capacitively coupled quantum dots. Three separate conductance peaks can now be distinguished. The parameters used for the simulation are the same as for Fig. 4.49, with the exception of $C_{ab} = C_{bc} = C_{ac} = 0.25$.

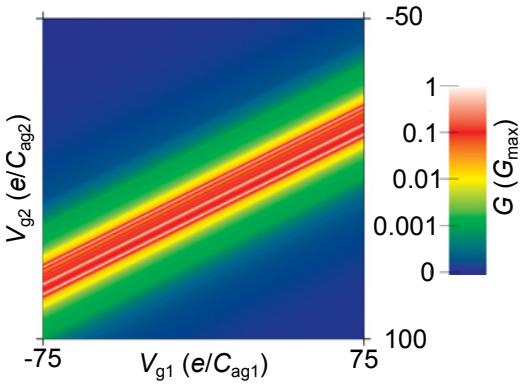

Figure 4.51 Color-coded I vs. V_{g1}/V_{g2} plot calculated with the model described in the previous section. The three capacitively coupled quantum dots are identical except for an energy offset introduced for the level of one island. This results in a peak distance variation and the appearance of additional resonances. The simulation parameters are the same as for Fig. 4.50, but $o_b = 0.1\, E_{ch}$.

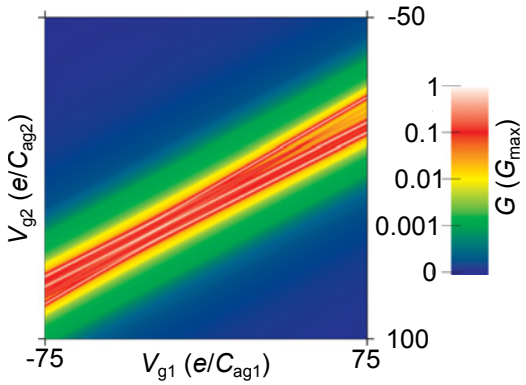

Figure 4.52 Color-coded I vs. V_{g1}/V_{g2} plot calculated with the model described in the previous section. One of the three considered quantum dots is stronger capacitively coupled to one of the gates than the others, which leads to different slope of conductance peak traces. The parameters used for the simulation are the same as for Fig. 4.50, except for $C_{ag2} = 0.012$.

An explanation for the crossing behavior of conductance traces belonging to the two different line sets can also be derived with the help of the numerical simulations discussed here. For that purpose, only two dots are taken into account, each capacitively coupled to only one of the

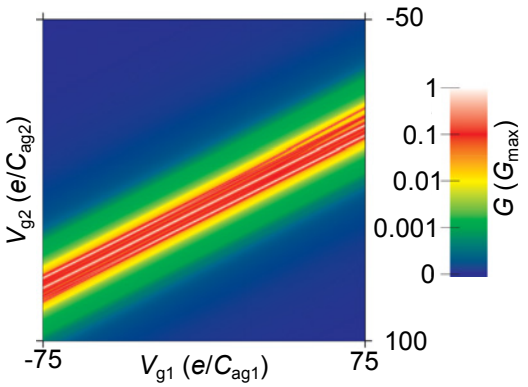

Figure 4.53 Result of numerical I vs. V_{g1} and V_{g2} calculations. The color scale can be found on the right. One of the three transport channels shows weaker coupling to the leads, which yields varying current amplitude within the conductance lines. The parameters used for the simulation are the same as for Fig. 4.50. Only $g'_{a1} = g'_{a2} = 0.00125\, e^2/(2hC_{a1})$ and $C_{ag2} = 0.011$ are different.

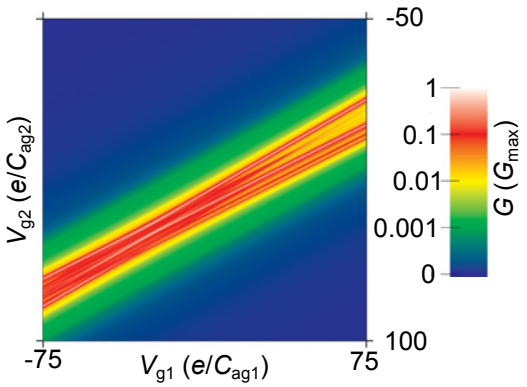

Figure 4.54 Summary of the low temperature transport features of three capacitively coupled quantum dots. The simulation parameters $g'_{b1} = g'_{b2} = 0.00125\, e^2/(2hC_{a1})$, $C_{ag2} = 0.012$ and $o_b = -0.05$ were changed simultaneously to produce differing distance and slope of the lines as well as conductance variation within traces. All other simulation parameters are those given in Fig. 4.50. The resulting I vs. V_{g1}/V_{g2} plot strongly resembles the measurement cutout in Fig. 4.43.

gates. Different tunneling strength to the leads causes dissimilar peak height and broadening as shown in Fig. 4.55. The reduction of conduction directly at the crossing point of the capacitively uncoupled system can be attributed to a suppressed transition rate from the state (0,0), i. e. both dots empty, to (1,1), i. e. both dots occupied, as cotunneling processes are less likely than sequential tunneling events. The shift in the horizontal line is a direct consequence of the capacitive coupling of both CNTs to each other, i. e. it is a sign of mutual gating. The conductance state of one dot is shifted in energy, i. e. also with respect to the applied gate voltages, depending on whether the other dot is occupied or empty. As the capacitive coupling of the quantum dots quickly reduces with distance but still clearly reflects itself in the intersections of the two different line sets, it might be assumed that the fourth CNT comprising the other arm of the ring geometry is also not spaced as far apart from the bundle as expected.

The numerical model described so far can also reproduce the low bias regime of gate-bias plots, though no complete Coulomb diamond pattern, as only one state per dot is included. A calculation for three identical CNTs capacitively coupled among each other with $C_{ab} = C_{ac} = C_{bc}$ is presented in Fig. 4.56. The gate voltages for which Coulomb blockade is suppressed are split into three values, whose spacing depends on the magnitude of $C_{jj'}$. In the voltage range in between, the blockade regime is significantly reduced and therefore hardly resolvable experimentally. This corresponds to the observation of Coulomb blockade suppression over an entire gate-voltage range in the measurements shown in Figs. 4.38 and 4.39.

For a closer investigation of the shape of Coulomb diamonds resulting from transport through three capacitively coupled quantum dots, the number of energy levels per dot was expanded to three each at $T = 0$, where the integral in Eq. (4.33) can be solved analytically. First,

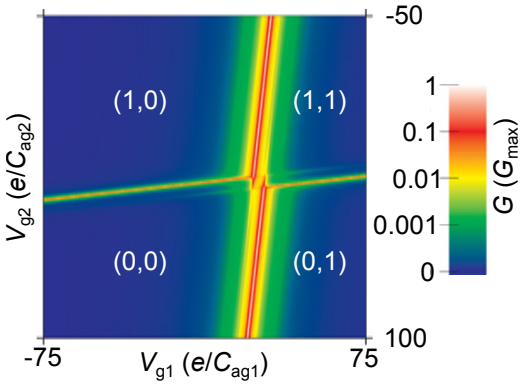

Figure 4.55 Color-coded I vs. V_{g1}/V_{g2} plot derived from numerical simulations of two quantum dots capacitively coupled among each other and to only one of the two existing gates. Additionally, one transport channel is coupled more weakly to the leads than the other channel. Conductance reduction directly at the peak crossing as well as parallel line shift left and right of the same can be observed. The simulation parameters in units of C_{a1} are: $C_{a1} = C_{b1} = C_{a2} = C_{b2} = 1$, $C_{ag1} = 0$, $C_{bg1} = 0.02$, $C_{ag2} = 0.02$, $C_{bg2} = 0$, $C_{ab} = 0.25$, $g'_{a1} = g'_{a2} = 0.005\,e^2/(2hC_{a1})$, $g'_{b1} = g'_{b2} = 0.0005\,e^2/(2hC_{a1})$, $o_a = 0$, $o_b = -0.05\,E_{ch}$, $V_{g1} = -75 - 75\,e/C_{ag1}$, $V_{g2} = -50 - 100\,e/C_{ag2}$, $V = 1 \cdot 10^{-5}\,e/C_{a1}$ and $T = 0$.

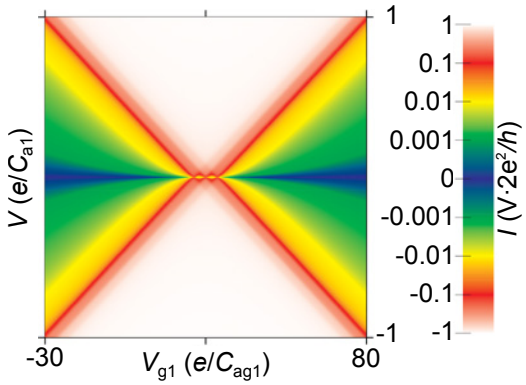

Figure 4.56 I vs. V_{g1} and V_{bias} plot. The color scale is displayed on the right. The Coulomb diamond pattern in the low bias regime has been calculated with the model explained in the previous section. A reduction, almost vanishing, of the current blockade over a continuous voltage range can be derived. The parameters used for the simulation are in units of C_{a1}: $C_{a1} = C_{b1} = C_{c1} = C_{a2} = C_{b2} = C_{c2} = 1$, $C_{ag1} = C_{bg1} = C_{cg1} = 0.02$, $C_{ag2} = C_{bg2} = C_{cg2} = 0.01$, $C_{ab} = C_{bc} = C_{ac} = 0.2$, $g'_{a1} = g'_{b1} = g'_{c1} = g'_{a2} = g'_{b2} = g'_{c2} = 0.005\,e^2/(2hC_{a1})$, $o_a = o_b = o_c = 0$, $V_{g1} = -30 - 80\,e/C_{ag1}$, $V_{g2} = 0$, $V = -1 - 1\,e/C_{a1}$ and $T = 0$.

only those transitions between the resulting 2^9 states of the system which change the total number of electrons by ± 1, i. e. only sequential tunneling, are taken into account and rates calculated for them. Including these allowed transitions of ± 1, steady state master equations can subsequently be set up and solved numerically, analogously to the previously described procedure. Figure 4.57 shows a Coulomb blockade pattern calculated with this approach. As in Fig. 4.56, a significant reduction of the diamonds can be observed over a continuous voltage range. Additionally, the superposition of transport states leads to diffusive onset of current flow through the device. The edges of the Coulomb diamonds are not sharp and the blockade extend varies significantly. Furthermore, in the low bias regime, which is enlarged in Fig. 4.58, signatures of excited states can hardly be detected. Comparison with the experimentally obtained plots shows that this was also the range in which the measurements were performed. Application of higher bias voltages might have revealed the contribution of excited states to the conductance of the system.

So far no inelastic scattering processes were included in the calculations of transport through quantum dots. However, within the SQTM electron tunneling to an excited state of one of the islands followed by relaxation to a lower, unoccupied energy level (if existent) is conceivable. Such processes can occur if the life time of a dot level is shorter than the tunneling time. Implementing these inelastic processes into the numerical simulations leads to further washing out of the Coulomb diamonds as illustrated in Fig. 4.59. The obtained blockade pattern strongly

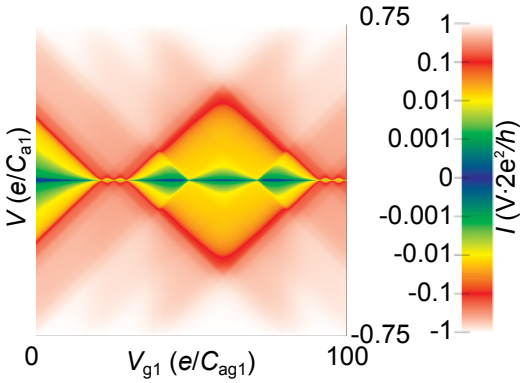

Figure 4.57 Coulomb-diamond pattern computed for a system of three capacitively coupled quantum dots with three energy levels contributing to transport each. The color scale for the I vs. V_{g1} and V_{bias} plot is given on the right. Irregular size and shape and washed-out onset of current flow as well as nearly complete suppression of blockade over a continuous voltage range can be reproduced with this model. The simulation parameters are identical to those given in Fig. 4.56, except for $V_{g1} = 0 - 100$ and $V = -0.75 - 0.75$. Additionally, $o_a = o_b = o_c = 0, 0.2$ and $0.4 E_{ch}$.

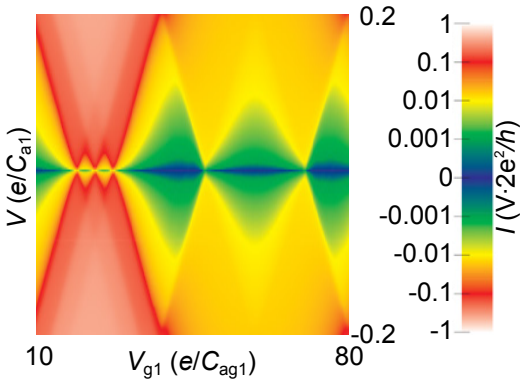

Figure 4.58 Enlarged low bias regime of a I vs. V_{gate} and V_{bias} dependence calculated with the same model used for Fig. 4.57. The color scale of the Coulomb diamond patter is displayed on the right.

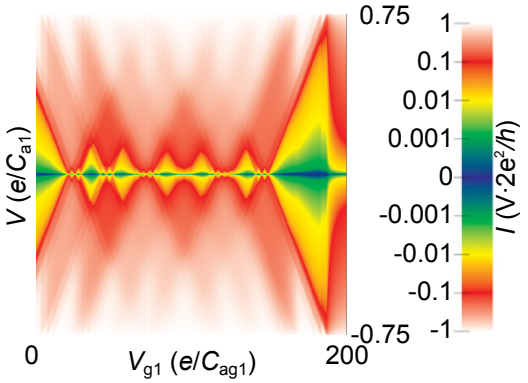

Figure 4.59 Coulomb diamond pattern. For the computation of this I vs. V_{gate} and V_{bias} plot (color scale given on the right) inelastic processes, namely relaxation of tunneling electrons to lower unoccupied energy levels, were also taken into account. The simulation was performed with the same parameters as for Fig. 4.57, except for the range of $V_{g1} = 0 - 200\, e/C_{a1}$.

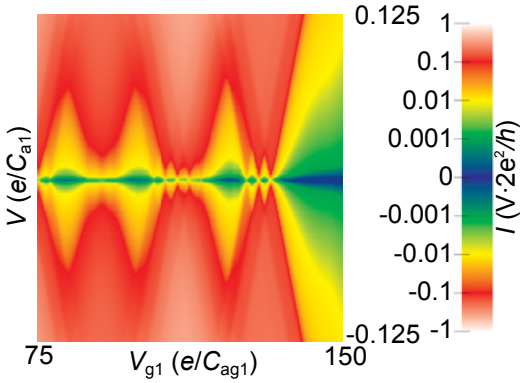

Figure 4.60 Zoom into the low bias regime of the Coulomb diamond pattern shown in Fig. 4.59. The color scale of the current can be found on the right.

resembles the data presented in Figs. 4.38 and 4.39, which indicates that the effect of relaxation processes on transport through a system of capacitively coupled quantum dots is not negligible and that more than one dot state contributes to transport.

5 Summary and Outlook

The goal of this thesis was the investigation of molecular transport with the focus on phase coherence. Thus, for a beginning doubly connected structures required for Aharonov-Bohm measurements were fabricated by standard electron beam lithography. The next step, the contacting of macromolecules, demanded nanometer-spaced metallic electrodes. These dimensions are not available to standard lithography techniques. Nevertheless, single-molecule transport data was acquired already by several research groups using various other methods. However, their shortcomings range from poor selectivity of measurements on sandwiched SAMs over mechanical instability of contacts formed with an STM tip to the difficulty of implementing a gate electrode in MCBJs. The last issue can be overcome by employing electromigration to generate ultrasmall gaps bridgeable by molecules in metallic structures. Due to the planar geometry of samples prepared this way, an additional capacitively coupled contact can be placed in close proximity to the investigated junction. Furthermore, the resulting compact devices can also be cooled to cryogenic temperatures, which guarantees sufficient suppression of spatial and conformational changes. Additionally, in-situ deposition and on-line conductance monitoring can improve selectivity. Therefore, feedback-controlled electromigration was our method of choice for contacting single molecules.

According to the experience gathered in the course of our work with this technique, the process divides into three regimes. It begins with thermal annealing, which manifests itself in an increase of conductance. We attribute it to a reduction of defects, in particular grain boundaries, in the evaporated metal. After the annealing a steady increase of resistance sets in. At this stage the feedback loop can be operated reliably. The third and final regime, which is entered above about $80\,G_0$, on the other hand, is difficult to control as R-V curves no longer show a monotonic development. If the region of only a few conductance quanta is reached, telegraph noise can be observed as a sign of atomic rearrangement as well as step-like conductance decrease. Plateaus however seldom correspond to integer multiples of G_0. This indicates that transport channel transmission is not unity.

For a better understanding of the relation between structure thinning and measured resistance we recorded a series of in-situ SEM images from electromigrating rings as well as wires documenting the process of structural changes and mapped them to the simultaneously measured R-V traces. From the resulting movies we learned that ion displacement and the formation of voids and hillocks already start in the annealing regime. However, the effect of island coalescence seems to prevail, but cannot be resolved with the SEM. When the resistance finally slowly starts to increase, drastic changes in the nanostructure conformation occur already. With the help of these observations we can conclude that the main material displacement is accompanied by a relatively low increase of only 1-2 orders of magnitude in resistance. The most notable changes in the resistance towards the end of electromigration, on the other hand, correspond to only small alterations in geometry below the resolution of the SEM. With this

knowledge, it is easy to understand why the last part of the process is so difficult to control even with a feedback loop.
All electromigration experiments described in this chapter so far had been conducted at room temperature. We observed that under these conditions the substrate used for sample preparation plays a crucial role for the fabrication of closely spaced electrodes for molecule deposition. The use of p-doped silicon covered by a thin layer of native oxide instead of 400 nm thermally grown oxide substantially raised the yield of nanogaps. The decisive factor is the thermal coupling of the metallic sample structure to a temperature reservoir. It improves dissipation of Joule heat from the junction in the substrate and thus helps to avoid melting. We confirmed these experimental observations by modeling heat transport along the leads connected to the nanostructure and across the underlying substrate described by a two-dimensional Poisson equation.
The model developed for this purpose can also be applied for the optimization of the sample layout with respect to improved control over the location where electromigration sets in. However, the microstructure, especially grain boundaries competing with pre-structured constrictions, is not considered and remains an uncertainty factor. Nevertheless, helpful indications how to avoid undesired excessive current and temperature rise can be derived. Consequently, changing the sample layout from horizontally oriented to tilted squares helped us shift gap generation towards the center of the ring arms.
For immediate registration of resistance changes in the high-ohmic regime during deposition of molecules, we subsequently had to resort to thermally as well as electrically insulating substrates again. Therefore, electromigration in cold helium gas was investigated. This method raised the yield of slits only a few nanometers wide even on substrates covered by thick SiO_2 layers. However, one has to keep in mind previously reported observations of metallic clusters remaining in the gap region after electromigration at cryogenic temperatures [37–39]. These possible residues make a gate electrode and sufficient statistics necessary for conclusive data evaluation.
When the electromigration process had been mastered to this degree, experiments proceeded to the inclusion of molecules in the generated nanogaps. Unfortunately, the synthesis of sublimable molecules with substantial conductivity and sufficient size proved more time-consuming than expected. Therefore, preliminary experiments with molecular rods, more precisely oligo(phenylene ethynylene)s, deposited from solution were conducted in the meantime. Several attempts once yielded a non-vanishing conductance. As I-V curves were obtained at room temperature only and no use had been made of gating, interpretation of the measurements is difficult. Furthermore, acquisition of additional data for comparison was impeded by the shortcomings of electromigration. The irreversibility of gap formation, the limited control over junction size and the time-consuming sample preparation made it impossible to gather enough statistics in a reasonable time.
At this point it was consequently decided to focus on a different kind of macromolecules, namely carbon nanotubes (CNTs), which are long enough to be contacted by standard lithography techniques, i. e. sample preparation does no longer require electromigration. Instead, tungsten electrodes for the deposition of CNTs were prepared by common electron beam lithography. Subsequently, single (bundles of) tubes could be placed by ac-dielectrophoresis.

The result of this fabrication step was then checked by imaging with an SEM. Those structures displaying two parallel CNT conductance channels were selected for further processing. However, single tubes cannot be distinguished doubtlessly from closely spaced bundles in that way. Despite all preparative measures against it, the occurrence of bundle formation and deposition thus remains a possibility. After temperature annealing to get rid of charges implanted by electron beam exposure, the sample layout was finally completed with gold measurement contacts and two independently addressable gate electrodes in a second electron beam lithography step. Accurate positioning of the structures with dimensions of down to 50 nm could be achieved.
Subsequently, the samples were inserted into a ^{3}He-^{4}He dilution refrigerator which can reach a base temperature below 10 mK. One sample survived this procedure completely intact, including two functioning gates. Low-temperature transport measurements were performed on this specimen. First, the variation of conductance with the voltage applied to one gate was investigated separately for both electrodes in turn. The appearance of Coulomb diamonds in each case verified an influence of both gates on the conductance of the device. In continuation, the current amplitude for a fixed bias voltage in the linear response regime was recorded whilst both V_{g1} and V_{g2} were stepped simultaneously. Two conductance line sets with clearly different slope could be resolved. These experiments confirmed the existence of two CNT transport channels. However, the capacitive coupling of each gate to both quantum dots also manifested itself.
The experimentally resulting Coulomb diamonds showed pronounced differences to a simple numerical model as well as to previously published measurements. Their size, shape and sequence displayed no regularity over the investigated voltage range. Furthermore, no traces of excited states were detectable and in certain continuous voltage ranges the blockade signature vanished completely. Similarly, unexpected features were observed in the simultaneous gating measurements. First, the two discernible line sets had a different spacing. In the more closely spaced set, the distance between individual lines was irregular as well. They appeared not only isolated, but also in pairs and triples. Even the spacing within such a set of three conductance peak traces was not equidistant over the entire gating range. Furthermore, the lines also displayed a varying current amplitude between different and within one line and the traces are not exactly parallel. Finally, crossing points of lines belonging to different sets show no clear conductivity peak due to addition of conductances, but instead a parallel shift of the signature of the weaker transport channel.
For comparison to and interpretation of the experimental results, a model was then developed for the computation of current through a quantum dot, i. e. a spatially confined structure with discrete level spacing weakly coupled via tunneling barriers to two Fermi reservoirs. In contrast to previous considerations of this setup, not only thermal, but also intrinsic level broadening was taken into account. The experimentally observed transport characteristics lead to the assumption that one of the apparently single CNTs was indeed formed by a closely spaced bundle of (at least) three tubes, which are capacitively coupled to each other. Thus, they mutually influence their respective conductance states, i. e. mutually gate each other. The transport model was therefore expanded for the numerical calculation of the current flow through such a system of three quantum dots. The striking and unexpected features listed above could be reproduced with these simulations. Thus, the assumption of a larger than intended number of

conductance channels and their interaction could be confirmed. In addition, the influence of relaxation processes during tunneling events could be shown to reflect itself in the shape of Coulomb diamonds and wash out the onset of current.
Magnetoresistance measurements were also performed on the CNT sample. However, observation of Aharonov-Bohm oscillations was not achieved. On the one hand, this is due to experimental difficulties, mainly caused by fluctuating background charges and instrumental drift. On the other hand, the specific configuration of the measured device also hinders stabilization of a transport state where two CNT channels contribute to charge transport. As the CNTs are capacitively coupled to each other, they are very sensitive to the charge state of the respective other quantum dots and drive each other in and out of conductance.
In summary, we can neither confirm nor exclude coherence in transport through carbon nanotubes. However, we were able to measure and reproduce the low-temperature transport characteristics of a unique sample configuration incorporating a closely spaced bundle of three CNTs representing quantum dots capacitively coupled among each other.

Bibliography

[1] Y. Aharonov and D. Bohm, Significance of electromagnetic potentials in the quantum theory, *Phys. Rev.* **115**, 485 (1959)

[2] R. A. Webb, S. Washburn, C. P. Umbach and R. B. Laibowitz, Observation of h/e Aharonov-Bohm Oscillations in Normal-Metal Rings, *Phys. Rev. Lett.* **54**, 2696 (1985)

[3] S. Washburn and R. A. Webb, Aharonov-Bohm effect in normal metal: Quantum coherence and transport, *Adv. Phys.* **35**, 375 (1986)

[4] R. G. Nuzzo and D. L. Allara, Adsorption of Bifunctional Organic Disulfides on Gold Surfaces, *J. Am. Chem. Soc.* **105**, 4481 (1983)

[5] J. C. Love, L. A. Estroff, J. K. Kriebel, R. G. Nuzzo and G. M. Whitesides, Self-Assembled Monolayers of Thiolates on Metals as a Form of Nanotechnology, *Chem. Rev.* **105**, 1103 (2005)

[6] H. Park, A. K. L. Lim, A. P. Alivisatos, J. Park and P. L. McEuen, Fabrication of metallic electrodes with nanometer separation by electromigration, *Appl. Phys. Lett.* **75**, 301 (1999)

[7] D. R. Strachan, D. E. Smith, D. E. Johnston, T.-H. Park, M. J. Therien, D. A. Bonnell and A. T. Johnston, Controlled fabrication of nanogaps in ambient environment for molecular electronics, *Appl. Phys. Lett.* **86**, 043109 (2005)

[8] R. Saito, M. Fujita, G. Dresselhaus and M. S. Dresselhaus, Electronic structure of chiral graphene tubules, *Appl. Phys. Lett.* **60**, 2204 (1992)

[9] S. J. Tans, M. H. Devoret, H. Dai, A. Thess, R. E. Smalley, L. J. Geerligs and C. Dekker, Individual single-wall carbon nanotubes as quantum wires, *Nature* **386**, 474 (1997)

[10] S. Sapmaz, P. Jarillo-Herrero, J. Kong, C. Dekker, L. P. Kouwenhoven and H. S. J. van der Zant, Electronic excitation spectrum of metallic carbon nanotubes, *Phys. Rev. B* **71**, 152402 (2005)

[11] H. Grabert and M. H. Devoret (Eds.), *Single Charge Tunneling: Coulomb Blockade Phenomena in Nanostructures*, Vol. 294 of *NATO ASI Series, Series B: Physics*, Plenum Press, 1992

[12] X. Wang, Q. Li, J. Xie, Z. Jin, J. Wang, Y. Li, K. Jiang and S. Fan, Fabrication of Ultralong and Electrically Uniform Single-Walled Carbon Nanotubes on Clean Substrates, *Nano Lett.* **9**, 3137 (2009)

[13] R. Krupke, F. Hennrich, H. B. Weber, M. M. Kappes and H. v. Löhneysen, Simultaneous deposition of metallic bundles of single-walled carbon nanotubes using ac-dielectrophoresis, *Nano Lett.* **3**, 1019 (2003)

[14] C. W. Marquardt, *Elektrolumineszens organischer Moleküle nach Kontaktierung mit Kohlenstoff-Nanoröhren*, PhD Thesis, Universität Karlsruhe (2009)

[15] J.-P. Cleuziou, W. Wernsdorfer, V. Bouchiat, T. Ondarçuhu and M. Monthioux, Carbon nanotube superconducting quantum interference device, *Nature Nanotech.* **1**, 53 (2006)

[16] K. B. Blodgett, Monomolecular Films of Fatty Acids on Glass, *J. Am. Chem. Soc.* **56**, 495 (1934)

[17] K. B. Blodgett, Films Built by Depositing Successive Monomolecular Layers on a Solid Surface, *J. Am. Chem. Soc.* **5**, 1007 (1935)

[18] B. Mann and H. Kuhn, Tunneling Through Fatty Acid Salt Monolayers, *J. Appl. Phys.* **42**, 4398 (1971)

[19] H. Kuhn, Present Status and Future Prospects of Langmuir-Blodgett Film Research, *Thin Solid Films* **178**, 1 (1989)

[20] M. C. Petty, Possible applications for Langmuir-Blodgett films, *Thin Solid Films* **210/211**, 417 (1992)

[21] G. Binning, H. Rohrer, C. Gerber and E. Weibel, Tunneling through a controllable vacuum gap, *Appl. Phys. Lett.* **40**, 178 (1982)

[22] G. Binning, H. Rohrer, C. Gerber and E. Weibel, Surface Studies by Scanning Tunneling Microscopy, *Phys. Rev. Lett.* **49**, 57 (1982)

[23] X. D. Cui, X. Zarate, J. Tomfohr, O. F. Sankey, A. L. Moore, D. Gust, G. Harris and S. M. Lindsay, Reproducible Measurement of Single-Molecule Conductivity, *Science* **294**, 571 (2001)

[24] B. Xu and N. J. Tao, Measurement of Single-Molecule Resistance by Repeated Formation of Molecular Junctions, *Science* **301**, 1221 (2003)

[25] L. Venkataraman, J. E. Klare, C. Nuckolls, M. S. Hybertsen and M. L. Steigerwald, Dependence of single-molecule junction conductance on molecular conformation, *Nature* **442**, 904 (2006)

[26] L. Venkataraman, J. E. Klare, C. Nuckolls, M. S. Hybertsen and M. L. Steigerwald, Single-Molecule Circuits with Well-Defined Molecular Conductance, *Nano Lett.* **6**, 458 (2006)

[27] Y. S. Park, A. C. Whalley, M. Kamenetska, M. L. Steigerwald, M. S. Hybertsen, C. Nuckolls and L. Venkataraman, Contact Chemistry and Single-Molecule Conductance: A Comparison of Phosphines, Methyl Sulfides, and Amines, *J. Am. Chem. Soc.* **129**, 15768 (2007)

[28] Z.-L. Cheng, R. Skouta, H. Vazquez, J. R. Widawsky, S. Schneebeli, W. Chen, M. S. Hybertsen, R. Breslow and L. Venkataraman, *In Situ* formation of highly conducting covalent Au-C contacts for single-molecule junctions, *Nature Nanotech.* **6**, 353 (2011)

[29] C. J. Muller, J. M. van Ruitenbeek and L. J. de Jongh, Experimental observation of the transition from weak link to tunnel junction, *Phyisca C* **191**, 485 (1992)

[30] M. A. Reed, C. Zhou, C. J. Muller, T. P. Burgin and J. M. Tour, Conductance of a Molecular Junction, *Science* **278**, 252 (1997)

[31] C. A. Martin, D. Ding, H. S. J. van der Zant and J. M. van Ruitenbeek, Lithographic mechanical break junctions for single-molecule measurements in vacuum: possibilities and limitations, *New J. Phys.* **10**, 065008 (2008)

[32] P. S. Ho and T. Kwok, Electromigration in metals, *Rep. Prog. Phys.* **52**, 301 (1989)

[33] C. Durkan, *Current at the Nanoscale*, Imperial College Press, 2007

[34] H. Park, J. Park, A. K. L. Lim, E. H. Anderson, A. P. Alivisatos and P. L. McEuen, Nanomechanical oscillations in a single-C_{60} transistor, *Nature* **407**, 57 (2000)

[35] J. Park, A. N. Pasupathy, J. I. Goldsmith, C. Chang, Y. Yaish, J. R. Petta, M. Rinkoski, J. P. Sethna, H. D. Abruña, P. L. McEuen and D. C. Ralph, Coulomb blockade and the Kondo effect in single-atom transistors, *Nature* **417**, 722 (2002)

[36] W. Liang, M. P. Shores, M. Bockrath, J. R. Long and H. Park, Kondo resonance in a single-molecule transistor, *Nature* **417**, 725 (2002)

[37] A. A. Houck, J. Labaziewicz, E. K. Chan, J. A. Folk and I. L. Chuang, Kondo Effect in Electromigrated Gold Break Junctions, *Nano Lett.* **5**, 1685 (2005)

[38] H. B. Heersche, Z. de Groot, J. A. Folk, L. P. Kouwenhoven and H. S. J. van der Zant, Kondo Effect in the Presence of Magnetic Impurities, *Phys. Rev. Lett.* **96**, 017205 (2006)

[39] H. S. J. van der Zant, Y.-V. Kervennic, M. Poot, K. O'Neill, Z. de Groot, J. M. Thijssen, H. B. Heersche, N. Stuhr-Hansen, T. Bjørnholm, D. Vanmaekelbergh, C. A. van Walree and L. W. Jenneskens, Molecular three-terminal devices: fabrication and measurements, *Faraday Discuss.* **131**, 347 (2006)

[40] A. Mangin, A. Anthore, M. L. D. Rocca, E. Boulat and P. Lafarge, Transport through metallic nanogaps in an in-plane three-terminal geometry, *Appl. Phys. Lett.* **105**, 014313 (2009)

[41] J.-C. Charlier, X. Blase and S. Roche, Electronic and transport properties of nanotubes, *Rev. Mod. Phys.* **79**, 677 (2007)

[42] A. H. C. Neto, F. Guinea, N. M. R. Peres, K. S. Novoselov and A. K. Geim, The electronic properties of graphene, *Rev. Mod. Phys.* **81**, 109 (2009)

[43] J. W. Mintmire and C. T. White, Electronic and structural properties of carbon nanotubes, *Carbon* **33**, 893 (1995)

[44] R. Saito, G. Dresselhaus and M. S. Dresselhaus, *Physical Properties of Carbon Nanotubes*, Imperial College Press, 1998

[45] S. J. Tans, M. H. Devoret, R. J. A. Groeneveld and C. Dekker, Electron-electron correlations in carbon nanotubes, *Nature* **394**, 761 (1999)

[46] Y. Oreg, K. Byczuk and B. I. Halperin, Spin Configuration of a Carbon Nanotube in a Nonuniform External Potential, *Phys. Rev. Lett.* **85**, 365 (2000)

[47] D. V. Averin and K. K. Likharev, Single electronics: Correlated transfer of single electrons and Cooper pairs in small tunnel junctions, In: B. Altshuler, P. Lee and R. Webb (Eds.), *Mesoscopic Phenomena in Solids*, North-Holland, 1991

[48] G.-L. Ingold and Y. V. Nazarov, Charge Tunneling Rates in Ultrasmall Junctions, In: H. Grabert and M. H. Devoret (Eds.), *Single Charge Tunneling: Coulomb Blockade Phenomena in Nanostructures*, Plenum Press, 1992

[49] G. Schön, Single-Electron Tunneling, In: *Quantum Transport and Dissipation*, WILEY-VCH, 1998

[50] C. W. J. Beenakker, Theory of Coulomb-blockade oscillations in the conductance of a quantum dot, *Phys. Rev. B* **44**, 1646 (1991)

[51] J. C. Cuevas and E. Scheer, *Molecular Electronics - An Introduction to Theory and Experiment*, Vol. 1 of *World Scientific Series in Nanoscience and Nanotechnology*, World Scientific, 2010

[52] B. Limbach, *Untersuchung von Einzelelektronentransistoren auf der Basis von nanostrukturiertem Aluminium*, Diploma Thesis, Universität Karlsruhe (1998)

[53] R. Hoffmann, D. Weissenberger, J. Hawecker and D. Stöffler, Conductance of gold nanojunctions thinned by electromigration, *Appl. Phys. Lett.* **93**, 043118 (2008)

[54] D. Meschede, *Gerthsen Physik*, Springer-Verlag, 2004

[55] O. V. Boltalina, V. Y. Markov, A. Y. Borschevskii, N. A. Galeva and L. N. Sidorov, Saturated Vapor Pressure and Sublimation Enthalpy of Fluorine Derivatives of C_{60}, *J. Phys. Chem. B* **103**, 3828 (1999)

[56] S. Y. Quek, M. Kamenetska, M. L. Steigerwald, H. J. Choi, S. G. Louie, M. S. Hybertsen, J. B. Neaton and L. Venkataraman, Mechanically controlled binary conductance switching of a single-molecule junction, *Nature Nanotech.* **4**, 230 (2009)

[57] S. Grunder, R. Huber, V. Horhoiu, M. T. Gonzáles, C. Schönenberger, M. Calame and M. Mayor, New Cruciform Structures: Toward Coordination Induced Single Molecule Switches, *J. Org. Chem.* **72**, 8337 (2007)

[58] K.-H. Müller, Effect of the atomic configuration of gold electrodes on the electrical conduction of alkanedithiol molecules, *Phys. Rev. B* **73**, 045403 (2006)

[59] M. Kamenetska, S. Y. Quek, A. C. Whalley, M. L. Steigerwald, S. G. Louie, C. Nuckolls, M. S. Hybertsen, J. B. Neaton and L. Venkataraman, Conductance and Geometry of Pyridine-Linked Single-Molecule Junctions, *J. Am. Chem. Soc.* **132**, 6817 (2010)

[60] E. S. Tam, J. J. Parks, W. W. Shum, Y.-W. Zhong, M. B. Santiago-Berríos, X. Zheng, W. Yang, G. K.-L. Chan, H. D. Abruña and D. C. Ralph, Single-Molecule Conductance of Pyridine-Terminated Dithienylethene Switch Molecules, *ACS Nano* **5**, 5115 (2011)

[61] S. Grunder, D. M. Torres, C. W. Marquardt, A. Błaszczyk, R. Krupke and M. Mayor, Synthesis and Optical Properties of Molecular Rods Comprising a Central Core-Substituted Naphthalenediimide Chromophore for Carbon Nanotube Junctions, *Eur. J. Org. Chem.* **2011**, 478 (2011)

[62] K. Sonogashira, Y. Thoda and N. Hagihara, A Convenient Synthesis of Acetylenes: Catalytic Substitutions of Acetylenic Hydrogen with Bromoalkenes, Iodoarenes, and Bromopyridines, *Tetrahedron Lett.* **50**, 4467 (1975)

[63] N. M. Jenny, M. Mayor and T. R. Eaton, Phenyl-Acetylene Bond Assembly: A Powerful Tool for the Construction of Nanoscale Architectures, *Eur. J. Org. Chem.* **2011**, 4965 (2011)

[64] M. Mayor (2010), private communication

[65] A. V. Danilov, S. E. Kubatkin, S. G. Kafanov, K. Flensberg and T. Bjørnholm, Electron Transfer Dynamics of Bistable Single-Molecule Junctions, *Nano Lett.* **6**, 2184 (2006)

[66] T. Guo, P. Nikolaev, A. Thess, D. T. Colbert and R. E. Smalley, Catalytic Growth of single-walled nanotubes by laser vaporization, *Chem. Phys. Lett.* **243**, 49 (1995)

[67] S. Lebedkin, P. Schweiss, B. Renker, S. Malik, F. Hennrich, M. Neumaier, C. Stroemer and M. M. Kappes, Single-wall carbon nanotubes with diameters approaching 6 nm obtained by laser vaporization, *Carbon* **40**, 417 (2002)

[68] F. Hennrich, R. Wellmann, S. Malik, S. Lebedkin and M. M. Kappes, Reversible modification of the absorption properties of single-walled carbon nanotube thin films via nitric acid exposure, *Phys. Chem. Chem. Phys.* **5**, 178 (2003)

[69] M. J. O'Connell, S. M. Bachilo, C. B. Huffman, V. C. Moore, M. S. Strano, E. H. Haroz, K. L. Rialon, P. J. Boul, W. H. Noon, C. Kittrell, J. Ma, R. H. Hauge, R. B. Weisman and R. E. Smalley, Band Gap Fluorescence from Individual Single-Walled Carbon Nanotubes, *Science* **297**, 593 (2002)

[70] F. Hennrich, R. Krupke, K. Arnold, J. A. R. Stütz, S. Lebedkin, T. Koch, T. Schimmel and M. M. Kappes, The Mechanism of Cavitation-Induced Scission of Single-Walled Carbon Nanotubes, *J. Phys. Chem. B* **111**, 1932 (2007)

[71] M. S. Arnold, S. I. Stupp and M. C. Hersam, Enrichment of Single-Walled Carbon Nanotubes by Diameter in Density Gradients, *Nano Lett.* **5**, 713 (2005)

[72] M. S. Arnold, A. A. Green, J. F. Hulvat, S. I. Stupp and M. C. Hersam, Sorting carbon nanotubes by electronic structure using density differentiation, *Nature Nanotech.* **1**, 60 (2006)

[73] R. Krupke, F. Hennrich, H. B. Weber, D. Beckmann, O. Hampe, S. Malik, M. M. Kappes and H. v. Löhneysen, Contacting single bundles of carbon nanotubes with alternating electric field, *Appl. Phys. A* **76**, 397 (2003)

[74] C. W. Marquardt, S. Dehm, A. Vijayaraghavan, S. Blatt, F. Hennrich and R. Krupke, Reversible Metal-Insulator Transitions in Metallic Single-Walled Carbon Nanotubes, *Nano Lett.* **8**, 2767 (2008)

[75] W. Cui, *Charge Transport in Single Cooper-Pair Transistors*, PhD Thesis, Karlsruher Institut für Technologie (KIT) (2010)

[76] K. S. Ralls, D. C. Ralph and R. A. Buhrmann, Individual-defect electromigration in metal nanobridges, *Phys. Rev. B* **40**, 11561 (1989)

[77] D. Stöffler, *Herstellung dünner metallischer Brücken durch Elektromigration und Charakterisierung mit Rastersondentechniken*, PhD Thesis, Karlsruher Institut für Technologie (KIT) (2012)

[78] T. Taychatanapat, K. I. Bolotin, F. Kuemmeth and D. C. Ralph, Imaging Electromigration during the Formation of Break Junctions, *Nano Lett.* **7**, 652 (2007)

[79] H. B. Heersche, G. Lientschnig, K. O'Neill, H. S. J. van der Zant and H. Zandbergen, *In situ* imaging of electromigration-induced nanogap formation by transmission electron microscopy, *Appl. Phys. Lett.* **91**, 072107 (2007)

[80] D. R. Strachan, D. E. Johnston, B. S. Guiton, S. S. Datta, P. K. Davies, D. A. Bonnell and A. T. Johnston, Real-Time TEM Imaging of the Formation of Crystalline Nanoscale Gaps, *Phys. Rev. Lett.* **100**, 056805 (2008)

[81] J. F. Shackelford, W. Alexander and J. S. Park (Eds.), *CRC Materials Science and Engineering Handbook*, CRC Press, 1994

[82] A. Vilan, Analyzing Molecular Current-Voltage Characteristics with the Simmons Tunneling Model: Scaling and Linearization, *J. Phys. Chem. C* **111**, 4431 (2007)

[83] J. Reichert, R. Ochs, D. Beckmann, H. B. Weber, M. Mayor and H. v. Löhneysen, Driving current through Single Organic Molecules, *Phys. Rev. Lett.* **88**, 176804 (2002)

[84] J. G. Simmons, Low-Voltage Current-Voltage Relationship of Tunnel Junctions, *J. Appl. Phys.* **34**, 238 (1963)

[85] J. G. Simmons, Generalized Formula for the Electric Tunnel Effect between Similar Electrodes Separated by a Thin Insulating Film, *J. Appl. Phys.* **34**, 1793 (1963)

[86] J. G. Simmons, Electric Tunnel Effect between Dissimilar Electrodes Separated by a Thin Insulating Film, *J. Appl. Phys.* **34**, 2581 (1963)

[87] W. Wang, T. Lee and M. A. Reed, Mechanism of electron conduction in self-assembled alkenethiol monolayer devices, *Phys. Rev. B* **68**, 035416 (2003)

[88] J. M. Beebe, B. Kim, J. W. Gadzuk, C. D. Frisbie and J. G. Kushmerick, Transition from Direct Tunneling to Field Emission in Metal-Molecule-Metal Junctions, *Phys. Rev. Lett.* **97**, 026801 (2006)

[89] H. B. Akkerman, R. C. G. Naber, B. Jongbloed, P. A. van Hal, P. W. M. Blom, D. M. de Leeuw and B. de Boer, Electron tunneling through alkanedithiol self-assembled monolayers in large-area molecular junctions, *Proc. Natl. Acad. Sci. USA* **104**, 11161 (2007)

[90] L. Mandelstam and I. Tamm, The uncertainty relation between energy and time in nonrelativistic quantum mechanics, *J. Phys. (USSR)* **9**, 249 (1945)

[91] W. Heisenberg, Über den anschaulichen Inhalt der quantentheoretischen Kinematik und Mechanik, *Zeitschrift für Physik A: Hadrons and Nuclei* **43**, 172 (1927)

Acknowledgments

Thanks is owed to many people for their contribution to this thesis. First of all, I thank Prof. von Löhneysen for giving me the opportunity to start with it in the first place and for welcoming me in his group. Next, I want to thank Prof. Ustinov for his offer to co-referee this work. Furthermore, I am very grateful for the huge amount of input from my supervisor Dr. Roland Schäfer. I am deeply indebted to him for the time he invested in experimental and computational tasks.

Also, I want to thank (in order of appearance) Dr. Regina Hoffman from the Physics Institute and her former PhD student Dr. Dominik Stöffler for introducing us to the concept of feedback controlled electromigration, Dr. Beckmann for valuable input, Prof. Marcel Mayor and his postdoc Dr. Fabien Lemasson for the synthesis of molecules and Prof. Ralph Krupke, his former PhD student Dr. Christoph Marquardt and his current PhD student Cornelius Thiele for their experimental support and for providing material and instruments. Thanks also goes to Dr. Ninette Stürzl for her work on the formation of CNT rings with an AFM. Dr. Rudolf Schneider I want to thank for the permission to use the ion etching chamber of the thin-film group at the IFP.

Furthermore I am grateful for the support of the mechanics workshop of the IFP and the competent and quick help with administration of the IFP secretary Mrs. Edith Maass. I wish her a soon and full convalescence because the scientist at this institute would be lost without her.

Heartfelt thanks for the exchange of experience in the labs and at the (ir)regular weekly meetings goes to my (former) fellow PhD students Dr. Florian Hübler, Dr. Richard Montbrun, Dr. Andrea Assmann, Dr. Stephan Uebe, Dr. Markus Wissinger, Dr. Kerrin Doessel, Dr. Pablo Robert, Michael Wolf, Julia Setzler, Julia Neff and Oliver Berg, whom I also wish a successful and satisfactory completion of their thesis.

Last but not least I am most glad that I started this thesis because I met Cornelius Thiele. I thank him for his fearless treatment of samples regardless of time and hour, his moral support and for the laughs we shared. I hope there will be many more.